University of Stavanger

Faculty of Science and Technology

MASTER'S THESIS

Study program/ Specialization: Offshore Technology - Marine and Subsea Technology	Spring semester, 2017 Open
Writer: Laila Aarstad Igeh	…… (Writer's signature)
Faculty supervisor: Prof. Muk Chen Ong External supervisor(s): Dr. Jie Wu and Dr. Zhenhui Liu	
Thesis title: VIV Fatigue Investigation for Subsea Planar Rigid Spools and Jumpers	
Credits (ECTS): 30	
Key words: Subsea spools and jumpers, VIV, response model, force model, VIVANA, DNV-RP-F105, fatigue damage, torsional stress, flexural stress, principal stress	Pages: 108 + enclosure: 35 Stavanger, June 15, 2017

Abstract

Today, most new field developments consist of a subsea production system. Rigid spools and jumpers are important parts of these systems as they accommodate pipeline expansion and contraction due to changes in pressure and temperature, or due to movements of structural members. As rigid spools and jumpers are located near the sea bottom and normally consist of significant free spans, they could be subjected to seabed currents. These seabed currents, if large enough, can lead to vortex induced vibrations (VIV), which will lead to fast accumulation of fatigue damage. As failure of a rigid spool or jumper will have severe environmental and economic consequences, a proper fatigue assessment should be done to ensure sufficient fatigue life and avoid fatigue failure.

The complex geometry of rigid spools and jumpers means that the flow field and hence the vortex shedding will be complex. Currently, there are no proven design guideline or software available for assessing VIV response of a rigid spool/jumper. Moreover, the available design guidelines or software do not normally account for the torsional stiffness of the structure. Hence, they do not consider the fatigue damage due to torsional stresses. The objective of this study is to benchmark the prediction of the global response of a "M" shaped rigid jumper and investigate methods to account for torsional stress in fatigue analysis.

A validation study has been performed to evaluate the use of the semi-empirical program, i.e. VIVANA, and a response model approach based on DNV-RP-F105 (2006) to predict the VIV response of rigid spools and jumpers. These two VIV prediction approaches have been used to predict the VIV response of an “M” shaped rigid jumper exposed to varying current speeds hitting the jumper plane at two different angles. The two prediction methods have been evaluated against the existing experimental data.

When the current hits the jumper plane at a 10° angle, VIVANA seems to give fairly good predictions on the response frequency/mode and maximum displacement amplitude for most current speeds. The response model approach, on the other hand, seems to give large over-predictions of the displacement amplitude for most current speeds at this current direction. When the current has a 90° angle relative to the jumper plane, both VIVANA and the response model approach give good predictions with respect to the maximum jumper response.

The results from the validation study are further used to calculate the fatigue damage of the rigid jumper. A methodology presented in Nair et al. (2011) is used to calculate the torsional stresses. This methodology is based on using the stress assessment method and the fatigue assessment method given in DNV-RP-F105 (2006), which originally is for stresses due to bending (i.e. flexural stresses), to also calculate the stresses due to torsion. Then the fatigue damage is calculated using two different methods. In method 1, the fatigue damage due to flexural stress ranges and the fatigue damage due torsional stress ranges are calculated separately. In method 2, the first principal stress range is used to calculated the fatigue damage.

For all current speeds and both current directions, method 2 gives higher fatigue damage for current velocities where the torsional stress contribution is large. Method 2 is also somewhat less time-consuming than method 1.

Acknowledgement

I would like to thank my supervisors, Prof. Muk Chen Ong, Dr. Jie Wu, and Dr. Zhenhui Liu, for their continuous guidance and support throughout this semester. I really appreciate the time you have spent on helping me with this thesis.

I would also like to thank my family and friends for their love and moral support throughout the years of my studies.

List of Abbreviations

VIV – vortex induced vibration

IL - in-line

CF – cross-flow

CFD – computational fluid dynamics

2D – two dimensional

3D – three dimensional

FEA – finite element analysis

FEM – finite element model

Table of Content

Abstract ii

Acknowledgement iv

List of Abbreviations v

Chapter 1: Introduction 1

1.1. Background 1

1.2. Objectives 2

1.3. Outline of the Thesis 2

Chapter 2: Background and Literature Review 4

2.1. Spool and Jumper 4

2.2. VIV Basics 7

2.2.1. Important parameters 7

2.2.2. Vortex formation 13

2.2.3. Vortex induced forces 15

2.2.4. VIV phenomenon 16

2.3. VIV Analysis Methods 17

2.3.1. Experimental methods 17

2.3.2. Numerical methods 23

2.4. VIV Mitigation 26

2.4.1. Avoid resonance 26

2.4.2. Increase the stability parameter K_s 26

2.4.3. Add vortex suppression devices 27

2.5. Fatigue Damage Assessment 27

2.5.1. The stress based approach 28

2.5.2. Fatigue damage 29

2.6. Literature Review 30

Chapter 3: VIV Response Estimation Methodology 33
3.1 The Response Model Approach 33
3.1.1 The DNV-RP-F105 response models 34
3.2 The Force Model Approach - VIVANA 43
3.2.1 VIVANA analysis procedure 44
Chapter 4: Evaluation of Assessment Methods for Estimating the VIV Response of Planar Rigid Jumpers (To be submitted to *Marine Structures*) 46
Chapter 5: Fatigue Damage Assessment 81
5.1. Fatigue Damage Calculation Methodology 81
5.1.1. Method 1: a method presented by Nair et al. (2011) 81
5.1.2. Method 2: a novel method using first principal stress 82
5.2. Modal Analysis 83
5.2.1. Modal unit amplitude stresses 87
5.2.2. Modal stresses for the 10° flow direction 88
5.2.3. Modal stresses for the 90° flow direction 90
5.3. Results and Discussion 92
5.3.1. Fatigue damage results of method 1 92
5.3.2. Fatigue damage results of method 2 96
5.3.3. Comparison of the fatigue damage calculated using method 1 and method 2 ... 98
5.4. Conclusions 102
Chapter 6: Conclusions 103
6.1. Summary of the Results in Chapter 4 103
6.2. Summary of the Results in Chapter 5 104
6.3. Conclusions 104
Chapter 7: Future work 105
References 106

Appendix A: VIVANA Output 109

A.1. 10° Flow Direction 109

A.2 90° Flow Direction 113

Appendix B: Response Model Calculations and Results 117

B.1 10° Flow Direction 117

B.2. 90° Flow Direction 125

Appendix C: Stress Assessment 131

C.1 Flexural and Torsional Stresses Calculated Using the VIV Response Predicted by the Response Model Approach. 131

C.1.1. 10° flow direction 131

C.1.2. 90° flow direction 134

C.2. Flexural and Torsional Stresses Calculated Using the VIV Response Predicted by VIVANA 137

C.2.1. 10° flow direction 138

C.2.2. 90° flow direction 141

Chapter 1: Introduction

1.1. Background

Today, most new field developments consist of a subsea production system. Rigid spools and jumpers are important parts of these systems as they accommodate pipeline expansion and contraction due to changes in pressure and temperature, or due to movements of structural members.

Since rigid spools and jumpers are located near the sea bottom, they could be subjected to seabed currents. These seabed currents, if large enough, can lead to vortex induced vibrations (VIV) which can significantly decrease the spools/jumpers fatigue life. As failure of a rigid spool or jumper will have severe environmental and economic consequences, a proper fatigue assessment should be done to ensure sufficient fatigue life and avoid fatigue failure.

Semi-empirical programs, such as VIVANA (Sintef Ocean, 2016) and SHEAR7 (MIT, 2016), are widely used by the industry for VIV prediction. A response model approach has also been developed to evaluate the VIV responses of free spanning pipelines as described in DNV-RP-F105 (2006).

However, the problem is that compared to other slender marine structures, the flow speed normal to the structural members of subsea rigid spools and jumpers can be three-dimensional even in a uniform flow due to their geometry in planar or multi-planar space. Therefore, the VIV response is complex and current heading dependent. Applying different VIV prediction methods may lead to large differences. There is limited validation of the VIV prediction methods against model tests.

Another problem is that the torsional stiffness of the structure normally is not accounted for by the present VIV prediction tools. Thus, the method to calculate fatigue damage due to combined bending and torsional stress needs further studies.

In Nair et al. (2011) a detailed methodology that can be followed to calculate the torsional stresses due to VIV, and hence the torsional fatigue damage, is presented. This method is based on using the stress assessment method and the fatigue assessment method given in DNV-RP-

F105, which originally is for stresses due to bending (i.e. flexural stresses), to also calculate the stresses due to torsion. In this method, the flexural and torsional stresses are considered separately. Thus, the fatigue damage due to torsion and the fatigue damage due to bending is also considered separately.

Another method, based on DNV-RP-C203 (2010), is proposed in this thesis where the fatigue damage due to bending and torsion is combined. In this method, the first principal stress is used to combine the shear stresses due to torsion and the bending stresses. Then this stress is used to calculate the fatigue damage.

1.2. Objectives

The objectives of the thesis are:

- To evaluate the use of different VIV prediction methods for planar rigid spools and jumpers, i.e. the force model based approach, VIVANA, and the response model approach based on DNV-RP-F105.

- To investigate the influence of the torsional stress on the fatigue assessment for rigid jumpers. Moreover, evaluate a novel method to calculate the fatigue damage using the first principal stress.

1.3. Outline of the Thesis

The thesis consists of the following chapters:

Chapter 1 presents the background, objective and outline of the thesis.

Chapter 2 gives a brief description of rigid jumpers and spools, VIV basics, fatigue damage assessment, and previous studies on VIV of free spanning pipelines and rigid jumpers and spools.

Chapter 3 gives a detailed description of the two VIV prediction approaches to be evaluated in this thesis, VIVANA and the response model approach based on DNV-RP-F105.

Chapter 4 evaluates the use of the semi-empirical program, i.e. VIVANA, and a response model approach based on DNV-RP-F105(2006) to predict the VIV response of rigid jumpers. These two methods have been used to predict the VIV response of an "M" shaped rigid jumper exposed to varying current speeds hitting the jumper plane at two different angles. The two prediction methods are evaluated against the existing experimental data. The figures in this chapter are based on tables and information given in Appendix A and B. This chapter is presented in an article format, which will be submitted to the scientific journal *Marine Structures*.

Chapter 5 presents the results from the fatigue assessment.

Chapter 6 summarizes the key results and present the main conclusions from Chapter 4 and 5.

Chapter 7 presents the recommendations for future work.

Chapter 2: Background and Literature Review

2.1. Spool and Jumper

The differences between rigid spools and jumpers are not very clear as different definitions have been given throughout the years in literature.

According to Corbetta and Cox (2001) the difference between subsea rigid spools and jumpers lies in the way they are connected to the subsea structure. Rigid spools are horizontal and horizontally connected to the subsea structure via horizontal tie-in, whereas the rigid jumpers are vertical and vertically connected to the subsea structure via vertical tie-in. However, in other sources different explanations are used to define a rigid jumper and a rigid spool.

In Lafitte et al. (2007) the term rigid jumper is used for pipe sections connecting wells and manifolds whereas the term rigid spool is used for pipe sections connecting manifolds and flowlines. This is illustrated in Figure 2.1. The same terminology is also used in Nelson (2010). This terminology is not in contradiction to the explanation given by Corbetta and Cox (2001).

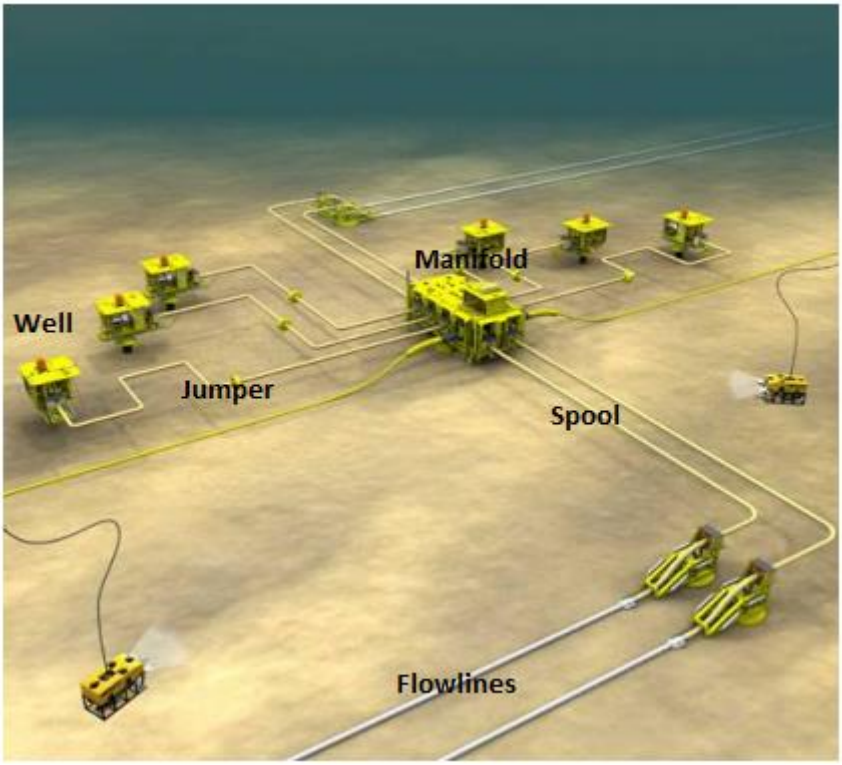

Figure 2.1. Dalia production well cluster (taken from Lafitte et al., 2007).

The *Subsea Engineering Handbook* (Bai and Bai, 2012) says that that a rigid jumper can be connected using both a horizontal and vertical tie-in, and can be both horizontal and vertical. This is in contradiction to the explanation given by Corbetta and Cox (2001). The differences in these explanations are probably due to the technological advances that have been made in the years after the article by Corbetta and Cox (2001) was published. Today, also rigid spools can be used for both horizontal and vertical tie-in.

It is clear from the explanations above, that rigid jumpers and spools have overlapping functions. Both types can be used for both tie-in methods, and both types can be horizontal. However, according to the explanations above it seems like only rigid jumpers can be vertical.

Based on the aforementioned explanations, the following definitions have been made:

- Rigid spools are used to connect a pipeline and a riser, a pipeline and a subsea structure, or two subsea structures. Rigid spools are horizontal and can be used in both horizontal and vertical tie-in. Figure 2.2 show a “Z” shaped rigid spool.

- Rigid jumpers are commonly used to connect two subsea structures, but can also be used to connect a pipeline and a subsea structure. Rigid jumpers can be vertical or horizontal, and can be used in both horizontal and vertical tie-in. Figure 2.3 show an “M” shaped rigid jumper.

Figure 2.2. Rigid spool (Spool, 2008).

Figure 2.3. Rigid jumper (Jumper, 2014).

Even though there are some differences in the definitions of rigid spools and jumpers, they both serve as interfaces between structural components subsea (including pipelines and risers) and have the same purpose. Their purpose is to deal with the inaccuracies in the installation of offshore pipelines, the expansion and contraction of pipelines due to differences in pressures and temperatures, and the translation of pipelines and/or risers due to dynamic loading.

Rigid jumpers and spools consists of short pipe segments put together in a 2D-space (planar) or 3D-space (multi-planar) structure. They must be flexible enough to tolerate the end displacements due to translation of pipelines and/or risers, and the temperature expansion/contraction of pipelines. Flexibility can be achieved by allowing them to deflect by using bends or elbows. However, they should be rigid enough to withstand the environmental loading acting on them.

Multi-planar rigid jumpers are increasingly being used subsea because of their increased flexibility compared to planar rigid jumpers and spools. This increase in flexibility is because they allow for deflection in more directions due to their multi-planar shape. However, these multi-planar rigid jumpers can be more susceptible to fatigue damage as they can experience larger bending and torsional loads.

The present thesis is focused on planar rigid jumpers only.

2.2. VIV Basics

It is important that designers of offshore structures account for VIV, especially when it comes to fatigue. This is because VIV gives dynamic stresses which leads to lower fatigue life. In other words, faster fatigue damage accumulation.

2.2.1. Important parameters

Important parameters used in the study of VIV are described in the following:

Reynolds number (Re)

The flow regime depends mainly on Reynolds number which is the ratio of the inertia forces to the viscous forces in the fluid. Reynolds number is a dimensionless quantity expressed as:

$$Re = \frac{inertia\ forces}{viscous\ forces} = \frac{UD}{\nu} \tag{2.1}$$

where

- U is the undisturbed flow velocity,
- D is cylinder diameter,
- ν is the kinematic viscosity of the fluid.

If the inertia forces are large relative to the viscous forces, which is the case at large Reynolds numbers, the viscous forces are not large enough to prevent the random and fast fluctuations of the fluid. Thus, the flow is turbulent. At moderate or small Reynolds numbers, the viscous forces are large enough to prevent this. Thus, the flow is laminar. The critical Reynolds number is the number at which the flow goes from laminar to turbulent. This number is influenced by the geometry of the structure and the flow conditions (Hjertager, 2013).

Because the flow regime is dependent on the Reynolds number, the Reynolds number will define the vortex shedding patterns. Figure 2.4 show the vortex shedding patterns behind a cylinder for various Reynolds numbers.

$300 < Re < 3 \times 10^5$ is referred to as the subcritical regime, $3 \times 10^5 < Re < 3.5 \times 10^6$ is referred to as the critical regime, and $3.5 \times 10^6 < Re$ is referred to as the supercritical regime. Most VIV experiments take place in the subcritical regime because the vortex shedding process is essentially remained the same throughout this regime. Even though full-scale cases easily will enter the critical and subcritical regimes, using experimental data from the subcritical regime is commonly understood to be conservative when applied to these full-scale cases (Larsen, 2011).

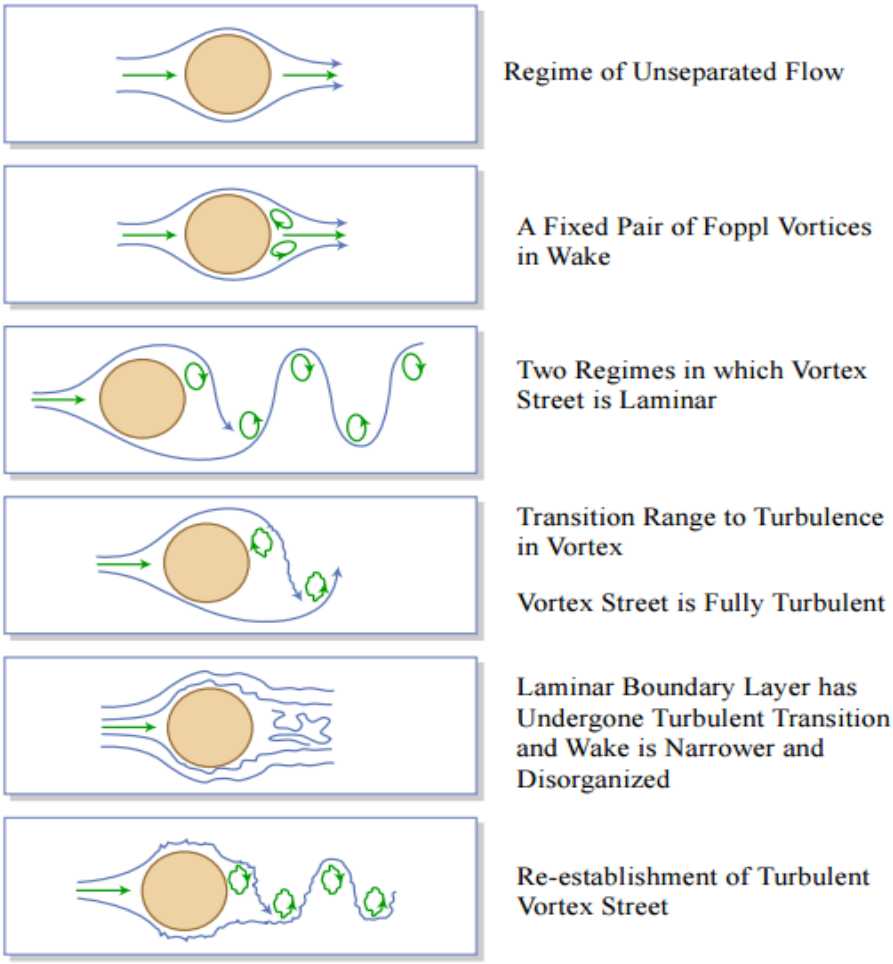

Figure 2.4. Vortex shedding pattern behind a cylinder for various Reynolds numbers (taken from Techet, 2005).

Strouhal number (St)

The Strouhal number is a dimensionless parameter that gives a relation between the vortex shedding frequency, the flow velocity, and the diameter of the cylinder. It is expressed as:

$$St = \frac{f_v D}{U} \tag{2.2}$$

where f_v is the vortex shedding frequency.

The Strouhal number is stable at a value close to 0.2 in the subcritical regime, this is, as mentioned previously, because the vortex shedding process, and hence the vortex shedding frequency, essentially remains the same throughout this regime. In the critical flow regime, Strouhal number strongly depends on the surface roughness of the structure. If the structure has a smooth surface the Strouhal number will have a large increase in this flow region. If the structure has a rough surface the Strouhal number will not experience such a large increase in this region. When the flow is in the super critical regime the Strouhal number will again be stable at a value close to 0.24 (Larsen, 2011). This is illustrated in Figure 2.5.

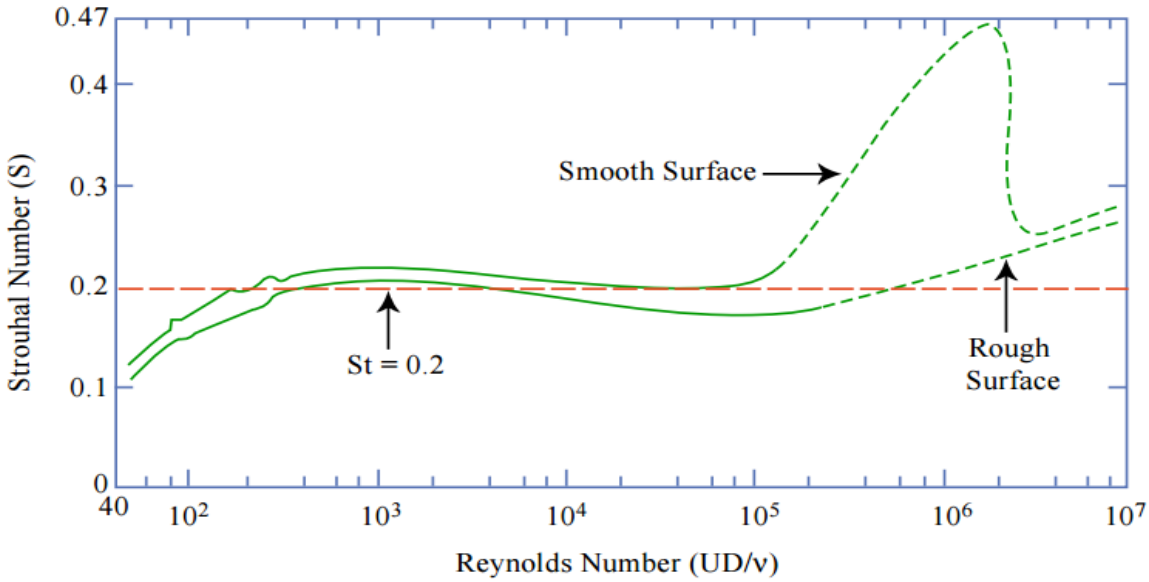

Figure 2.5. Strouhal number vs. Reynolds number for circular cylinders (taken from Techet, 2005).

Normally offshore slender structures have sufficient roughness to avoid the large increase of Strouhal number in the critical flow regime. Hence, the Strouhal number is often considered to be constant in VIV analyses of such structures.

Reduced velocity (V_r)

Reduced velocity is a function of velocity, diameter, mass (m), added mass in still water (m_{a0}), and stiffness of the structure (k). It is a dimensionless quantity expressed as:

$$V_R = \frac{U}{Df_n} \tag{2.3}$$

where $f_n = \frac{1}{2\pi}\sqrt{\frac{k}{m+m_{a0}}}$ is the eigenfrequency of the structure in still water.

Non-dimensional frequency ($\hat{f}$)

The non-dimensional frequency is defined as:

$$\hat{f} = \frac{Df_{osc}}{U} \tag{2.4}$$

where f_{osc} is the oscillation/response frequency.

Stability parameter (K_s)

The stability parameter determines the maximum possible vibration amplitude as it represents the damping for a given modal shape. It is defined as:

$$K_s = \frac{4\pi m_e \zeta_T}{\rho D^2} \tag{2.5}$$

where

- m_e is the effective mass,
- ρ is the density of the fluid surrounding the structure,
- ζ_T is the total modal damping ratio comprising of structural damping (ζ_{str}), soil damping (ζ_{soil}), and hydrodynamic damping (ζ_h) (DNV, 2006).

Keulegan Carpenter number

For cylinders exposed to oscillatory flow (wave flow) the Keulegan Carpenter (*KC*) number, in addition to Reynolds number, is needed to define the flow around the cylinder. *KC* is defined as:

$$KC = \frac{U_W}{f_W D} \tag{2.6}$$

where

- U_W is the amplitude of the significant wave-induced velocity normal to the pipe,
- f_W is the significant wave frequency (DNV, 2006).

Small *KC* means that the water particles orbital motion is small compared to the cylinder width. Hence, vortex shedding cannot occur. When *KC* is large, the water particles travel a large distance compared to the cylinder width, and vortex shedding can occur. This is illustrated in Figure 2.6.

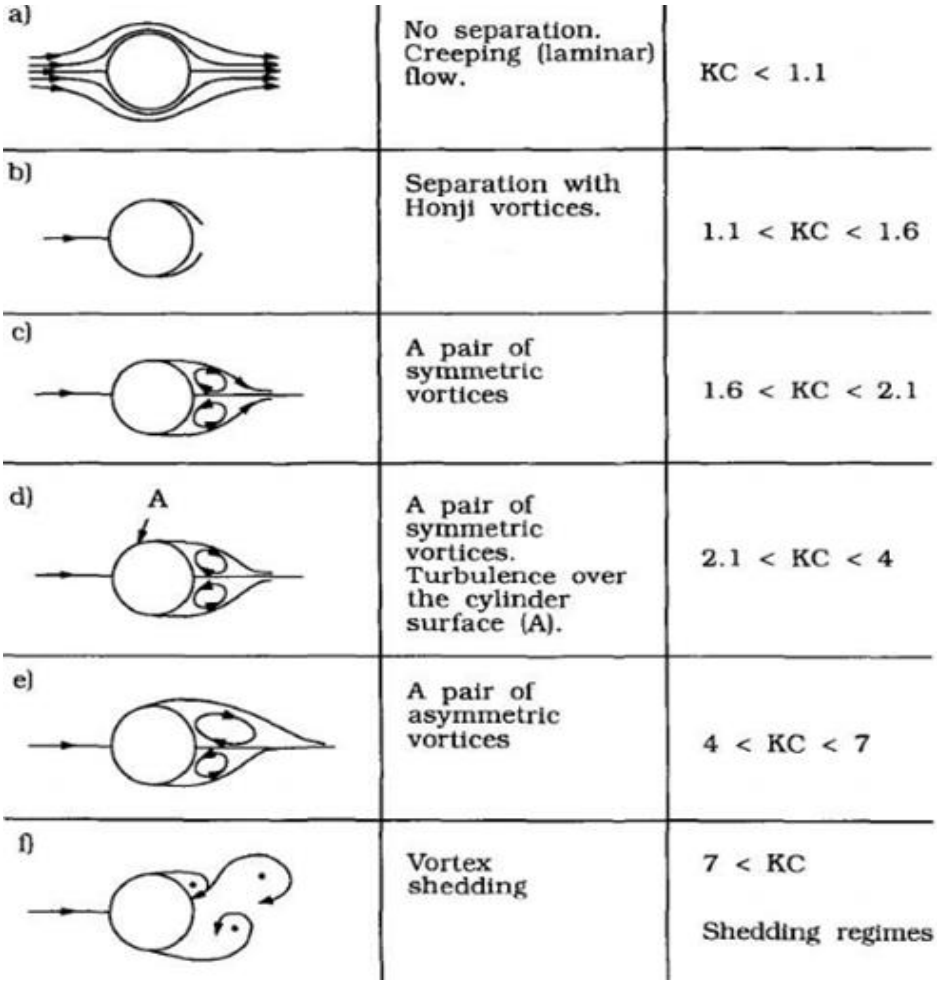

Figure 2.6. Flow regime around a smooth cylinder in oscillatory flow, Re=103 (taken from Sumer and Fredsøe, 1997).

2.2.2. Vortex formation

When a slender structure is exposed to current vortices can arise on the downstream side of it, if the current is large enough. This vortex formation is due to the friction between the structure and the fluid.

When the fluid comes in contact with the surface of the structure it is slowed down due to the friction forces between them. Close to the surface of the structure, the friction force between the surface and the fluid are so large that the fluid velocity is zero. As the distance between the fluid and the surface increases, the friction forces decrease. Thus, the flow velocity increases as the distance from the surface increases. This region of flow, where the surface of the structure

influences the fluid velocity, is called the boundary layer region. Figure 2.7 show the boundary layer region for a flat and a curved surface, respectively.

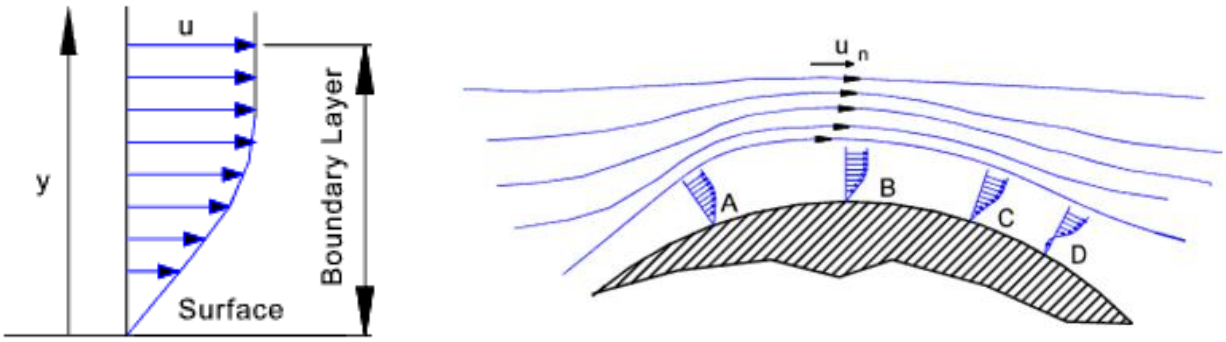

Figure 2.7. Boundary layer region for a flat surface and a curved surface (Drag on objects moving through fluids, 2013).

Figure 2.7 shows that the flow velocity will increase with the distance from the surface, until a point where the flow velocity reaches a constant maximum value. At this point the distance from the surface to the fluid is so large that the frictional forces become zero. This point is the end of the boundary layer region, and the irrotational flow region begins. In this region, the frictional effects are negligible (Hjertager, 2013). It is the difference in velocity between boundary layer region and irrotational flow region that will cause the formation of vortices.

For Re >40 the vortices formed are unstable when expose to small disturbances. A consequence of this is that one of the vortices will grow larger and larger until it become so large that it has the sufficient strength to make the opposite vortex shed from the structure (Sumer and Fredsøe, 1997). Thus, the vortices are shed alternately from the upper and bottom surface of the structure. This is shown in Figure 2.8.

As the fluid particles in the vortices formed downstream of the structure have higher velocities than the fluid particles upstream, there will be a difference in pressure between the upstream and downstream side. This pressure difference leads to fluctuating forces in x and y direction (Gudmestad, 2015).

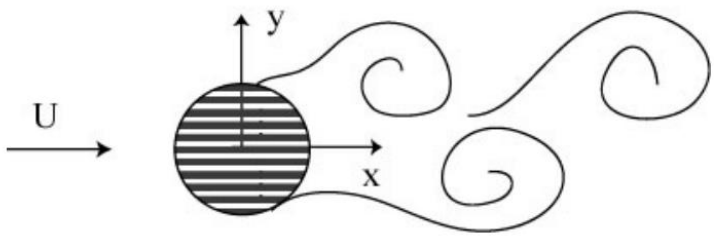

Figure 2.8. Alternate vortex shedding (taken from Techet, 2005).

2.2.3. Vortex induced forces

The difference in pressure between the upstream and downstream side of a slender structure, as mentioned in section 2.2.2, causes in-line (IL) and cross-flow (CF) fluctuating forces which can lead to vibration of the structure. The fluctuating forces in the direction IL with the current, drag forces, will cause IL vibrations whereas the fluctuating forces in the CF direction, lift forces, will cause CF vibrations. The lift and drag forces are expressed by using hydrodynamic force coefficients. These coefficients are defined as:

$$C_D = \frac{F_D(t)}{0.5\rho U^2 D} \tag{2.7}$$

$$C_L = \frac{F_L(t)}{0.5\rho U^2 D} \tag{2.8}$$

where

- C_D is the drag coefficient and C_L is the lift coefficient,
- $F_D(t)$ is the drag force as a function of time,
- $F_L(t)$ is the lift force as a function of time,
- U is the undisturbed flow velocity,
- D is cylinder diameter,
- ρ is the density of the fluid.

Added mass is the hydrodynamic force component that is in phase with the CF or IL acceleration of the structure (thus negative added mass is possible). The added mass influences the structures eigenfrequency, and the degree of influence depends on the dry mass of the

structure. In other words, a light structure is more subjectable to an adjustment in eigenfrequency due to the added mass than a heavy structure with the same dimensions. Because of this, a light structure will vibrate in a larger reduced velocity range than a heavy structure (Larsen, 2011). The added mass is expressed by using an added mass coefficient, C_a, in IL and CF direction.

The force and added mass coefficients can be found from forced oscillation tests which are described in section 2.3.1.

2.2.4. VIV phenomenon

Vortex induced vibration (VIV) is vibration at resonance, meaning that it occurs when the vortex shedding frequency (f_v) is close to, or equal to, an eigenfrequency (f_n) of the structure. For slender structures the VIV response will have a frequency (f_{osc}) close to an eigenfrequency of the structure. When $f_v = f_n = f_{osc}$ we have "lock-in", which means that f_v will remain locked to f_{osc} within a certain range of reduced velocity. In other words, f_v will not change but remain locked to f_{osc} even though the flow velocity, and hence the response amplitude, is increased. Within the "lock-in" range the structure experiences large amplitude oscillations.

"Lock-in" of a structure in water is somewhat different than "lock-in" of a structure in air. This is because f_n will be influenced by the change in hydrodynamic added mass, and f_v will be influenced by the oscillation of the structure. Thus, f_{osc} become a compromise between f_n and f_v.

VIV is said to be a self-limiting process. This is because the forces driving the vibrations varies when the "effective" diameter varies. When the response amplitude is small, the vortex shedding process will transfer energy from the fluid to the structure, hence increasing the response amplitude. Eventually the structures response amplitude will be large enough to create an energy balance between energy in and out of the vortex shedding process. The structure is now in the "lock-in" region. The structure will remain in the "lock-in" region until the flow velocity is large enough to give a response amplitude that exceeds a certain level. The process will now transfer energy from the structure to the fluid and hence lead to damping. The structure is no longer in the "lock-in" region.

There are two types of VIV, CF VIV and IL VIV. CF VIV is caused by the fluctuating lift forces, whereas fluctuating drag forces cause IL VIV. Due to the alternating vortex shedding, the fluctuations in lift force occur at the vortex shedding frequency and the fluctuations in drag force occur at twice the vortex shedding frequency. In other words, the frequency of the fluctuating drag force is twice the frequency of the fluctuating lift force (Techet, 2005).

$$f_{drag} = 2 \times f_{lift} \tag{2.9}$$

CF VIV gives larger response amplitudes than IL VIV, and will therefore influence the static deformation of the structure more and give larger dynamic stresses. However, IL VIV can in some cases be just as, or even more critical than CF VIV when it comes to fatigue damage. This can be the case for slender structures, like free spanning pipelines or jumpers/spools, subjected to seabed currents. The reason for this is that IL VIV can be initiated at lower current velocities than CF VIV, and therefore can occur more often. In addition, the frequency of the fluctuating drag force is twice the frequency of the fluctuating lift force. Meaning that the number of stress cycles due to IL VIV will be twice the amount of the stress cycles due to CF VIV (Aronsen, 2007).

2.3. VIV Analysis Methods

In the following two sections, experimental methods, used to understand the VIV phenomenon, and numerical methods, used to predict VIV, are briefly discussed. The numerical methods are often based on result from experimental methods.

2.3.1. Experimental methods

Experimental methods have for many years been used to illustrate and understand the VIV phenomenon. The experimental methods most commonly used are:

Fixed cylinder tests

These tests are basically a fixed cylinder, with a constant diameter *(D)*, subjected to a constant flow velocity (*U*). Since *U*, *D*, and the kinematic viscosity (ν) is known, hence *Re* is known, the information given in Figures 2.4, 2.5 and 2.6 can be obtained by such tests.

Free oscillation tests of rigid cylinders

In a free oscillation test of a rigid cylinder, an elastically supported rigid cylinder is subjected to constant current. Tests like this, can be performed as IL, CF, or combined IL and CF tests. The simplest type of a free oscillation test is a cylinder supported by a spring in IL, CF or combined IL and CF direction, as shown in Figure 2.9.

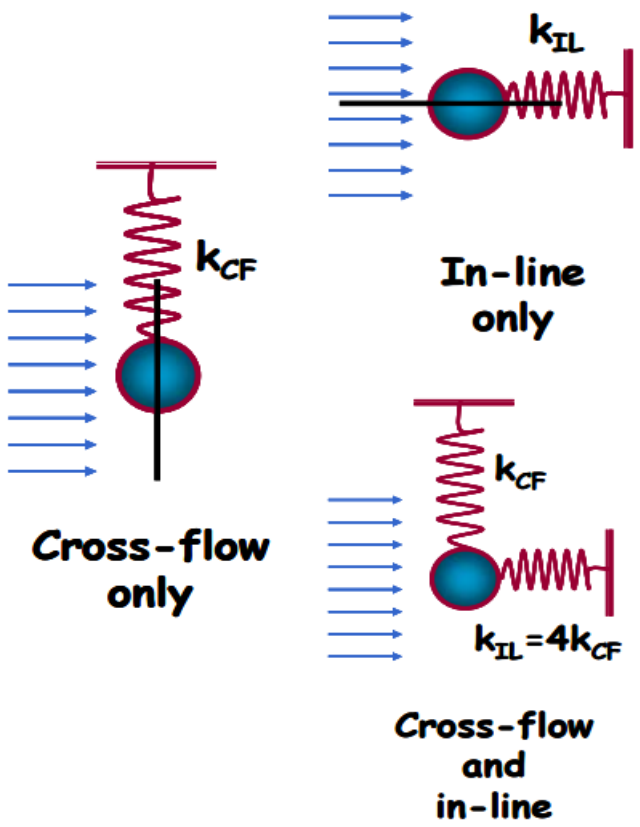

Figure 2.9 Boundary conditions for a vibrating cylinder (taken from Larsen, 2011).

These 2D tests have three key parameters: Strouhal number (St), reduced velocity (V_R), and the non-dimensional frequency ($\hat{f}$).

$$V_R = \frac{U}{D f_n} \qquad St = \frac{f_v D}{U} \qquad \hat{f} = \frac{f_{osc} D}{U}$$

As can be observed, each of these parameters are linked to a frequency. These frequencies are defined as follows for these types of tests:

$$f_n = \frac{1}{2\pi}\sqrt{\frac{k}{m + m_{a0}}} \tag{2.10}$$

$$f_v = \frac{St\ U}{D} \tag{2.11}$$

$$f_{osc} = \frac{1}{2\pi}\sqrt{\frac{k}{m + m_a}} \tag{2.12}$$

where k is the stiffness of the spring, m is the cylinder mass, m_{a0} is the hydrodynamic added mass in still water, and m_a is the hydrodynamic added mass for the actual oscillation and flow condition (Larsen, 2011).

From the free oscillation tests, parameters like CF amplitudes and frequencies, IL amplitudes and frequencies, and drag force coefficients for oscillating cylinders can be obtained. If the forces on the cylinder are measured, the added mass can be found as a function of V_R. It is from tests of this kind that the difference in the reduced velocity range for a light and heavy cylinder, as explained in section 2.2.3, have been observed.

Forced oscillation tests of rigid cylinders

In a forced oscillation test, a rigid cylinder in uniform flow is given a predefined motion. This motion is normally a harmonic motion in CF, IL, or a combination of CF and IL direction. A typical forced oscillation test set up is shown in Figure 2.10.

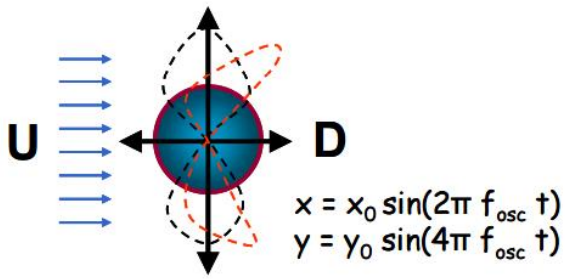

Figure 2.10. Forced oscillation test setup (taken from Larsen, 2011).

In these tests, the hydrodynamic forces are measured and the force components in phase with the forced motion acceleration, i.e. added mass, and the force components in phase with the velocities in IL and CF directions, i.e. lift and drag forces, can be identified. When added mass, lift forces, and drag forces are known, the added mass and hydrodynamic force coefficients can be found. Thus, from tests of this kind the added mass and hydrodynamic force coefficients (IL and CF) can be found for any combination of frequency and amplitude.

Forced oscillation tests do not have any eigenfrequency (as the oscillation is forced), and the cylinder mass is not relevant. Because of this, the results from such tests are normally presented in terms of the non-dimensional frequency.

In Gopalkrishnan (1993), the lift and drag forces on circular cylinders for CF oscillations where measured, for several different combinations of frequency and amplitude, by using forced oscillation tests. From the results from these tests added mass, drag force, and lift force coefficients were found. Similar tests for IL oscillations where done by Aronsen (2007). Today, this type of data can be found in the open literature and have been used in force based VIV prediction approaches such as VIVANA.

Experiments with flexible beams

Flexible beam experiments could be small-scale laboratory experiments or large-scale experiments done in lakes, harbours, or at sea. In these experiments, a pipeline or riser model, that might have varying cross section, is subjected to sheared current. For these cases, of long and slender structures, many eigenfrequencies are active (can be excited) and hence the VIV response of such structures is complicated. Currently, there does not exist any model that can reproduce the exact response observed in these experiments. However, there exist an approach that is commonly accepted.

In the commonly accepted approach, the key is to define the excitation zone for a specific frequency, and then calculate the response which that frequency gives independent of other frequencies that are active. There are two ways of doing this, time sharing (consecutive method) and space sharing (concurrent method). Time sharing is when only one of the competing frequencies will dominate for a period of time. This is illustrated in Figure 2.11. Space sharing is when all competing frequencies are active at the same time, but the shedding process at a specific point along the beam can only excite one of the active frequencies (Larsen, 2011). This is illustrated in Figure 2.12.

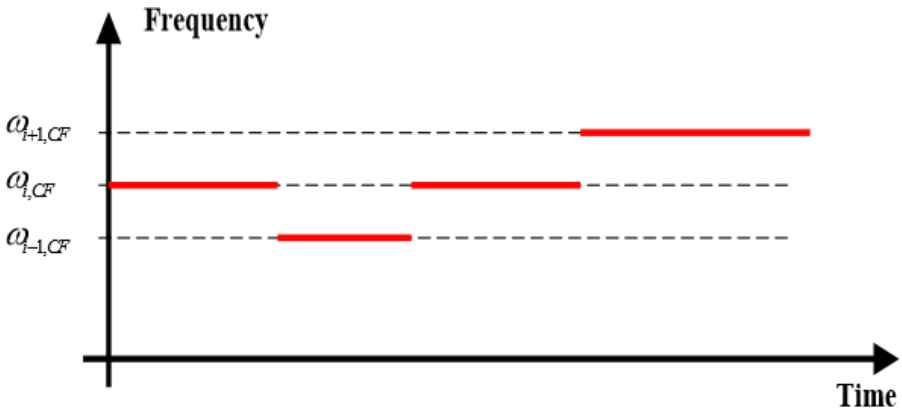

Figure 2.11. Illustration of time shearing (taken from Larsen, 2011).

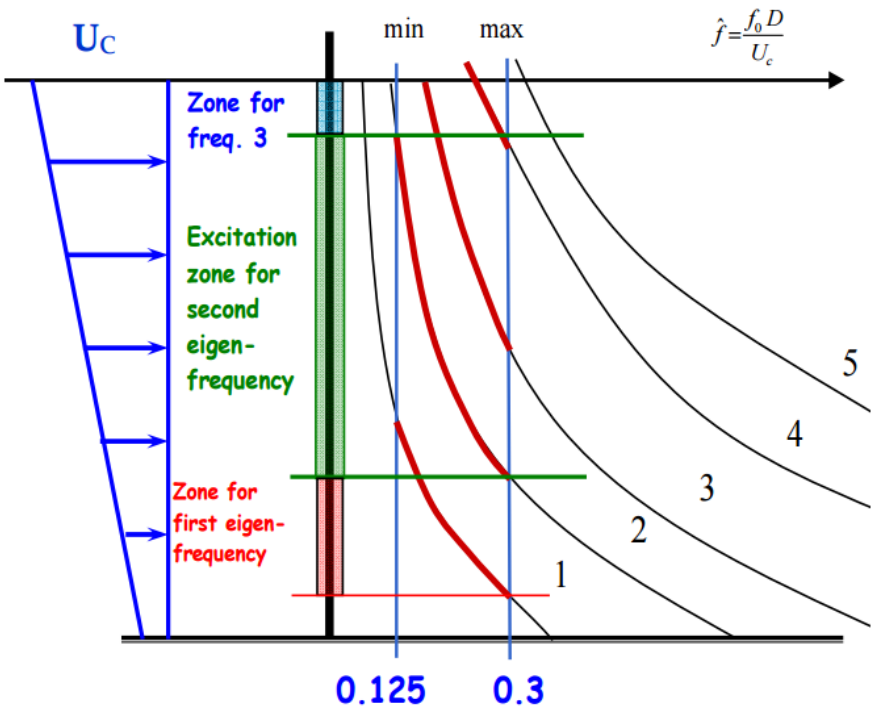

Figure 2.12. Illustration of space shearing (taken from Passano et al., 2016).

Some important observations, from laboratory experiments with flexible beams and observations of real structures, are listed in the following:

- the response takes place at discrete frequencies,
- even if several eigenfrequencies could become excited, only one will normally dominate.
- A single frequency response is in general not a single mode response,
- VIV is not always a stable response.

Observations of real structures

Very little data from real structures can be found in the open literature as companies do not want to share this information with competitors.

Model tests

Model tests are a good way of investigating the VIV phenomenon and improving the understanding of VIV for different types of structures. For example, the Ormen Lange model test program which main goal was to investigate the occurrence of interaction between the VIV response of several modes. Or the ExxonMobil rigid jumper model test, which goal was to provide benchmark data for validation of VIV prediction approaches for rigid jumpers.

2.3.2. Numerical methods

Numerical methods are used to predict slender structures response to VIV. The numerical methods can be classified into the following models:

Response based models

Response based model uses hydrodynamic parameters such as reduced velocity, damping ratio, stability parameter, etc. to directly determine the maximum VIV displacement amplitude. These parameters are based on experimental results.

The response based models uses results from several free oscillation experiments to plot *A/D* as a function of V_R. For IL VIV evaluation, response curves for levels of the stability parameter K_s, also based on experimental results, are made inside the IL plot (Aronsen, 2007). This plot can then be used to find the IL response amplitude. An example of a plot of this type is illustrated in Figure 2.13.

For CF VIV evaluation, response curves for levels of the Keulegan-Carpenter number, *KC*, are made inside the CF plot. This plot can then be used to find the CF response amplitude. The basic CF response plot is shown in Figure 2.14.

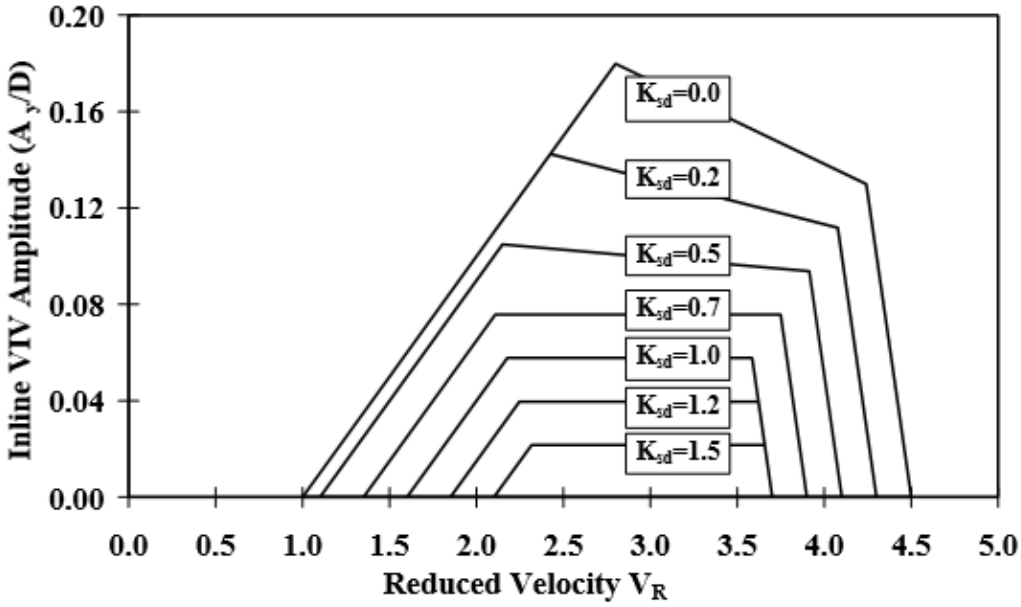

Figure 2.13. In-line VIV response amplitude as a function of V_R and K_s (taken from DNV, 2006).

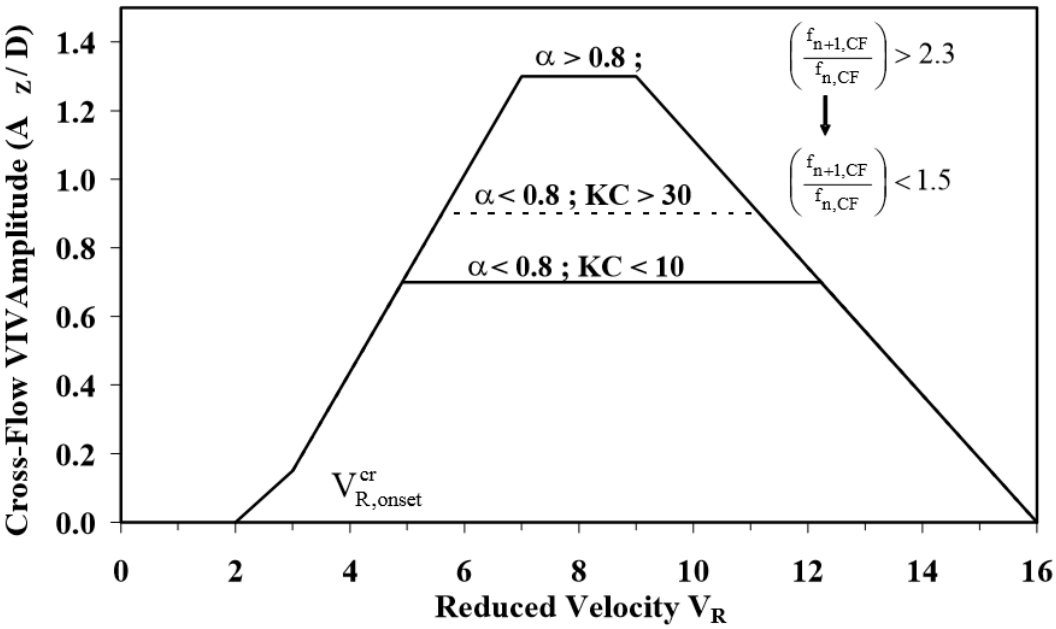

Figure 2.14. CF response model as a function of V_r and *KC* (taken from DNV, 2006).

Plots like the ones shown in Figure 2.13 and 2.14 are conservative if the experimental results used to make these plots are representative for the case considered. The response model

approach based on DNV-RP-F105(2006) use plots like these to predict the VIV response of mainly free spanning pipelines.

Flow based models (CFD)

Flow based models are very promising tools when it comes to the prediction of VIV. They use a combined simulation of fluid flow (simulated by CFD models) and the response of the structure (usually simulated by a Finite Element Model). The problem with these models is that they require long computing times for ordinary computers and hence are normally not economical to use.

However, there are some institutions that have developed methods where CFD is used to analyse risers in a less time-consuming way. This is done by using many 2D CFD planes to model a riser. The oscillating beam will build up the needed correlation to excite vibrations by providing communication between the planes. Because of this, no hydrodynamic coupling between planes are needed, and there will be a reduction in computation time. Nevertheless, these methods are still not commonly used for practical engineering cases because they are still more time-consuming than other software which use force based models (Larsen, 2011).

Force based models

Force based models are based on Morrison's equation for hydrodynamic forces. They use added mass, force, and damping coefficients to describe the fluid structure interaction. Many computer programs for VIV analysis uses a force based model, for example VIVANA (Sintef Ocean, 2016) and SHEAR7 (MIT, 2016). These programs typically use a model based on experimental values for hydrodynamic forces in combination with a model of the structure, often a finite element model (FEM). Normally default curves for added mass, force, and damping coefficients, based on forced oscillation tests, are available. However, the user can often input other data if necessary.

Computer programs of this type are the most common engineering tools used for VIV analysis today.

2.4. VIV Mitigation

The consequences of VIV can be reduced by either changing the properties of the structure, or the properties of the flow around the structure. There are many ways to do this, some are described in the sections below.

2.4.1. Avoid resonance

Resonance can be avoided by keeping the reduced velocity below 1. Equation 2.3 shows that to achieve a lower reduced velocity, the current velocity U should be decreased, or the diameter or eigenfrequency of the structure should be increased. U can obviously not be changed and should hence be viewed as a constant. D can also be viewed as a constant since a certain diameter is required to have flow assurance. This means that the only way to keep the reduced velocity below 1 is by increasing the eigenfrequency of the structure. This can be done by making the structure stiffer.

2.4.2. Increase the stability parameter K_s

Figure 2.13 shows that the vibration amplitude is larger for small K_s and so is the reduced velocity range in which the vibration can occur. Hence, an increase of the stability parameter K_s can reduce the vibration amplitude and the occurrence of VIV. K_s can be increased by increasing the system damping, or by increasing the effective mass of the structure.

2.4.3. Add vortex suppression devices

A more common way to supress VIV, is by adding vortex suppression devices on the structure. According to Larsen (2011) the vortex suppression devices can be categorised according to the way they influence the vortex shedding:

- surface protrusions which initiate separation of the flow,
- devices which brakes the flow into several smaller vortices,
- near wake stabilizers.

Common for all categories is that they interrupt the boundary layer formation, and thus the vortex formation. Some common vortex suppression devices are shown in Figure 2.15.

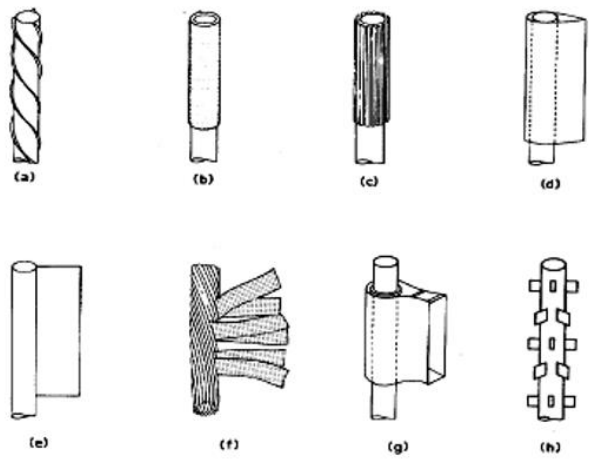

Figure 2.15. Vortex suppression devices (taken from Larsen, 2011).

2.5. Fatigue Damage Assessment

Fatigue failure is failure well below the yield stress of a structures material. This is due to crack-like defects that exist in every material. When the material is subjected to a sufficiently large cyclic stress these defects will grow and eventually cause fatigue failure. As fatigue failure occurs when a structure is subjected to cyclic loading, fatigue failure is common for structures subjected to dynamic loading (Jia, 2014).

There are mainly three approaches used to assess the damage due to fatigue:

- the Stress-based/S-N curve based approach, which is associated with high cycle fatigue,
- the Strain-based approach, which is associated with low cycle fatigue,
- fracture mechanics.

The stress based/S-N based approach is the most commonly used of the above approaches. This is because of its simplicity and accuracy (Jia, 2014).

2.5.1. The stress based approach

The stress based approach is based on the use of S-N curves which characterize the performance of a material subjected to high cycle fatigue. These curves show the log-linear relationship between the stress range *S* and the number of load cycles to failure *N*.

S-N curves based on data obtained from numerous fatigue tests, under different constant stress amplitudes, are called mean S-N curves and are expressed as:

$$\log N = \log A - m \times \log S \tag{2.13}$$

where *N* is the number of stress cycles of the stress range *S* to failure. *A* is a constant related to the mean S-N curve and *m* is the inversed slope of the S-N curve. Both *A* and *m* are found from test data. The mean S-N curve gives a 50% failure probability and is therefore not used for engineering purposes (Jia, 2014).

S-N curves with different probabilities of failure can be found from statistical analysis of fatigue data. For civil engineering applications, the design S-N curves follows the mean-minus-two-standard-deviation of the mean curve. These design S-N curves gives a failure probability of 2.4 % and are expressed as:

$$\log N = \log A - 2 \times \sigma_{\log N} - m \times \log S \tag{2.14}$$

where $\sigma_{\log N}$ is the standard deviation of $\log N$ (Jia, 2014).

Figure 2.16 shows the difference between a mean curve and the corresponding design curve following the mean-minus-two-standard-deviation approach.

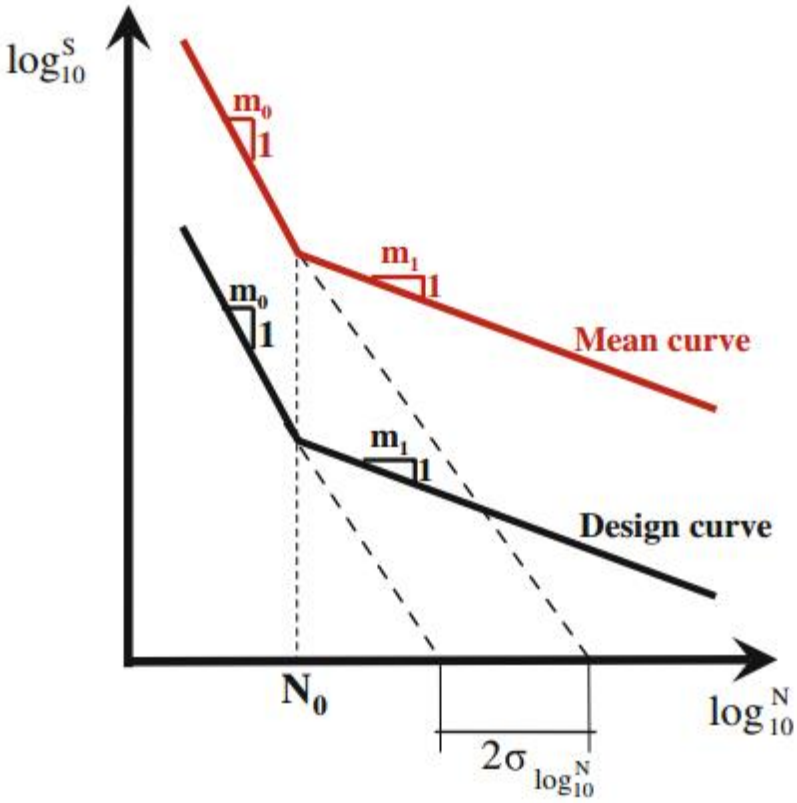

Figure 2.16. Illustration of a mean and a design S-N curve (taken from Jia, 2014).

2.5.2. Fatigue damage

To calculate the cumulative fatigue damage on a structure the Palmgren-Miner rule can be used. This rule assumes that the fatigue damage produced by an individual stress cycle is constant:

$$D_i = \frac{1}{N_i} \tag{2.15}$$

D_i is the fatigue damage produced by stress cycle i, and N_i is the number of stress cycles of the stress range S_i to failure.

The rule also implies that the fatigue damage for a stress history with changing stress ranges can be calculated using linear accumulation of the partial fatigue damage produced by individual cycles. The accumulated fatigue damage(D) is given by:

$$D = \sum_{i=1}^{k} \frac{n_i}{N_i} \tag{2.16}$$

where n_i is the total number of stress cycles of the stress range S_i, and k is the number of different stress ranges S (Chen et al., 2011).

2.6. Literature Review

Since 1998 the free span design guideline, DNV guideline no.14, by *Det Norske Veritas* has been used to estimate the VIV response and associated fatigue damage for free spanning pipelines. In 2002, this guideline was updated and replaced by DNV-RP-F105 (2002).

When the deep-water gas field Ormen Lange was to be developed, the decision to transfer the gas from reservoir to shore using pipelines was made. During the early phases of pipeline routing it became clear that the pipelines needed to cross a very uneven seabed. Hence, numerous of free spans were needed to make this project feasible and to save seabed intervention costs. Moreover, measurements showed that sea bottom currents had significant velocities in this area. Because of this, a model test program within the Ormen Lange project was initiated. Its purpose was to investigate the VIV response of long free spans, and free span areas where interaction between the VIV response of numerous modes could occur (multi-mode response). From these tests, and test data from other sources, an Ormen Lange specific design guideline based on the existing DNV-RP-F105 (2002) was developed (Søreide et al., 2005) This eventually led to an update of the DNV-RP-F105 (2002), to incorporate multi-modal response and multi-span analysis, to the current version DNV-RP-F105 (2006). This version is a widely used design approach for free spanning pipelines today.

However, some semi-empirical methods can also be used for free spanning pipelines. A study was done by Passano et al. (2010) where the VIV predictions from the semi-empirical program VIVANA was compared to experimental results from the Ormen Lange model test. The

conclusion was that the VIVANA version at that time was not able to give a good prediction of the multi-modal response and hence gave too high response frequencies compared to the test data. Apart from this limitation, this version of VIVANA (with no interaction between CF and IL response) gave promising results.

Hariharan et al. (2004) performed a study to show a subsea rigid jumper susceptability to IL VIV due to low sea bottom current velocities. The finite element analysis software ANSYS (ANSYS, 2015) was used to do the static and modal analysis. Then the IL and CF response and fatigue lives were found using DNV-RP-F105 (2006). Their conclusion was that an IL VIV response would be present at these low sea bottom current velocities, and that the high probability of such currents occuring results in a high fatigue damage prediction. However, at the time of the study there were no test data or observations available that could confirm that IL VIV actually occurs for rigid jumpers subjected to such low current velocities.

Holmes and Constantinides (2010) showed how a CFD code could be used to predict VIV response of a rigid jumper subjected to seabed currents. To shorten the computational time, a separate modal analysis was used to find the eigenfrequencies and eigenvectors of the rigid jumper system and then inputted into the CFD analysis. In this study, only the displacements due to VIV for currents normal to the rigid jumper with velocities from 0.1m/s to 0.5m/s were considered. Both the displacements for a rigid jumper with a straked buoyancy section and the displacement for a bare rigid jumper were considered. The conclusion was that both IL and CF VIV could occur for rigid jumpers subjected to current. Although none of the rigid jumpers experienced very large vibration amplitudes (IL or CF) for the various currents, the rigid jumper with the straked buoyancy section experienced vibrations with significantly less amplitudes than the bare rigid jumper.

A study by Deka et al. (2013) assessed the VIV induced fatigue damage of a rigid jumper using SHEAR 7. ANSYS was used to perform the modal analysis of the rigid jumper, and the results were inputted into SHEAR 7 which was used to predict the VIV amplitude. The fatigue damage was calculated using the fatigue assessment method given in DNV-RP-F105 (2006) with the needed values extracted from SHEAR 7. These fatigue damage results were compared to the fatigue damage results obtained by using a combination of DNV-RP-F105 and ANSYS (where ANSYS performs the modal analysis, and DNV-RP-F105 predicts the response and fatigue damage). The conclusion was that the SHEAR 7 approach gave less conservative results than the response model approach based on DNV-RP-F105.

In Wang et al. (2013) the results from a rigid jumper VIV model test done in 2012 by ExxonMobil were presented. The test was done using a towing test rig to expose a small-scale rigid jumper model to flow conditions simulating uniform sea bottom currents. Numerous tests were performed, with different orientations and with different flow speeds, for an “M” shaped rigid jumper, with and without strakes. The purpose of this experiment was to obtain data that later could be used as benchmark data for validating different VIV prediction approaches. Moreover, to identify what orientations and flow speeds that could lead to VIV of the rigid jumper.

Based on the results presented by Wang et al. (2013), Zheng et al. (2015) presented two different approaches to analyse the data from the model test. These approaches could be used to make similar response curves as shown in Figure 2.13 and 2.14. The first method is the spectral analysis method which focuses on the response at a point of the rigid jumper. The second method is the modal scalar analysis method which focuses on the global response of the rigid jumper. These methods are dependent on data from model tests and cannot be used for geometries where model test data does not exist. Currently, the model test data from the tow test done by ExxonMobil on an “M” shaped rigid jumper is the only model test data available for any rigid jumper system.

Nair et al. (2011) presented a methodology to calculate the torsional fatigue damage due to VIV for planar and multi-planar rigid jumpers. They concluded that the torsional contribution to the fatigue damage due to VIV could be significant for certain rigid jumper shapes, and hence should be considered in the fatigue damage assessment of rigid jumpers. Nair et al. (2013) showed that the torsional contribution due VIV can be neglected for jumpers solely consisting of free spans. However, for all other jumper shapes the torsional effects due to VIV should be considered in the fatigue damage assessment.

Chapter 3: VIV Response Estimation Methodology

To do a fatigue damage assessment of a rigid jumper/spool subjected to VIV, the VIV response must be known. In this thesis, two different VIV analysis approaches are to be used to predict the VIV response of a rigid jumper, the response model approach based on the response models in DNV-RP-F105 (2006) and VIVANA.

3.1 The Response Model Approach

DNV-RP-F105 was developed for free spanning pipelines, and its objective is *"to provide rational design criteria and guidance for assessment of pipeline free spans subjected to combined wave and current loading"* (DNV, 2006). The DNV-RP-F105 uses response models, based on empirical data, to predict the VIV amplitudes of free spanning pipelines. However, these models can also be used to evaluate other subsea cylindrical structural components like rigid jumpers and spools. If so, special consideration should be given to the following conditions:

- the uniform current assumption,
- detailed finite element model (FEM) is normally used to find the eigen-frequencies and mode shapes,
- the L/D ratio should be within the design range of the DNV-RP-F105 (2006),
- the structural element must not be in a location where wave-induced VIV can occur.

3.1.1 The DNV-RP-F105 response models

The response models from DNV-RP-F105 (2006) are empirical models which gives the maximum steady state VIV amplitude response. The models are only valid for the following conditions:

- IL VIV in steady current, and current dominated conditions.
- CF VIV induced IL motion (relevant for all reduced velocity ranges where CF VIV can occur).
- CF VIV in steady current, and in combined current and wave conditions.

In-line response model

The IL response amplitude depends on the following parameters:

- The reduced velocity, V_R
- The stability parameter, K_S
- The turbulence intensity, I_C
- The flow angel relative to the pipe, θ_{rel}.

The IL response model is used to find the IL VIV induced stress range S_{IL}:

$$S_{IL} = 2 \times A_{IL} \times \left(\frac{A_Y}{D}\right) \times \psi_{\alpha,IL} \times \gamma_s \tag{3.1}$$

where

- A_{IL} is the unit stress amplitude (found from separate modal analysis using FE software)
- $\psi_{\alpha,IL}$ is a correction factor for the particular current flow ratio α,
- γ_s is a safety factor for fatigue given in Table 3.1,
- $\left(\frac{A_Y}{D}\right)$ is the maximum IL VIV response amplitude, normalised with D.

The current flow ratio is given by:

$$\alpha = \frac{U_c}{(U_c + U_{W)}} \tag{3.2}$$

where U_c is the current velocity normal to the pipe, and U_W is the amplitude of the significant wave-induced velocity normal to the pipe.

In wave dominant conditions, IL VIV is reduced. This reduction is accounted for using the below reduction factor:

$$\psi_{\alpha,IL} = \begin{cases} 0 & for\ 0.5 < \alpha \\ \dfrac{\alpha - 0.5}{0.3} & for\ 0.5 < \alpha < 0.8 \\ 1 & for\ \alpha > 0.8 \end{cases} \tag{3.3}$$

The maximum IL VIV response amplitude $\left(\frac{A_Y}{D}\right)$ can be found from the generated IL response model as a function of V_R and K_S. The IL response model generation principle is given in Figure 3.1.

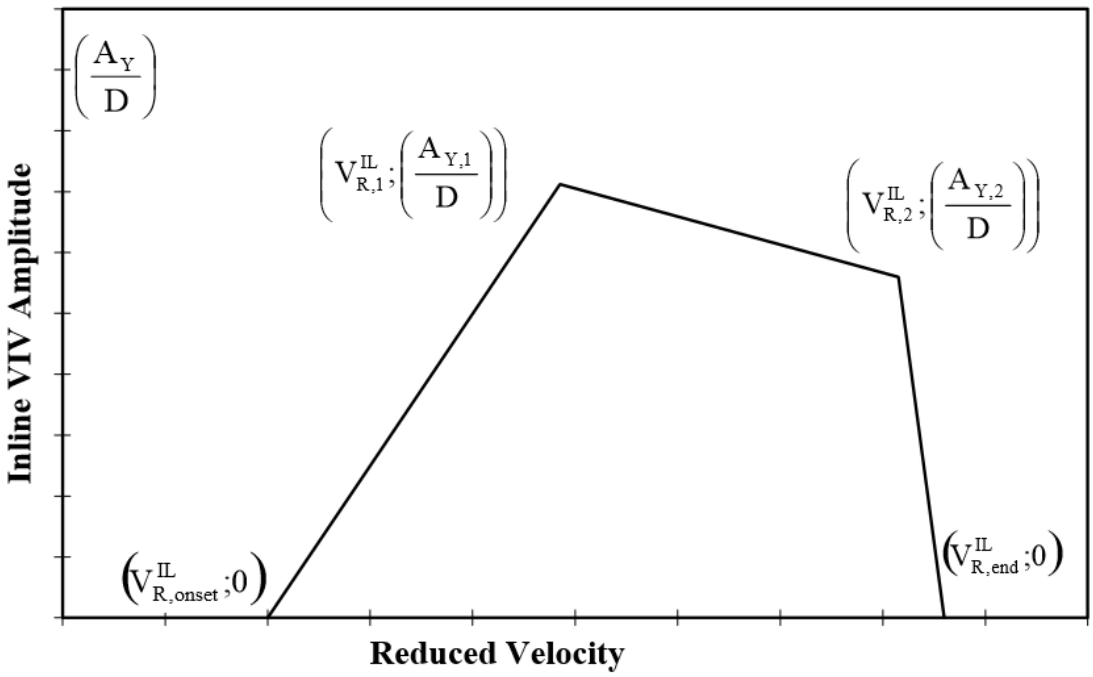

Figure 3.1. IL response model generation principle (taken from DNV, 2006).

In Figure 3.1 the design values for reduced velocity, V_{Rd}, and the design values for the stability parameter, K_{sd}, should be applied when evaluating $\left(\frac{A_Y}{D}\right)$. The design values are given by:

$$V_{Rd} = V_R \times \gamma_f \tag{3.4}$$

$$K_{sd} = \frac{K_s}{\gamma_k} \tag{3.5}$$

Where γ_f and $\gamma_k$are safety factors given in Table 3.1 and 3.2.

Figure 3.1 can be constructed from the following equations:

$$V_{R,onset}^{IL} = \begin{cases} \left(\frac{1.0}{\gamma_{on,IL}}\right) & for \quad K_{sd} < 0.4 \\ \left(0.6 + \frac{K_{sd}}{\gamma_{on,IL}}\right) & for \quad 0.4 < K_{sd} < 1.6 \\ \left(\frac{2.2}{\gamma_{on,IL}}\right) & for \quad K_{sd} > 1.6 \end{cases} \tag{3.6}$$

$$V_{R,1}^{IL} = 10 \times \left(\frac{A_{Y,1}}{D}\right) + V_{R,onset}^{IL} \tag{3.7}$$

$$V_{R,2}^{IL} = V_{R,end}^{IL} - 2 \times \left(\frac{A_{Y,2}}{D}\right) \tag{3.8}$$

$$V_{R,end}^{IL} = \begin{cases} 4.5 - 0.8K_{sd} & for \quad K_{sd} < 1 \\ 3.7 & for \quad K_{sd} \geq 1 \end{cases} \tag{3.9}$$

$$\left(\frac{A_{Y,1}}{D}\right) = \max\left[0.18 \times \left(1 - \frac{K_{sd}}{1.2}\right) \times R_{I\theta,1}; \left(\frac{A_{Y,2}}{D}\right)\right] \tag{3.10}$$

$$\left(\frac{A_{Y,2}}{D}\right) = 0.13 \times \left(1 - \frac{K_{sd}}{1.8}\right) \times R_{I\theta,2} \tag{3.11}$$

The effect of turbulence intensity (I_c) and attack angle (θ_{rel}) is accounted for by the reduction factors $R_{I\theta,1}$ and $R_{I\theta,2}$ which are given by:

$$R_{I\theta,1} = 1.0 - \pi^2 \left(\frac{\pi}{2} - \sqrt{2} \times \theta_{rel}\right) \times (I_c - 0.03) \qquad 0 \leq R_{I\theta,1} \leq 1 \tag{3.12}$$

$$R_{I\theta,2} = 1.0 - (I_c - 0.03)/0.17) \qquad 0 \leq R_{I\theta,2} \leq 1 \tag{3.13}$$

$$I_c = \frac{\sigma_c}{U_c} \tag{3.14}$$

where σ_c is the standard deviation of the velocity fluctuations, and U_c is the mean velocity. If too little or no information is available, I_c should be taken as 5%.

The safety factors for natural frequencies and fatigue are given in Table 3.1 and 3.2. These safety factors are obtained from section 2.6 in DNV-RP-F105(2006).

Table 3.1. General safety factors for fatigue.

Safety factor	Safety class		
	Low	Normal	High
η	1.0	0.5	0.25
γ_k	1.0	1.15	1.30
γ_s	1.3		
$\gamma_{on,IL}$	1.1		
$\gamma_{on,CF}$	1.2		

Table 3.2. Safety factors for natural frequencies, γ_f.

Free span type	Safety class		
	Low	Normal	High
Very well defined	1.0	1.0	1.0
Well defined	1.05	1.1	1.15
Not very well defined	1.1	1.2	1.3

CF response model

Several parameters affect the CF response amplitude, such as:

- the reduced velocity, V_R,
- the stability parameter, K_S,
- the Keulegan-Carpenter number, *KC*,
- the current flow velocity ratio, α,
- the strouhal number, *St*,
- the seabed gap ratio, *(e/D)*, and
- the pipe roughness, *(k/D)*.

The CF response model is used to find the CF VIV induced stress range, S_{CF}, due to combined current and wave flow. S_{CF} is given by:

$$S_{CF} = 2 \times A_{CF} \times \left(\frac{A_Z}{D}\right) \times R_k \times \gamma_s \tag{3.15}$$

where

- A_{CF} is the unit stress amplitude (found from separate modal analysis using FE software),
- R_k is the amplitude reduction factor due to damping,
- γ_s is a safety factor for fatigue given in Table 3.1,
- $\left(\frac{A_Z}{D}\right)$ is the characteristic maximum values of the CF VIV response amplitude, normalized with *D*.

The amplitude reduction factor, R_k, due to damping is given by:

$$R_k = \begin{cases} 1 - 0.15K_{sd} & for \quad K_{sd} \leq 4 \\ 3.2{K_{sd}}^{-1.5} & for \quad K_{sd} > 4 \end{cases} \tag{3.16}$$

The maximum characteristic value of the CF VIV response amplitude, $\left(\frac{A_Z}{D}\right)$, can be found from the generated CF response model as a function of α and KC. The CF response model generation principle is given in Figure 3.2. Also in this figure, the design values for reduced velocity, V_{Rd}, should be applied when evaluating $\left(\frac{A_Z}{D}\right)$.

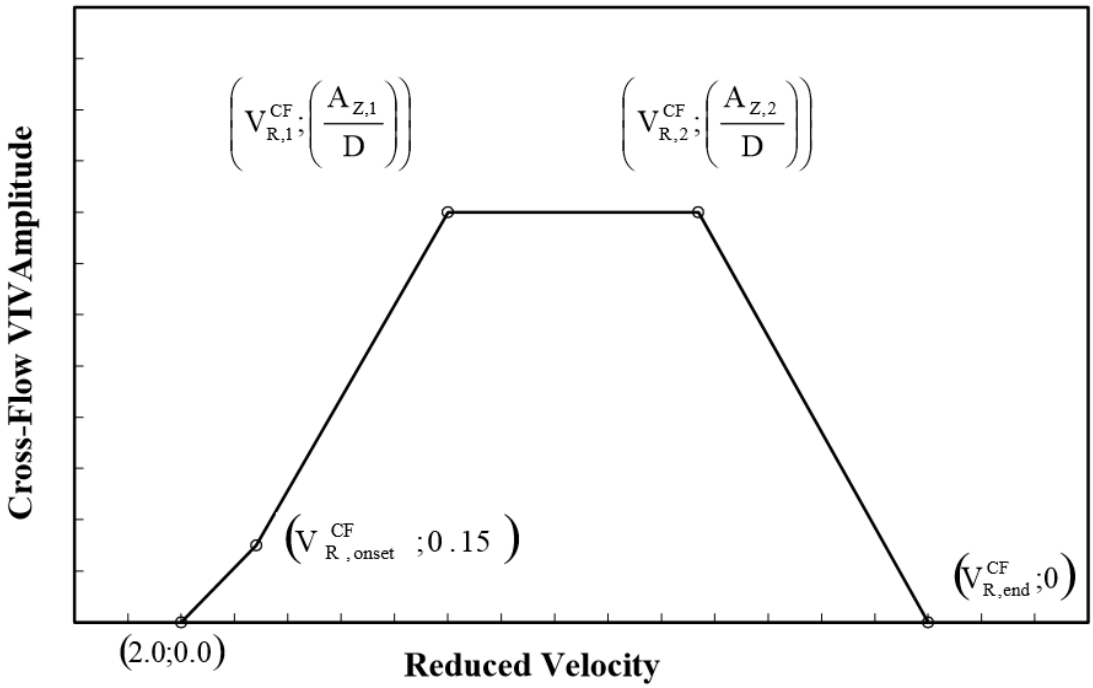

Figure 3.2. CF response model generation principle (taken from DNV, 2006).

Figure 3.2 is constructed using the following equations:

$$V_{R,onset}^{CF} = \frac{3 \times \psi_{proxi,onset} \times \psi_{trench,onset}}{\gamma_{on,CF}} \tag{3.17}$$

$$V_{R,1}^{CF} = 7 - \frac{\left(7 - V_{R,onset}^{CF}\right)}{1.15} \times \left(1.3 - \frac{A_{Z,1}}{D}\right) \tag{3.18}$$

$$V_{R,2}^{CF} = V_{R,end}^{CF} - \left(\frac{7}{1.3}\right) \times \left(\frac{A_{Z,1}}{D}\right) \tag{3.19}$$

$$V_{R,end}^{CF} = 16 \tag{3.20}$$

$$\left(\frac{A_{Z,1}}{D}\right) = \begin{cases} 0.9 & for\ \alpha > 0.8\ and\ \left(\frac{f_{n+1,CF}}{f_{n,CF}}\right) < 1.5 \\ 0.9 + 0.5 * \left(\frac{f_{n+1,CF}}{f_{n,CF}} - 1.5\right) & for\ \alpha > 0.8\ and\ 1.5 \leq \left(\frac{f_{n+1,CF}}{f_{n,CF}}\right) \leq 2.3 \\ 1.3 & for\ \alpha > 0.8\ and\ \left(\frac{f_{n+1,CF}}{f_{n,CF}}\right) > 2.3 \\ 0.9 & for\ \alpha \leq 0.8\ and\ KC > 30 \\ 0.7 + 0.01 * (KC - 10) & for\ \alpha \leq 0.8\ and\ 10 \leq KC \leq 30 \\ 0.7 & for\ \alpha \leq 0.8\ and\ KC < 10 \end{cases} \tag{3.21}$$

$$\left(\frac{A_{Z,2}}{D}\right) = \left(\frac{A_{Z,1}}{D}\right) \tag{3.22}$$

Where $\left(\frac{f_{n+1,CF}}{f_{n,CF}}\right)$ is the CF frequency ratio of two contributing CF modes.

From the above equations, it is clear that the maximum amplitude is a function of α and KC. However, the $V_{R,onset}^{CF}$ depends on the seabed proximity and the geometry of the trench, if one is present. The effect of seabed proximity and trench geometry is accounted for using the following correction factors:

$$\psi_{proxi,onset} = \begin{cases} \frac{1}{5}(4 + 1.25\frac{e}{D}) & for\ \frac{e}{D} < 0.8 \\ 1 & else \end{cases} \tag{3.23}$$

$$\psi_{trench,onset} = 1 + 0.5\frac{\Delta}{D} \tag{3.24}$$

$$\frac{\Delta}{D} = \frac{1.25d - e}{D}\ \ where\ \ 0 \leq \frac{\Delta}{D} \leq 1 \tag{3.25}$$

The relationship between the trench depth *d*, the eccentricity *e*, and the pipe diameter *D* is given in Figure 3.3.

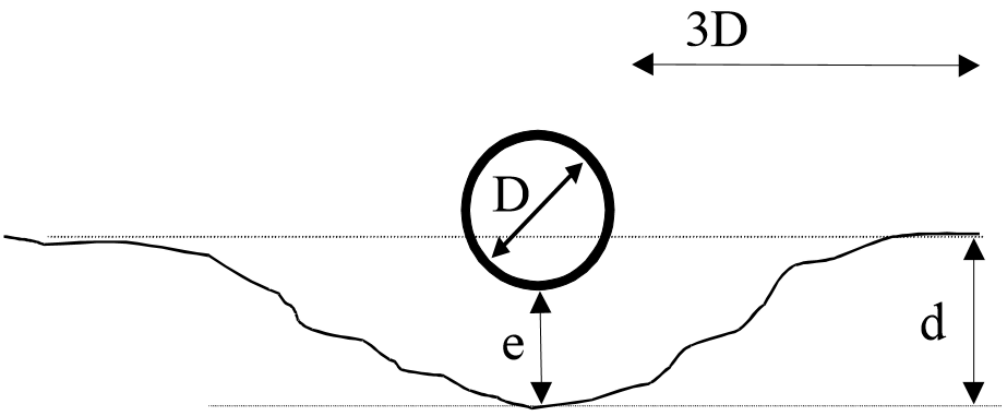

Figure 3.3. Relationship between the trench factors *d*, *e* and *D* (taken from DNV, 2006).

CF induced IL VIV

The DNV-RP-F105 also provides a method for determining the CF induced IL VIV by using the CF and IL response models.

The IL mode with frequency closest to twice the dominant CF response frequency ($f_{n,CF-RES}$) is chosen as the dominant CF induced IL mode.

$$f_{n,CF-RES} = f_{n,CF} \times \sqrt{\frac{\left(\frac{\rho_s}{\rho}\right) + C_a}{\left(\frac{\rho_s}{\rho}\right) + C_{a,CF-RES}}} \tag{3.26}$$

Where:

- $\left(\frac{\rho_s}{\rho}\right)$ is the specific mass ratio between pipe mass and displaced water,
- $C_{a,CF-RES}$ is taken from Figure 3.4.
- C_a is the added mass in still water given by:

$$C_a = \begin{cases} 0.68 + \dfrac{1.6}{1 + 5 \times (\frac{e}{D})} & for\ \dfrac{e}{D} < 0.8 \\ 1 & for\ \dfrac{e}{D} \geq 0.8 \end{cases} \tag{3.27}$$

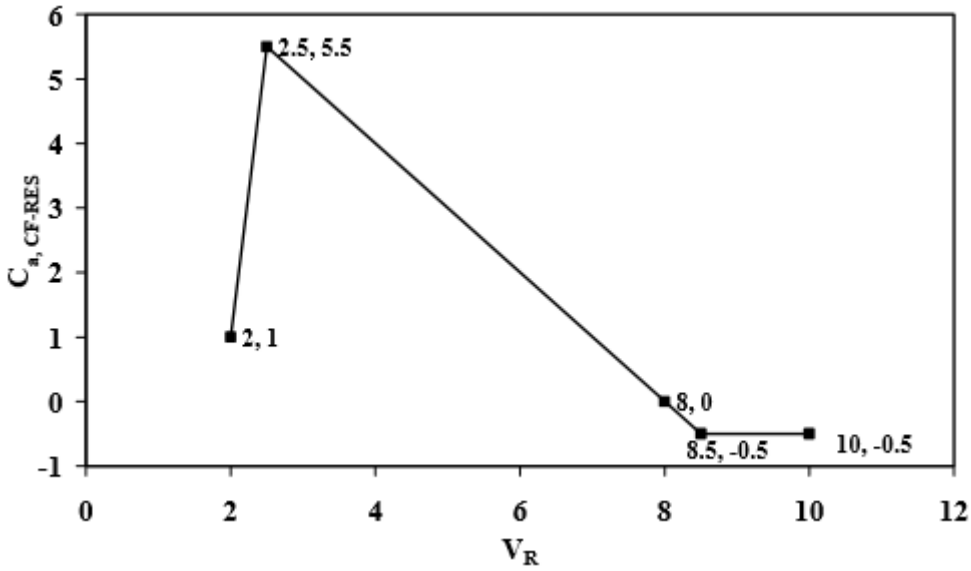

Figure 3.4. Added mass coefficient $C_{a,CF-RES}$ (taken from DNV, 2006).

The stress range for the IL mode that is potentially oscillated by CF induced IL motion, is taken as:

$$S_{i,IL} = \max\left(S_{i,IL}\,, S_{j,IL-CF}\right) \rightarrow S_{i,IL} = \max\left(\left(\frac{A_y}{D}\right) \times \psi_{\alpha,IL}\,, 0.4 \times \left(\frac{A_{Z,dom}}{D}\right) \times R_k\right) \tag{3.28}$$

where

$$S_{i,IL} = 2 \times A_j \times \left(\frac{A_y}{D}\right) \times \psi_{\alpha,IL} \times \gamma \tag{3.29}$$

$$S_{j,IL-CF} = 2 \times 0.4 \times A_j \times \left(\frac{A_{Z,dom}}{D}\right) \times R_k \times \gamma \tag{3.30}$$

3.2 The Force Model Approach - VIVANA

VIVANA is a finite element based semi-empirical software developed by SINTEF Ocean and NTNU to predict the VIV response of slender structures. Added mass, force, and damping coefficients are used to describe the fluid structure interaction (Passano et al., 2016).

VIVANA is not a stand-alone program. It is linked to the analysis program RIFLEX, which provides VIVANA with a description of the structure and its static shape. Thus, in order for VIVANA to predict the VIV response an initial RIFLEX analysis of the structure is needed. The system modelling and the environmental data is done in the RIFLEX module INPMOD, and the non-linear static analysis of the modelled system is done in the RIFLEX module STAMOD. (MARINETEK, 2016) Figure 3.4 illustrates the link between RIFLEX and VIVANA.

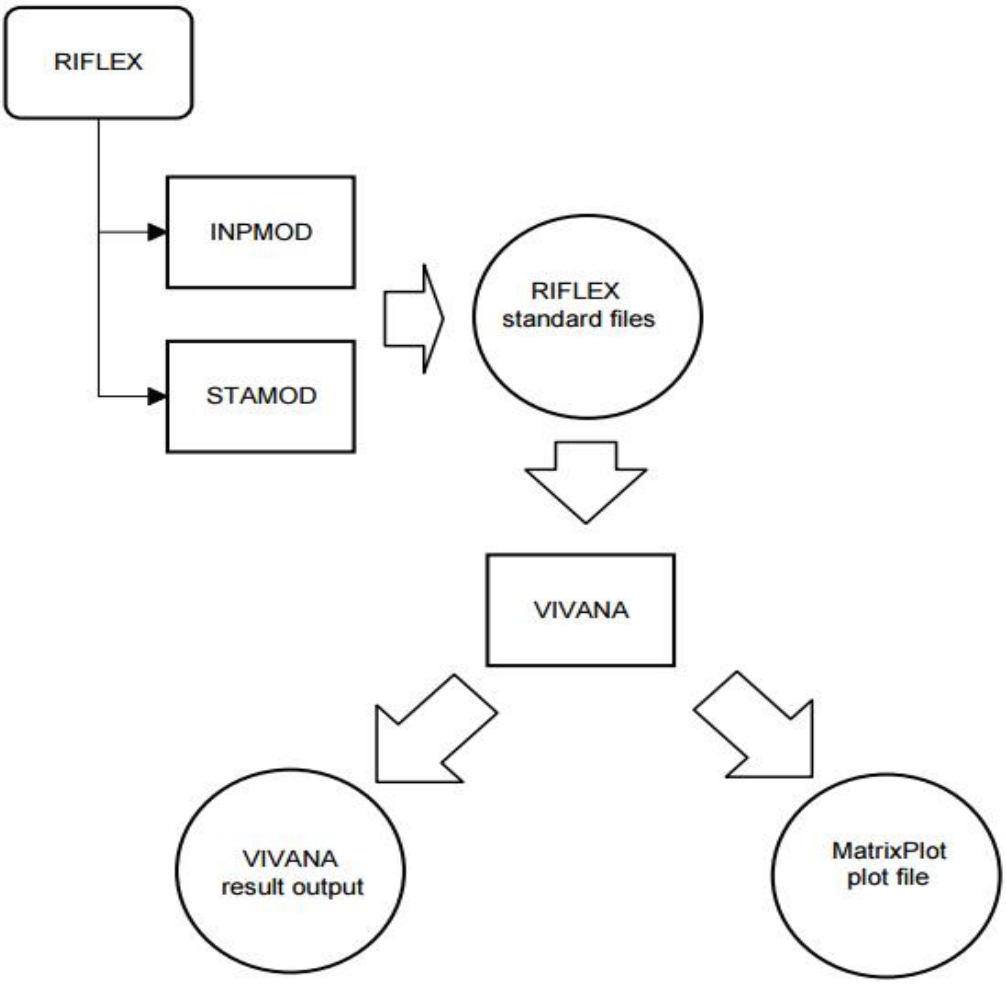

Figure 3.5. Components of the VIVANA program system (taken from MARINETEK, 2016).

RIFLEX can analyse a variety of slender marine structures, for example free spanning pipelines, flexible risers, umbilicals and tendons. Hence, VIVANA can also analyse such structures. The current RIFLEX version, and hence also VIVANA (version 4.8), can analyse 3D shaped slender structures with arbitrary geometries subjected to 3D current profiles.

3.2.1 VIVANA analysis procedure

VIVANA offers 3 analysis options:

1. CF response,
2. pure IL response,
3. combined CF and IL response.

The three options all follow the same analysis procedure when predicting the VIV response of slender structures. However, they use different strategies to find possible response frequencies. For analysis options 1 and 2, the added mass is adjusted for each eigenfrequency until the two are consistent. The difference between these two analysis options is that the added mass coefficients are different. The added mass coefficients for CF response only are found from curves based on experimental data from Gopalkrishnan (1993) whereas the added mass coefficients for pure IL response are found from curves based on experimental data from Aronsen (2007).

For analysis option 3, the possible CF response frequencies are first identified using the strategy for option 1. Then the IL added mass is adjusted to obtain an IL response frequency that is twice the CF frequency. (Passano et al., 2010).

The VIVANA analysis procedure consists of the 6 following steps obtained from Passano et al. (2016):

Step 1: Static analysis

The structure and its environment is modelled in RIFLEX which also performs a static analysis to find the static shape of the structure. When this is known, the normal flow velocity along the structure can be found and the results transferred to VIVANA.

Step 2: Eigenvalue analysis in still water

The eigenfrequencies and associated mode shapes of the structure are found. The eigenvalue analysis is performed by inputting the added mass for the structure in still water. To find all frequencies that can give VIV, called active frequencies, enough eigenfrequencies needs to be found. The number of eigenfrequencies to be found can be inputted by the user. The possible active frequencies can be found by considering the maximum vortex shedding frequency.

The results from the eigenvalue analysis are given in terms of discrete eigenvectors, Φ_i, and their associated eigenfrequencies, ω_i. The results are found from solving the eigenvalue problem which says that all eigenvector solutions need to satisfy the following equation:

$$(M_0 - {\omega_i}^2 K_0)\Phi_i = 0 \tag{3.31}$$

where *M* is the mass matrix and *K* is the stiffness matrix.

Step 3: Identification of possible excitation frequencies

The added mass under VIV conditions is different from the added mass in still water, and will depend on the response frequency. Because of this, the calculated possible active frequencies cannot be taken directly as correct response frequencies. So, to find the actual response frequency candidates an iteration needs to be performed for each possibly active eigenfrequency. This iteration is explained in the following:

- assume that the response frequency is equal to the still water eigenfrequency

$$f_{osc,i}^k = f_{n,i}^k \tag{3.32}$$

  where *k* is the iteration step.

- Calculate the non-dimensional frequency along the structure

$$\hat{f}_i^k(z) = \frac{D(z) f_{osc,i}^k}{U(z)} \tag{3.33}$$

- Use the calculated non-dimensional frequency to find the added mass coefficient from built-in curves. These curves are based on experimental data from Gopalkrishnan (1993) for CF oscillations and from Aronsen (2007) for IL oscillations. The curves can also be user defined. Now the added mass matrix, and hence total mass matrix, needs to be re-calculated.

- Use the new mass distribution to solve the eigen value problem (eqs.3.31) and identify the wanted eigenfrequency $f_{n,i}^{k+1}$.

- Finally, use the below equation to test for convergence.

$$\left|f_{n,i}^{k+1} - f_{n,i}^{k}\right| \leq \epsilon \tag{3.34}$$

  ϵ is a built-in convergence criterion.
  If the test for convergence fails, go to the first step and do a new iteration. If the test is satisfied, $f_{n,i}^{k+1}$ can be accepted as a possible response frequency, $f_{osc,i}$.

Step 4: Dedication of excitation zones

As explained in section 2.3.1, for cases of long and slender structures, many eigenfrequencies are active (can be excited) and hence the VIV response of such structures is complicated. There does not exist any model today that can reproduce the response observed in these structures. However, there exist an approach that is commonly accepted. In this approach, the key is to define the excitation zone for a specific frequency and calculate the response that frequency gives independent on other frequencies that are active. There are two ways of doing this, time sharing and space sharing. In VIVANA both methods can be used.

Step 5: Calculation of the CF response

The CF response at the response frequency found in step 3 with excitation zones defined in step 4 is calculated using the frequency response method. Because VIVANA uses the frequency response method the dynamic analysis is linear with respect to the structural stiffness. This limitation is for most cases not a problem as the VIV amplitudes are small compared to the

global dimensions of the structures. In order to use the frequency response model to calculate the response, VIVANA assumes that VIV occur at discrete frequencies. Laboratory tests and large-scale measurements support this assumption.

The response is found from the dynamic equilibrium equation which can be written as:

$$M\ddot{r} + C\dot{r} + Kr = R \tag{3.35}$$

The external loads, R, and the response vector, r, will be given by a complex vector and a harmonic time variation:

$$R = Xe^{i\omega t} \tag{3.36}$$

$$r = xe^{i\omega t} \tag{3.37}$$

$$\dot{r} = i\omega xe^{i\omega t} \tag{3.38}$$

$$\ddot{r} = -\omega^2 xe^{i\omega t} \tag{3.39}$$

Hence, the dynamic equilibrium equation can be rewritten as:

$$-\omega^2(M_S + M_H)x + i\omega(C_S + C_H)x + Kx = X_L \tag{3.40}$$

where

- M_S is the structural mass matrix,
- M_H is the hydrodynamic mass matrix,
- C_S is the structural damping matrix,
- C_H is the hydrodynamic damping matrix,
- K stiffness matrix,
- X_L is the excitation force vector.

To solve Equation.3.40 iteration is needed. The iteration process is continued until the response shape and amplitude that give consistency between the response level and applied hydrodynamic coefficients are identified.

The solution can be written as:

$$x = [-\omega^2(M_S + M_H) + i\omega(C_S + C_H) + K]^{-1} X_L = H(\omega) X_L \tag{3.41}$$

where $H(\omega)$ is the frequency response matrix.

Step 6: calculation of the IL response

The IL response is calculated in the same way as the CF response in step 5. However, all hydrodynamic coefficients are different.

Chapter 4: Evaluation of Assessment Methods for Estimating the VIV Response of Planar Rigid Jumpers[#]

Laila Aarstad Igeh[A], Jie Wu[B], Zhenhui Liu[C], Muk Chen Ong[A]

[A] Department of Mechanical and Structural Engineering and Material Science, University of Stavanger, Stavanger, Norway.

[B] SINTEF Ocean, Trondheim, Norway.

[C] Aker Solutions AS, Trondheim, Norway.

Abstract

Rigid jumper (or spool) is an important part of a subsea production system. When subjected to current, vortex induced vibrations (VIV) can occur. This will lead to fast accumulation of fatigue damage. The three-dimensional geometry of the structure means that the flow field and hence the vortex shedding will be complex. Currently, there are no proven design guideline or software available for assessing VIV response of a rigid jumper. Therefore, the objective of the present study is to evaluate the use of the semi-empirical program, i.e. VIVANA, and a response model approach based on DNV-RP-F105(2006) to predict the VIV response of rigid jumpers. These two methods have been used to predict the VIV response of an "M" shaped rigid jumper exposed to varying current speeds hitting the jumper plane at two different angles. The two prediction methods are evaluated against the existing experimental data.

When the current hits the jumper plane at a 10° angle, VIVANA seems to give fairly good predictions on the response frequency/mode and maximum displacement amplitude for most current speeds. The response model approach, on the other hand, seems to give large over-predictions of the displacement amplitude for most current speeds at this current direction.

[#]This is a journal paper which will be submitted to *Marine Structures.*

When the current has a 90° angle relative to the jumper plane, both VIVANA and the response model approach give good predictions with respect to the maximum jumper response.

Keywords: rigid jumper, rigid spool, VIV, response model, force model, VIVANA, DNV-RP-F105

1. Introduction

Today, most new field developments consist of a subsea production system. Rigid jumpers (also refereed as spools in some places) are important parts of these systems as they accommodate pipeline expansion and contraction due to changes in pressure and temperature, or due to movements of connected structures.

The rigid jumpers are normally with significant free spans and they could be subjected to seabed currents since they are located near the sea bottom. These seabed currents, if large enough, can lead to vortex induced vibrations (VIV) which can significantly decrease their fatigue life. As failure of a rigid jumper will have severe environmental and economic consequences, a proper fatigue assessment should be done to ensure sufficient fatigue life and avoid fatigue failure.

Semi-empirical programs, such as VIVANA (Sintef Ocean, 2016) and SHEAR7 (MIT, 2016), are widely used by the industry for VIV prediction. These programs solve the system dynamic equilibrium equation by using empirical hydrodynamic force model. They are referred as force model approach in present study. A modal superposition technique is used by SHEAR7 to calculate the response. The response is described by combination of a set of normal modes. While, VIVANA solves the system equation by frequency response method. Consistency between the phase of the load and the phase of the response are maintained. The structural model in VIVANA applies a non-linear three-dimensional (3D) finite element (FEM) formulation. The program is able to work with an arbitrary distribution of tension, mass, stiffness, buoyancy and diameter. Different programs can give similar predictions for a simple structure if the same hydrodynamic force data is used (Voie et al., 2017).

A response model approach has also been developed to evaluate VIV responses of free spanning pipelines as described in DNV-RP-F105 (2006). The maximum VIV displacement amplitude is directly obtained from the response model for given parameters such as reduced velocity,

damping ratio, etc., without solving the dynamic equilibrium equations. This model is calibrated against VIV model test data, but its application is limited to bare cylinders in uniform flow.

Hariharan et. al. (2004) performed a numerical study to show a subsea rigid jumper can be susceptible to VIV even at low sea bottom current velocities. The modal parameters (i.e. eigen-frequency and mode shapes) were obtained from a FEM program, which were used as input parameters to obtain VIV response from the response model. They concluded that an IL VIV response can be present at these low sea bottom current velocities.

Deka et al. (2013) applied SHEAR7 for the VIV assessment of rigid jumpers. The results from the SHEAR 7 approach was compared to the predicted VIV response calculated using the response model approach based on DNV-RP-F105 (2006). The conclusion was that SHEAR 7 was demonstrated to be significantly less conservative than the response model approach.

In recent studies, CFD based fully coupled analysis has been used to assess jumper VIV, see e.g. Holmes & Constantinides (2010). CFD is a robust tool but long computing time must be expected and thus CFD is not yet an engineering tool.

Compared to other slender marine structures, the flow speed normal to the structural members of the subsea rigid jumpers can be three-dimensional even in a uniform flow due to their geometry in planar or multi-planar space. Therefore, the VIV response is complex and current heading dependent. Applying different VIV prediction methods may lead to large differences. However, there is limited validation of the VIV prediction methods against model tests. In addition, the present VIV prediction tools do normally not account the torsional stiffness of the structure. The method to calculate fatigue damage due to combined bending and torsional stress still needs further studies.

In 2012, ExxonMobil performed a rigid jumper VIV model test, see Wang et al. (2013) and Zheng et al. (2015) The purpose of this experiment was to investigate VIV responses of a rigid jumper and obtain benchmark data. Currently, this model test data is the only test data available in open literature for any types of rigid jumpers.

The objective of the present study is to evaluate the use of different VIV prediction methods for rigid jumpers, i.e. the force model based approach, VIVANA, and the response model approach based on DNV-RP-F105 (2006). The global responses of the structure, such as mode number, frequency and displacement amplitude are the main focus of this benchmark study.

The results obtained from these analyses will be compared to the benchmark data from the ExxonMobil model test given in Wang et al. (2013) and Zheng et al. (2015).

Two flow directions, 10° and 90° relative to the jumper plane, were selected for this study. For the 10° flow direction, analyses were performed for 31 different flow speeds varying from 0.05m/s to 0.98m/s. For the 90° flow direction, analyses were performed for 33 different flow speeds varying from 0.05m/s to 0.748m/s. Only bare jumper configurations are considered.

2. Force Model Approach – VIVANA

VIVANA (version 4.8) is a finite element based semi-empirical program developed by SINTEF Ocean and NTNU to predict the VIV response of slender structures. Added mass, excitation force, and damping coefficients are used to describe the fluid structure interaction.

The program is based on the assumption that the response will occur at one or more discrete response frequencies and that these frequencies are eigen frequencies with the added mass in agreement with the non-dimensional frequency corresponding to the response frequency.

The equation of dynamic equilibrium may be written

$$\boldsymbol{M\ddot{r} + C\dot{r} + Kr = R} \tag{1}$$

Where, M, K and C are the structural mass matrix, structural stiffness matrix and structural damping matrix respectively. R is the external load vector, r is the response vector.

The external loads R will in this case be harmonic with frequencyω, but loads at all degrees of freedom are not necessary in phase. It is convenient to describe this type of load pattern by a complex load vector X with harmonic time variation.

$$\boldsymbol{R = Xe^{i\omega t}} \tag{2}$$

The response vector r will also be given by a complex vector x and a harmonic time variation. Hence, we have,

$$\mathbf{r} = \mathbf{x}\mathbf{e}^{\mathbf{i\omega t}} \tag{3}$$

By introducing in the hydrodynamic mass M_H and damping matrices C_H dynamic equilibrium can now be expressed as:

$$-\boldsymbol{\omega}^2(\boldsymbol{M_S} + \boldsymbol{M_H})\boldsymbol{x} + \boldsymbol{i\omega}(\boldsymbol{C_S} + \boldsymbol{C_H})\boldsymbol{x} + \boldsymbol{Kx} = \boldsymbol{X} \tag{4}$$

Where, M_S and C_S are the structural mass and structural damping respectively.

VIVANA can predict:

1. cross-flow (CF) response,
2. pure in-line (IL) response, and
3. combined CF and IL response.

The hydrodynamic added mass and force coefficients are different for the three analysis options, but they all follow the same analysis procedure to predict the VIV response. However, there are differences in the strategies used to find possible response frequencies.

For analysis options 1 and 2, the response frequency is found by adjusting the added mass for each eigenfrequency until the two are consistent. For analysis option 3, the possible CF response frequencies are first identified using the strategy of analysis option 1 (CF response only). Then the IL added mass is adjusted to obtain an IL response frequency that is twice the CF frequency. User defined added mass model can also be used.

The response is solved iteratively in frequency domain. A more detailed description of VIVANA may be found in Passano et al. (2016). Other empirical VIV prediction programs also rely on empirical hydrodynamic force coefficient models, but different methods are applied for calculation of the dynamic responses.

3. Response Model Approach based on DNV-RP-F105

DNV-RP-F105 (2006) was developed for free spanning pipelines to predict fatigue damage due to VIV and direct wave loads. The response models are empirical models providing the maximum steady state VIV response amplitudes as a function of some basic hydrodynamic and structural parameters. The models for estimation of response due to VIV are based on several research and development programs, including the Ormen Lange free spanning pipeline VIV model tests (Nielsen et al., 2002)

The pure IL and CF analysis procedure is as follows:

1. determine which of the modes from the eigenvalue analysis that are IL modes and which that are CF modes. According to DNV-RP-F105 (2006), 3 contributing CF modes and 4 contributing IL modes are considered sufficient to provide accurate fatigue damage estimates.

2. Calculate the design value of the reduced velocity (V_{Rd}) for the different modes, the design value of the stability parameter (K_{sd}), and the Keulegan-Carpenter number(KC)

$$\boldsymbol{V_{Rd} = V_R \gamma_f} \tag{5}$$

$$\boldsymbol{K_{sd} = \frac{K_s}{\gamma_k}} \tag{6}$$

$$\boldsymbol{KC = \frac{U_w}{f_w D}} \tag{7}$$

Where γ_f is a safety factor related to the natural frequency, γ_k is a safety factor related to damping, U_w is the significant wave induced flow velocity and f_w is the significant wave frequency.

3. construct the IL and CF response models. Figure 1 shows a typical IL response curve and Figure 2 a typical CF response curve.

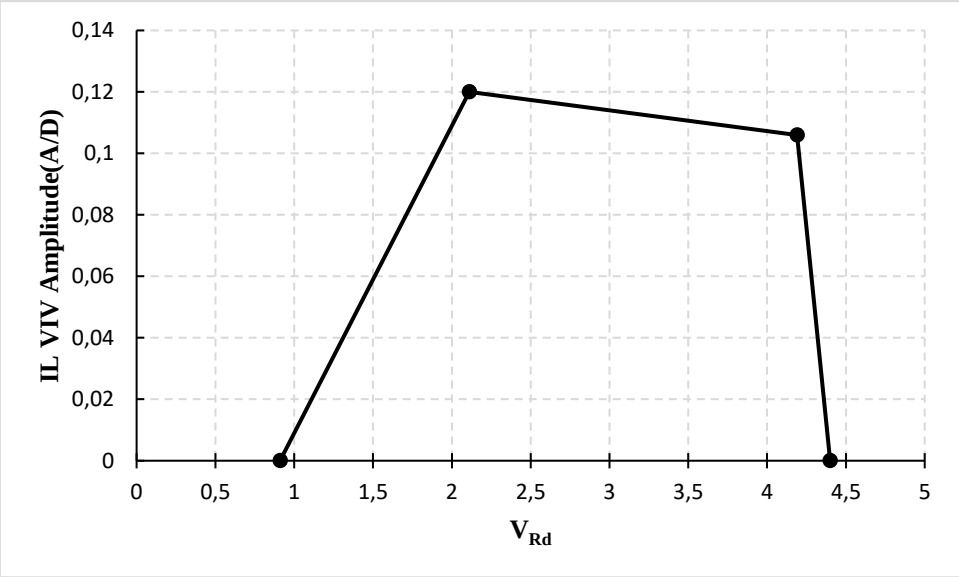

Figure 1. IL response model created based on DNV-RP-F105 (2006).

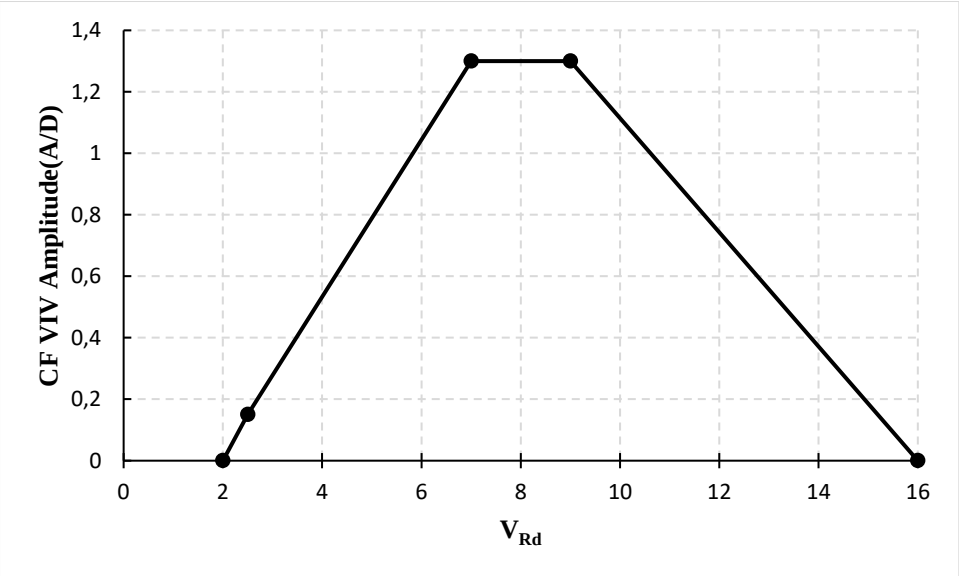

Figure 2. CF response model created based on DNV-RP-F105 (2006).

4. check for multi-mode response using the below criteria

$$\boldsymbol{V_{Rd,CF} > 2 \quad for\ cross - flow} \tag{8}$$

$$\boldsymbol{V_{Rd,IL} > 1 \qquad for\ in - line} \tag{9}$$

5. determine the dominating IL and CF modes. The IL mode associated with the highest response stress is defined as the dominating IL mode. The CF mode that gives the largest response amplitude (A/D) is defined as the dominating CF mode.

6. use the design value of the reduced velocity for the dominating mode and find the maximum amplitude response from the response models.

The response models in the DNV-RP-F105(2006) can also be used to evaluate other subsea cylindrical structural components like rigid jumpers. If so, special consideration should be given to the following conditions:

- the uniform current assumption,
- detailed finite element model (FEM) is normally used to find the eigen-frequencies and mode shapes,
- the L/D ratio should be within the design range of the DNV-RP-F105(2006),
- the structural element must not be in a location where wave-induced VIV can occur.

The main difference between the response model and the force model approach is that the response model approach uses hydrodynamic parameters to determine the VIV response directly without solving the dynamic equilibrium equation of the structure.

4. Jumper VIV Model Test

In 2012, ExxonMobil performed a rigid jumper VIV model test. a model-scale “M” shaped rigid jumper model was towed in still water simulating uniform flow conditions. A more detailed explanation of the VIV model test is given in Wang et al. (2013) The jumper model was towed at three different orientations to achieve flow directions of 10°, 45° and 90° relative to the jumper plane. Numerous test was performed for the three different orientations with flow speed varying from 0.05m/s to 1.241m/s.

A full scale 10” outer diameter “M” shaped rigid subsea production jumper was selected as base case for the model test. The test required that the model-scale jumper to be built had geometry, mass ratio, and torsion- and bending stiffness similar to the base case. To obtain similar geometry and stiffness, aluminium pipes were used to build the model. However, the use of aluminium pipes made the jumper model less massive than the base case. Thus, to increase the mass a fluid, with specific gravity 1.4, was filled inside the model jumper. Nevertheless, this was not enough so additional lead weights were added along the jumper model, making the final mass ratio equal to 2.33.

The jumper model was instrumented with 13 accelerometers to identify the different modes, three strain gauges to measure bending and torsion strain, and two force dynamometers at each end to measure the connection forces and moments. The locations of the accelerometers and the pipe segments are shown in Figure 3. The length of the segments marked in Figure 3 are provided in Table 1.

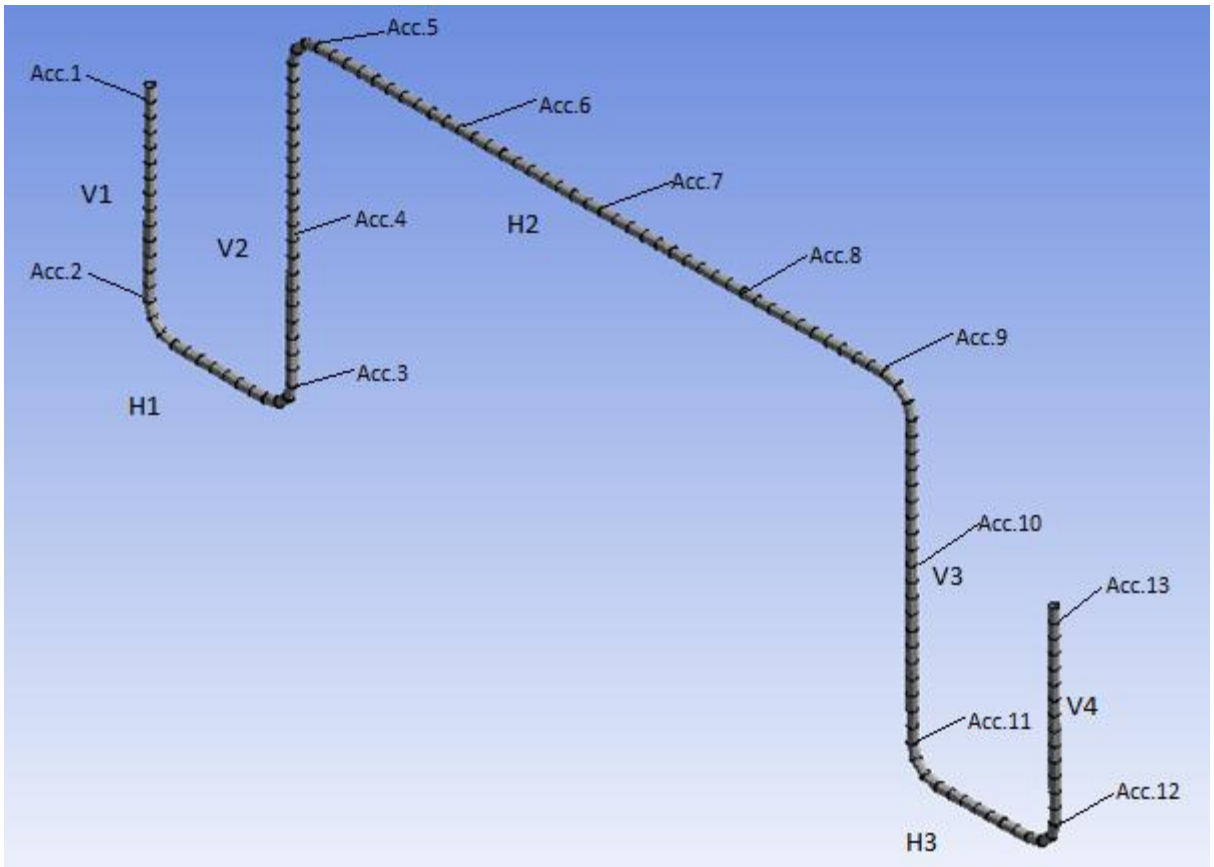

Figure 3. Jumper model with accelerometer and pipe segment locations.

Table 1. Length of each segment in the jumper model.

Segment	Length
V1	1.495m
H1	1.000m
V2	2.323m
H2	4.327m
V3	2.326m
H3	1.000m
V4	1.495m

5. Evaluation and discussion

VIV analyses have been performed using force model based VIV prediction program, VIVANA and the response model approach based on DNV-RP-F105 (2006). The results from these analyses are compared to experimental data given in Wang et al. (2013) and Zheng et al. (2015). The response frequency/mode, and displacement are the main focus of the present study.

5.1. Comparison with force model approach

Table 2 and 3 provides the jumper model properties used to create the finite element model (FEM). The information in these tables were given in Zheng et al. (2015). The internal fluid density in the FEM created in VIVANA was set to 2328,45 kg/m^3 to account for the lead weights distributed along the length of the pipes to increase the mass ratio.

To simplify the finite element model of the jumper, only vertical and horizontal members were used to model the jumper, i.e. no bends at the corners. Also, the jumper ends were assumed to be fully clamped.

A pure IL, and a combined CF and IL analysis have been conducted in VIVANA for varying flow speeds with 10° and 90° directions relative to the jumper plane. In the analyses done in this study, the concurrent response frequency option and the default force coefficient database in VIVANA have been used. The default force coefficients are given in Passano et al. (2016). In Figure 4 the CF excitation coefficient database in VIVANA is presented in a contour plot.

Table 2. Jumper model properties.		
Parameters	Value	Unit
Total jumper length	13.96	M
Pipe density	2700	Kg/m^3
Mass ratio	2.33	-
Outer diameter	0.0605	M
Inner diameter	0.055	M
Wall thickness	0.00277	M
Elastic modulus(E)	6.90 E+10	N/m^2
Bending stiffness(EI)	1.44 E+4	Nm^2
Shear modulus(J)	2.61 E+10	N/m^2
Torsion stiffness(GJ)	1.08 E+4	Nm^2

Table 3. Hydrodynamic properties for the jumper model.			
	Drag Diameter	Drag Coefficient	Added Mass Coefficient
Bare jumper	0.0605 m	1.1	1.0

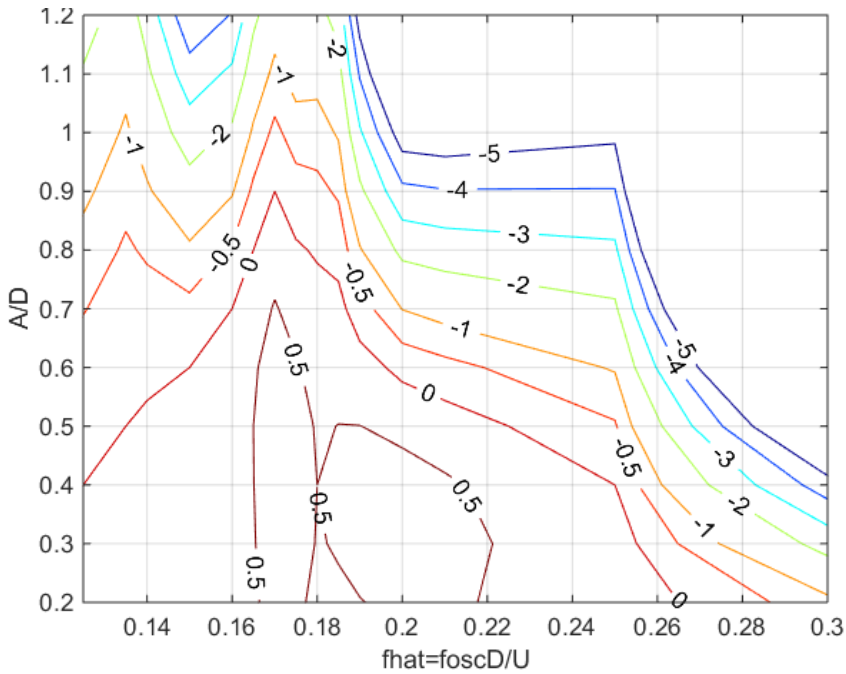

Figure 4. CF excitation coefficient database in VIVANA presented in a contour plot.

5.1.1. Eigenvalue analysis results

The results from the eigenvalue analysis in VIVANA are compared to the eigen frequencies and mode shapes, of the model test jumper, given in Zheng et al. (2015). These results along with the measured values are shown in Table 4 and Figure 5, 6, 7, and 8.

Table 4. Bare jumper mode frequencies.

	From VIVANA	From Zheng et al. (2015)
Mode frequency 1	0.8587 Hz	0.8632 Hz
Mode frequency 2	2.1403 Hz	2.1492 Hz
Mode frequency 3	2.1741 Hz	2.1941 Hz
Mode frequency 4	2.5457 Hz	2.5417 Hz

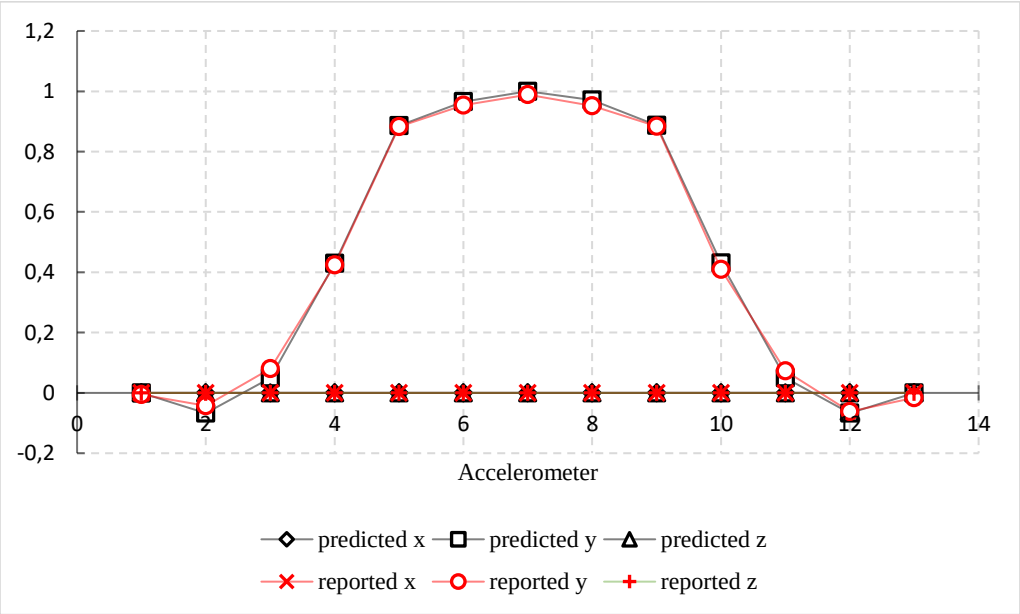

Figure 5. Comparison of predicted mode shape 1 (black lines) and mode shape 1 reported in Zheng et al. (2015) (red lines).

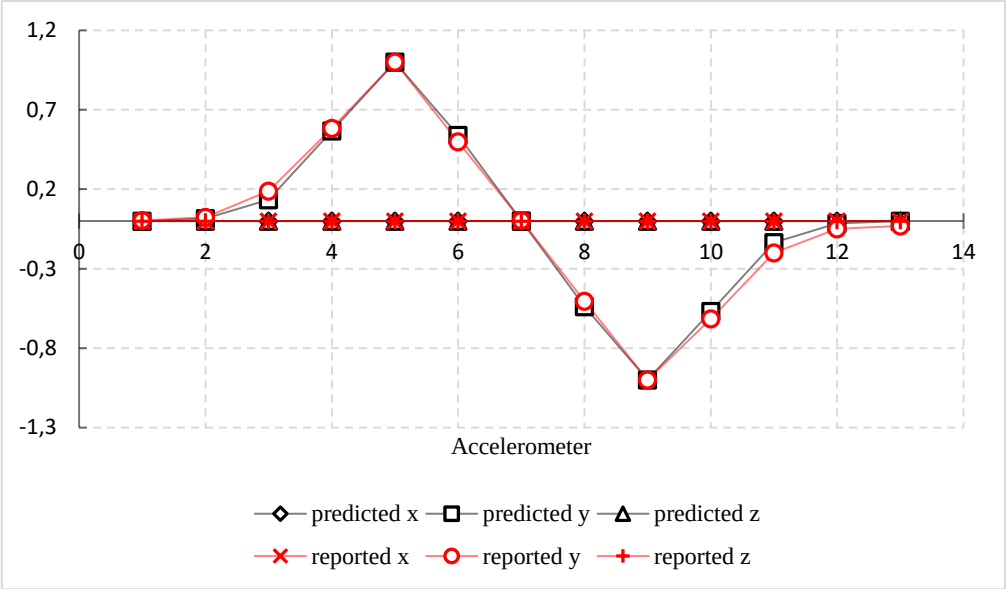

Figure 6. Comparison of predicted mode shape 2 (black lines) and mode shape 2 reported in Zheng et al. (2015) (red lines).

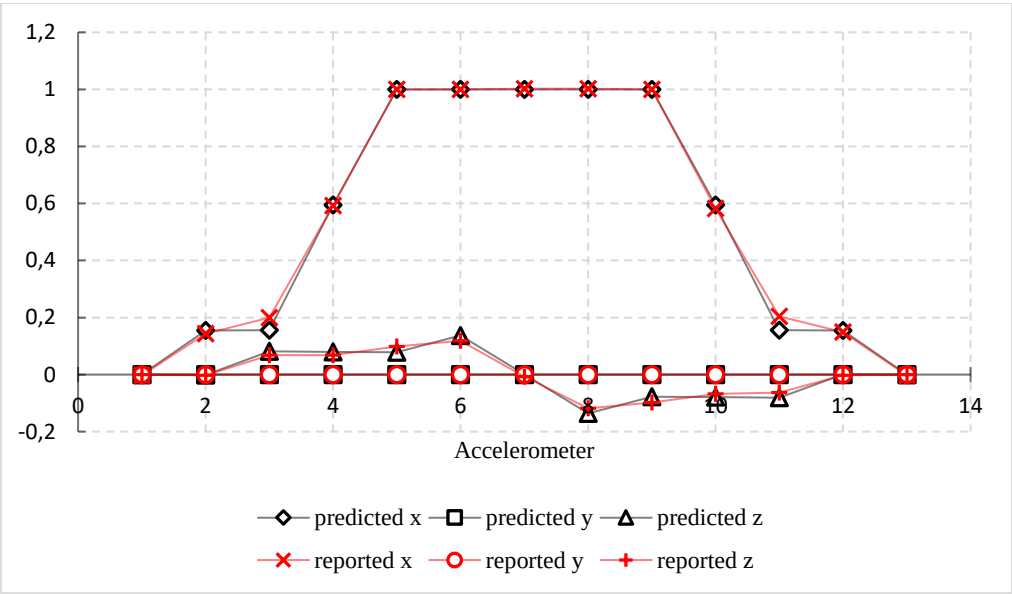

Figure 7. Comparison of predicted mode shape 3 (black lines) and mode shape 3 reported in Zheng et al. (2015) (red lines).

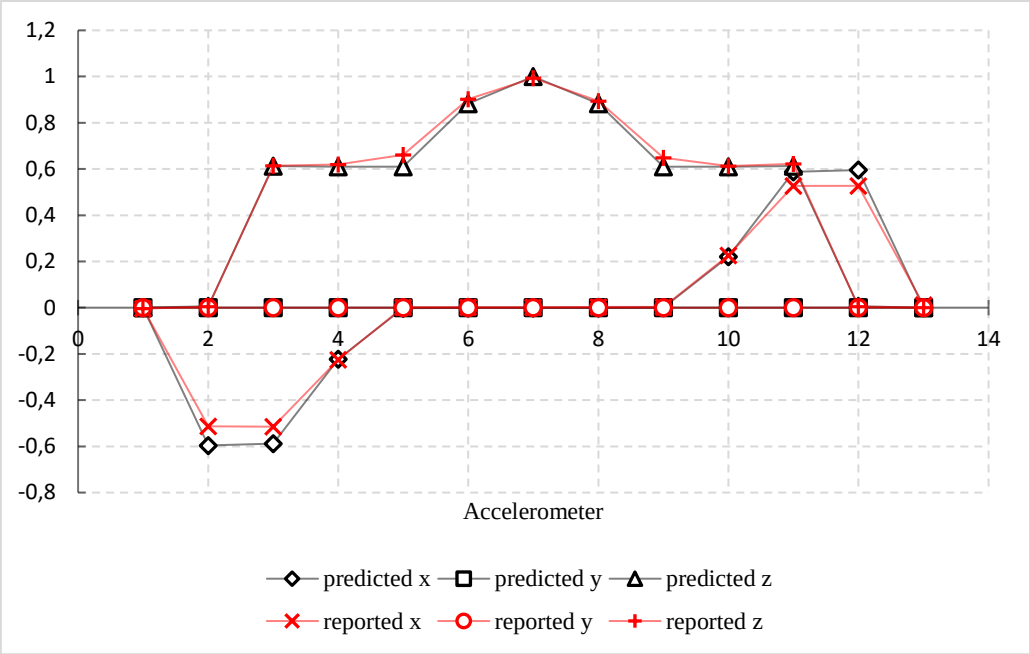

Figure 8. Comparison of predicted mode shape 4 (black lines) and mode shape 4 reported in Zheng et al. (2015) (red lines).

Table 4 and Figures 5, 6, 7, and 8 show that the eigenfrequencies and associated mode shapes calculated in VIVANA agrees well with those given in Zheng et al. (2015). This indicates that the jumper model in VIVANA represents well the ExxonMobil model test jumper. The predicted mode shapes in 3D are given in Figure 9.

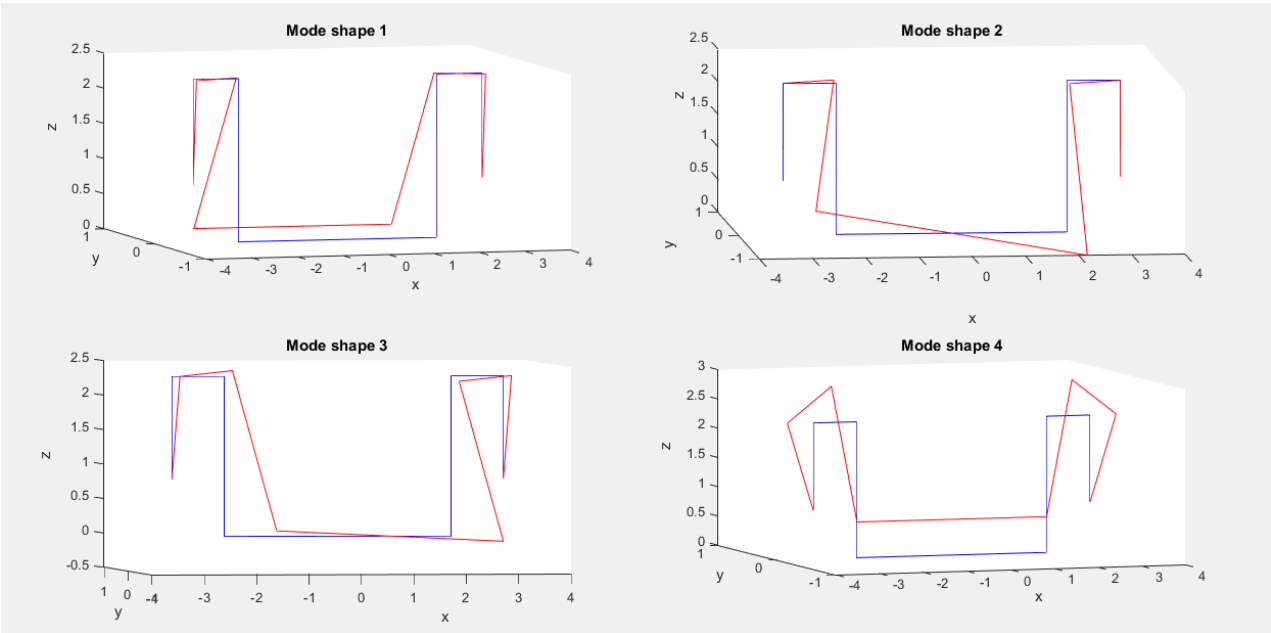

Figure 9. 3D mode shapes.

5.1.2. Prediction of 10° current direction

When the flow hits the jumper plane at a 10° angle, only the vertical members will experience significant VIV as they are the only members exposed to significant flow speed normal to their cylindrical axis. Thus, the normal component of the flow speed is not uniform along the jumper. In this case, IL and CF direction for the vertical structure members corresponds to global x, y direction respectively

Zheng et al. (2015) presented the modal information of the measured response in Figure 10.

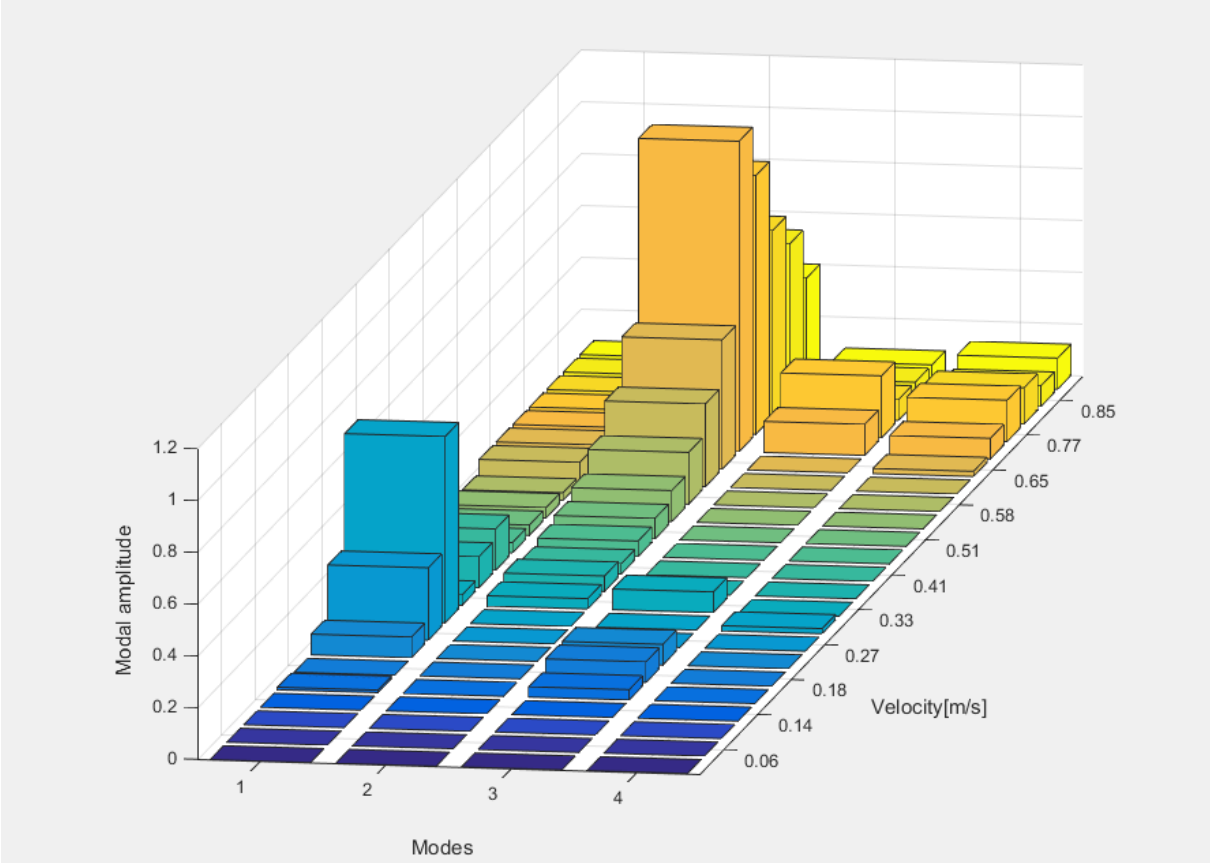

Figure 10. Measured jumper response in terms of mode and its sequence of occurrence with increasing flow speed for the 10° current direction. The measurement data is recreated from Zheng et al. (2015).

Figure 10 shows that mode 3 was first excited at low towing speed around U=0.18 m/s. The vertical structure members are responding to pure IL loading. The jumper deforms in x direction, see Figure 9. With increasing towing speed, mode 1 was excited and vibration in y

direction is expected due to VIV load in CF direction. At higher velocities CF VIV occurs at mode 2 with contributions from mode 3 and mode 4. The measured response in x and z-direction due to CF loading is a result of these contributions.

Figure 11 presents the modal information of the predicted response.

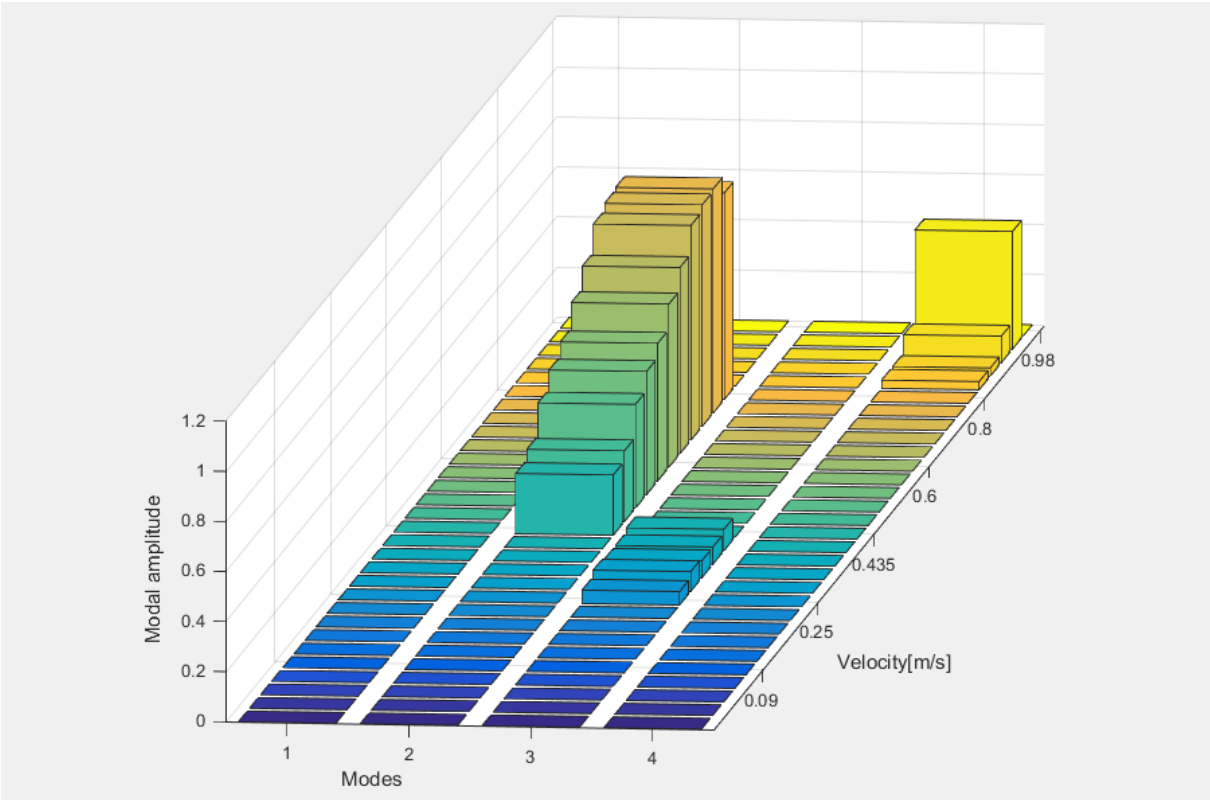

Figure 11. Predicted jumper response in terms of mode and its sequence of occurrence with increasing flow speed for the 10° current direction.

Figure 11 show that VIVANA predicts that mode 3 will be excited due to IL loading for low flow speeds (from 0.206m/s to 0.412m/s). As the flow speed increases mode 2 becomes the excited mode due to CF loading. Mode 1 is not predicted to be a CF response mode because VIVANA predicts that mode 1 is a IL mode for this flow direction. For higher flow speeds, 0.85m/s to 0.95m/s, mode 4 is predicted to be the excited mode. When the flow speed reaches its maximum(0.98m/s) the predicted excited mode is mode 5.

Selected results from the analyses in VIVANA are compared to results from the ExxonMobil model test in Figure 12, Figure 13, and Figure 14.

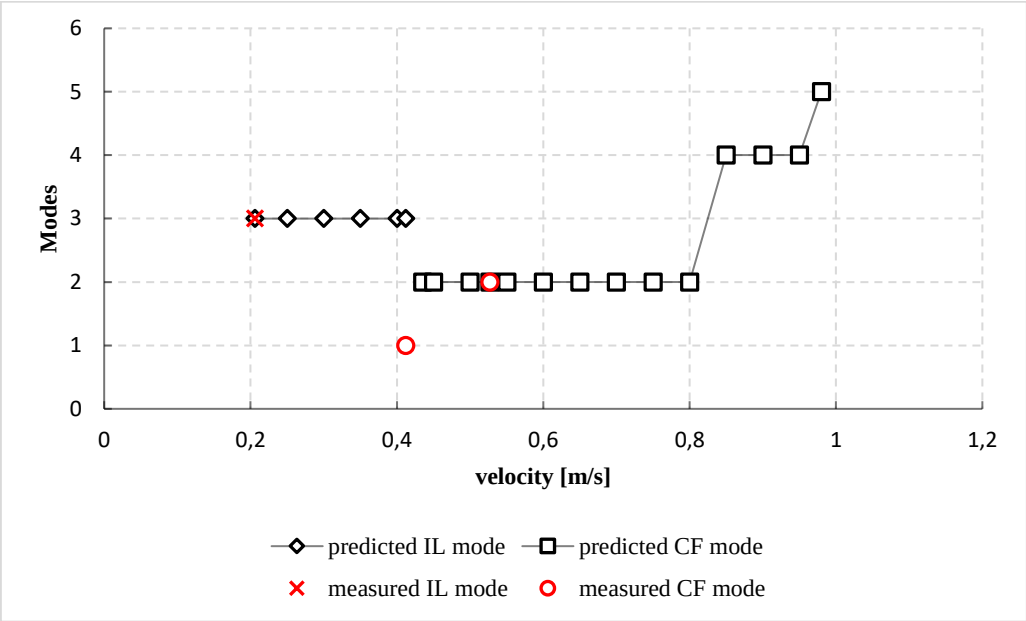

Figure 12. Comparison of the dominating modes predicted by VIVANA and the measured dominating modes for the 10° current direction. The measurement data is recreated from Wang et al. (2013).

Figure 12 shows that VIVANA gives correct mode prediction for current velocities 0.206m/s and 0.527m/s. For current velocity 0.412m/s, VIVANA predicts that mode 3 (due to IL loading in x direction) is the dominating mode when the measured dominating mode is mode 1 (due to CF loading in y direction). In other words, VIVANA predicts that there will be no VIV due to CF loading at such low current velocities. This is most likely because the default force coefficient database in VIVANA has been used for these analyses. The database is mainly based on rigid cylinder test data. It has not been tuned for pipelines or jumpers vibrating at low modes.

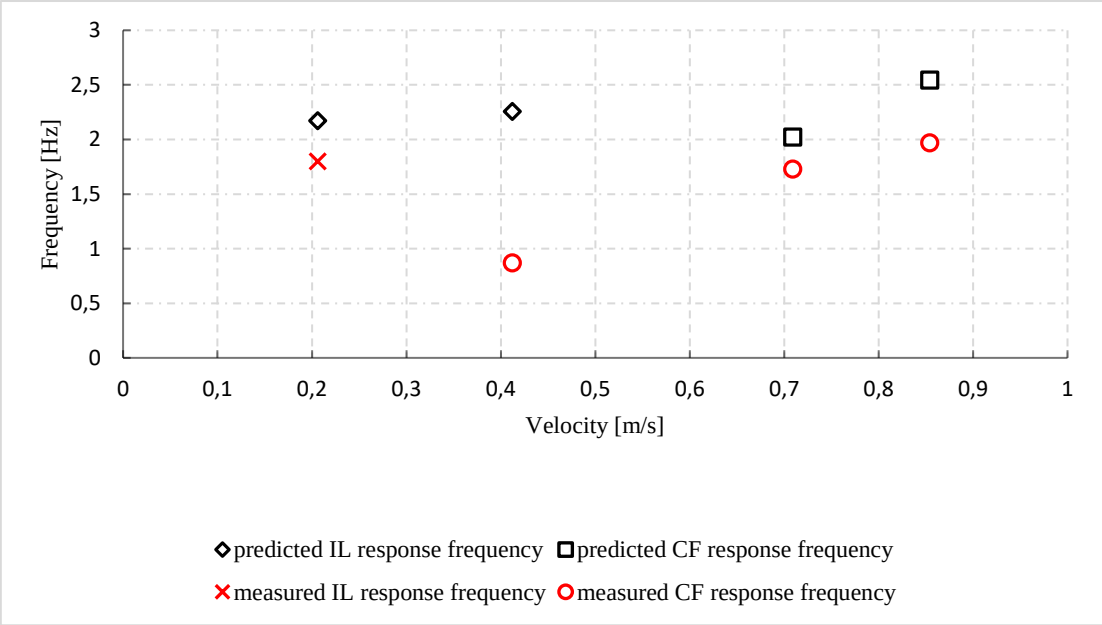

Figure 13. Comparison of the response frequencies predicted by VIVANA and the measured response frequencies for the 10° current direction. The measurement data is recreated from Zheng et al. (2015).

Figure 13 shows that VIVANA in general predicts larger response frequencies than what are measured. A refined added mass model can be constructed based on the measurement data, however, it is not considered in present study. Figure 9 shows that for high current velocities (velocities >0.53m/s), mode 2 is the dominating mode. Nevertheless, for velocities larger than 0.85m/s VIVANA predicts that mode 4 will be the dominating mode. This wrong prediction is most likely because the predicted response frequencies are larger than the measured response frequencies. E.g. for current velocity 0.854m/s the measured response frequency is closest to the predicted eigenfrequency of mode 2, whereas the predicted response frequency is closest to the predicted eigenfrequency of mode 4. For current velocity 0.412m/s the response frequency is largely over-predicted because VIVANA predicts CF VIV when in reality only IL VIV is measured for this current velocity.

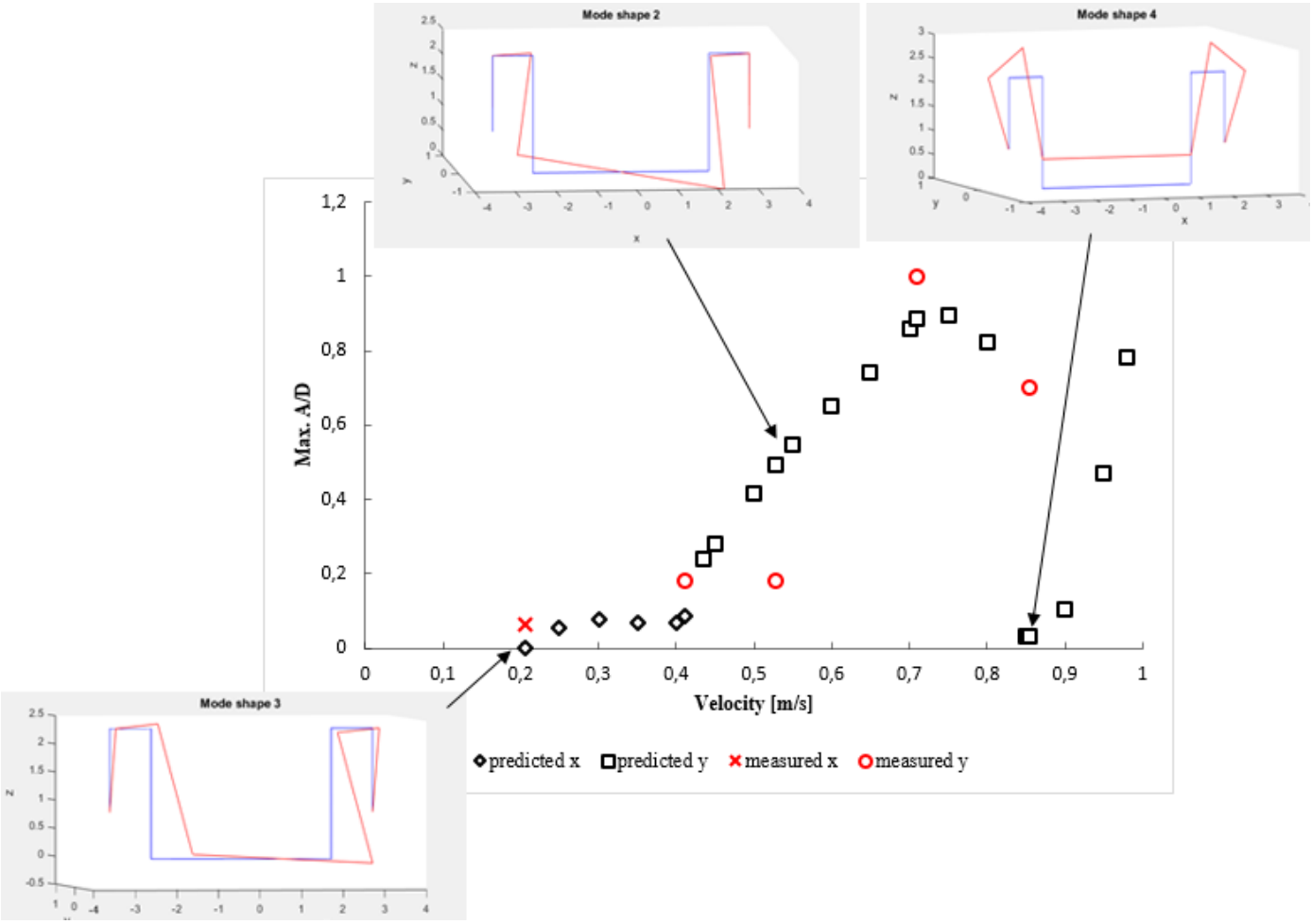

Figure 14. Comparison of the maximum non-dimensional response amplitude over the jumper model predicted by VIVANA and the measured values for the 10° current direction. The measurement data is recreated from Wang et al. (2013) and Zheng et al. (2015).

Figure 14 shows that VIVANA generally gives quite good predictions compared to the measured values for most current velocities, except for current velocity 0.854m/s. At this current, the predicted value is much smaller than the measured. The drop of the predicted maximum non-dimensional amplitude is probably due to the dominating mode shift, from mode 2 to mode 4, as can be seen in Figure 12.

In Figure 15 and 16, the predicted response at accelerometers 3 and 5 are plotted against current velocity ($U = V_r f_n D$) along with the measured response at accelerometers 3 and 5.

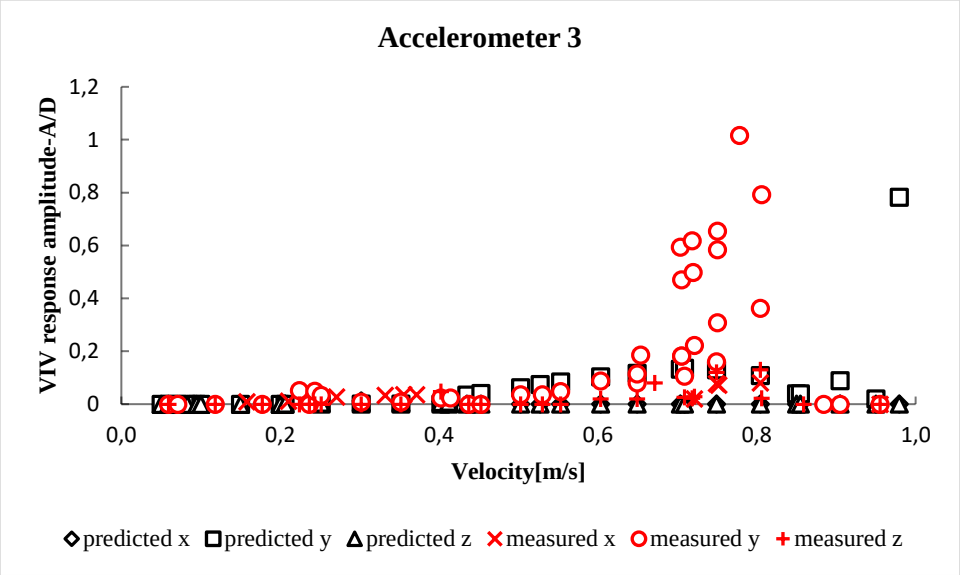

Figure 15. Comparison of the response predicted by VIVANA and the measured response at accelerometer 3 for the 10° current direction. The measurement data is recreated from Wang et al. (2013).

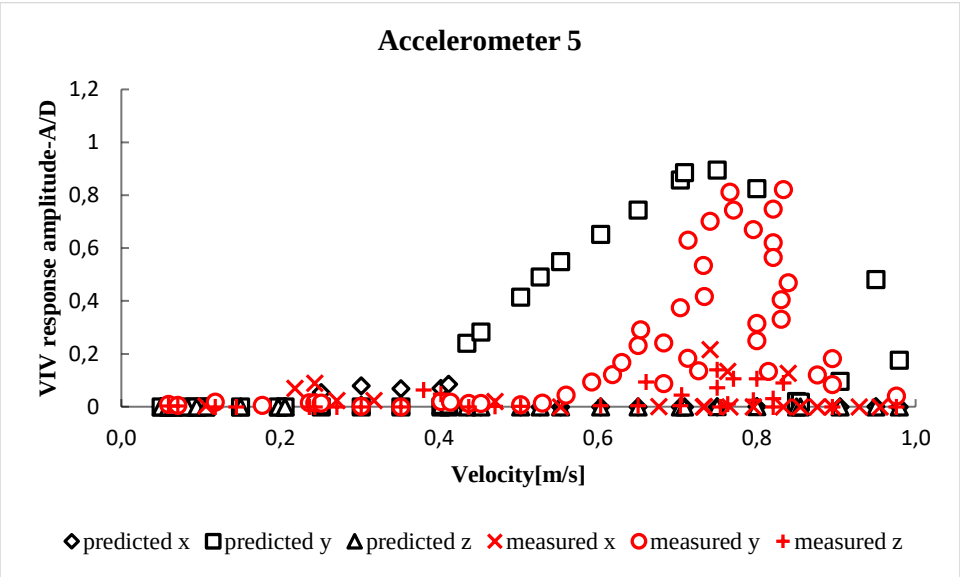

Figure 16. Comparison of the response predicted by VIVANA and the measured response at accelerometer 5 for the 10° current direction. The measurement data is recreated from Wang et al. (2013).

Figure 15 and 16 show that VIVANA predicts a much lower response due to CF loading for velocity 0.65m/s to 0.8m/s at accelerometer 3 then what is measured. Accelerometer 3 is located above the bend between a horizontal (H1) and vertical structural (V2) members. However, a simplified structural model with sharp corners are used in present study. This may cause the discrepancy between predicted and measured responses. However, there is a peak in the predicted values at velocity 0.98m/s This peak is because the dominating mode has shifted from mode 4 to mode 5 at this velocity. The response due to IL loads at accelerometer 3 is well predicted compared to the measured values.

At accelerometer 5 the predicted values in y-direction show a good trend compared to the measured values. However, the response in x and z-direction due to CF loading is predicted to be zero whereas the measured values show some response in x and z-direction due to CF loading. VIVANA does not predict multi-mode response for velocities<0.85m/s, and thus it predicts no response in x and z-direction. Nevertheless, for current velocities 0.85m/s to 0.95m/s VIVANA predicts response in y-direction even though mode 4 is the dominating mode (mode 4 gives deformations in x and z-directions and not in y, see figure 5). This can indicate that VIVANA predicts a multi-mode response for these velocities.

5.1.3. Prediction of 90° current direction

When the current hits the jumper plane at a 90° angle, both horizontal and vertical structural members will experience significant VIV as they all experience significant current normal to their cylindrical axes. Thus, the jumper experiences a uniform flow. The IL and CF responses occur in y and x directions respectively in this case.

Very little benchmark data can be found in the literature for this current direction.

The only benchmark data given for this current direction is the response at accelerometer 3 and accelerometer 7. In Figure 19 and 20, the predicted response at accelerometers 3 and 7 are plotted against current velocity along with the measured response at accelerometers 3 and 7. In these plots, the current velocity is calculated from the reduced velocity values in Wang et al. (2013) The response mode and the maximum displacement amplitude ratio for different tow speeds are presented in Figure 17 and 18 respectively. The comparison with the measurement is not made due to lack of data.

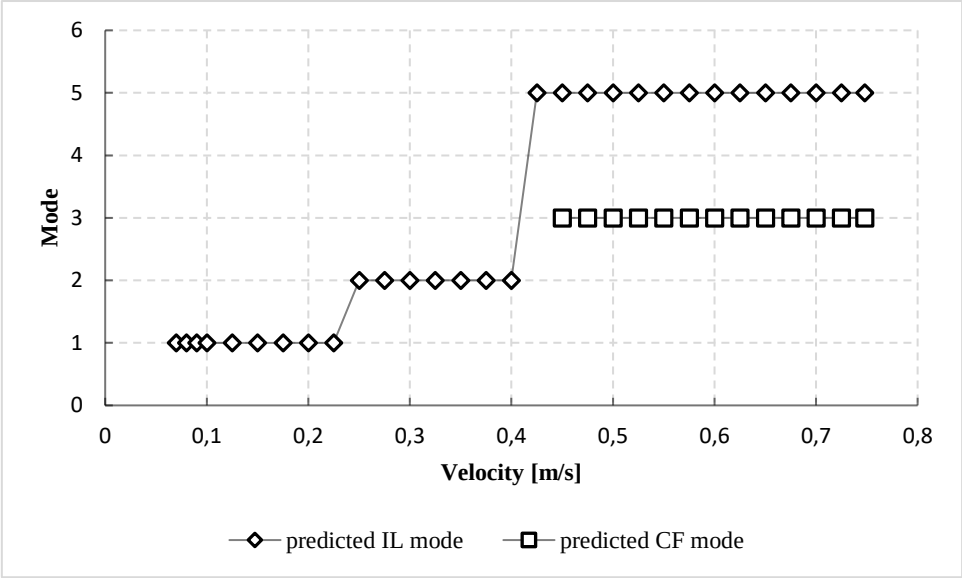

Figure 17. The dominating modes predicted by VIVANA for the 90° current direction.

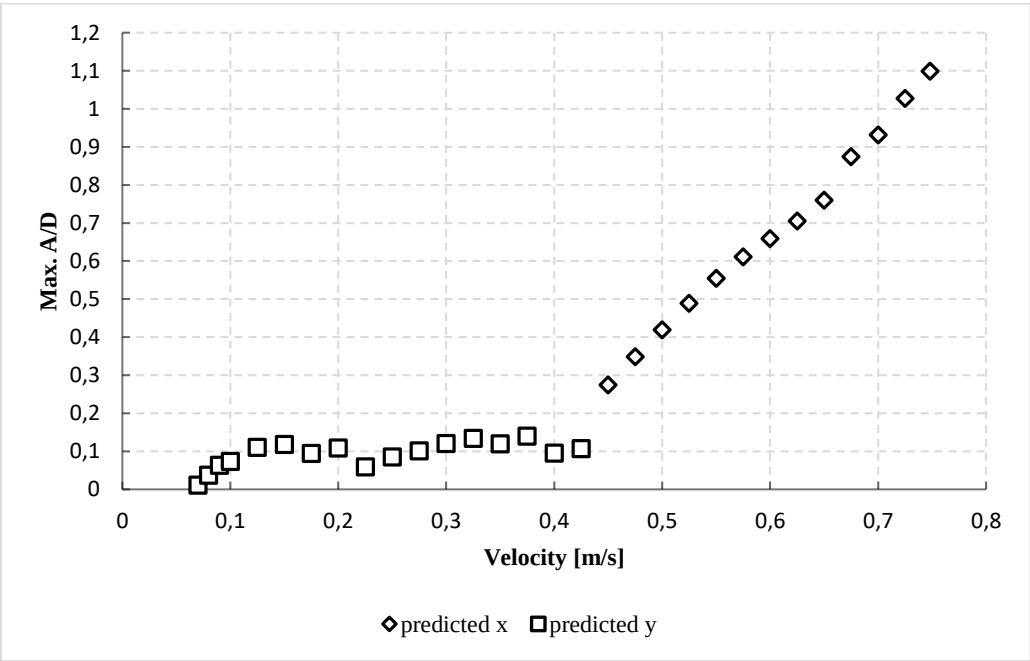

Figure 18. The maximum non-dimensional response amplitude over the jumper model predicted by VIVANA for the 90° current direction.

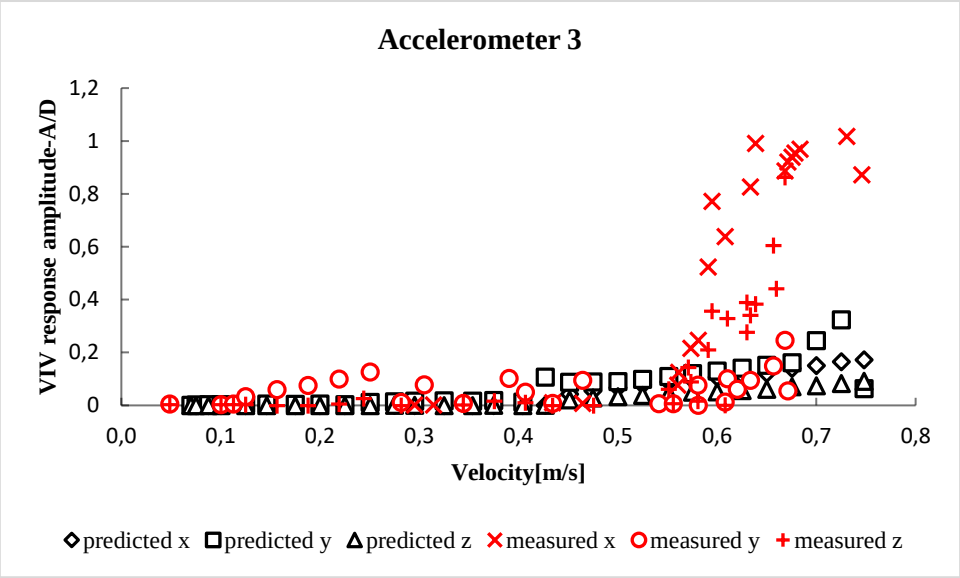

Figure 19. Comparison of the response predicted by VIVANA and the measured response at accelerometer 3 for the 90° current direction. The measurement data is recreated from Wang et al. (2013).

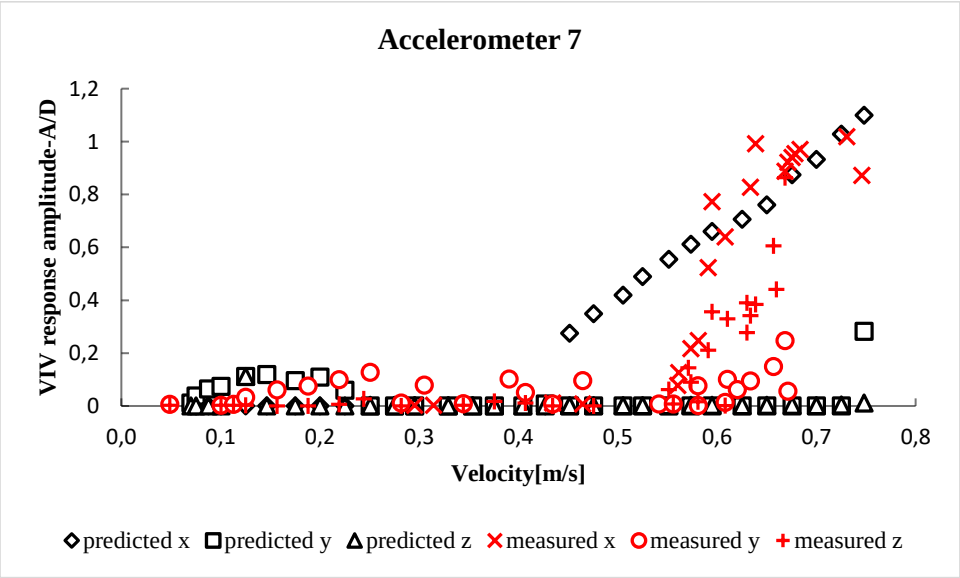

Figure 20. Comparison of the response predicted by VIVANA and the measured response at accelerometer 7 for the 90° current direction. The measurement data is recreated from Wang et al. (2013).

Figure 19 and 20 show that VIVANA predicts too low response in x and z-directions due to CF loading for velocities larger than 0.57m/s at accelerometer 3. Also, the predicted response in y-direction due to IL loading is somewhat smaller than measured at this accelerometer. At accelerometer 7 predicted values show a good trend compared to the measured values in x-direction. The response in y-direction is well predicted for current velocities smaller than 0.25m/s. However, for velocity 0.25m/s to 0.67m/s VIVANA predicts a somewhat lower response than what is measured. The response in z-direction due to CF loading is highly under-predicted by VIVANA. VIVANA predicts that the response in z-direction due to CF loading is zero while the measured values show significant response in z-direction due to CF loading.

VIVANA predicts that mode 3 will be the excited CF mode for current velocities larger than 0.45m/s. Looking at mode shape 3 (in Figure 7) there will be no motion in z-direction at accelerometer 7. If mode 4 was to be the dominating mode, there would be large motion in z-direction but no motion in x-direction at accelerometer 7. However, Figure 20 clearly shows that there is significant response in both x and z-direction at this position. This indicates that there is a multi-mode response where mode 3 most likely is the dominating mode with contributions from mode 4. VIVANA, on the other hand predicts a single mode response for these current velocities. This is probably why VIVANA predicts no response in z-direction at accelerometer 7.

5.2. Comparison with the response model approach

A separate IL, CF, and a CF induced IL analysis has been conducted using the response models in DNV-RP-F105(2006) for varying flow speeds with 10° and 90° directions relative to the jumper plane. To find the maximum amplitude response using the response models the eigenfrequencies and mode shapes needs to be known. Since the eigenvalue analysis done by VIVANA gave good results compared to the literature, the eigenfrequencies and mode shapes from this analysis will also be used in this approach.

As the maximum response over the jumper model due to CF loading always will be larger than the maximum response over the jumper model due to CF induced IL loading, the maximum response due to CF induced IL loading is not presented in this study.

5.2.1. Prediction of 10° current direction

When the current hits the jumper plane at a 10° angle, it is considered that IL and CF directions are in x-direction and y-direction. The response model is based on test data in uniform flow. However, this is not the case for jumper in this flow direction. 98% of the current velocity will hit the vertical members normal to their cylindrical axis, and thus may be able to excite VIV. While only 17% of the current velocity will hit the horizontal members normal to their cylindrical axis.

In Figure 21 and Figure 22, key results from the analyses based on the response model approach are benchmarked against the model test data.

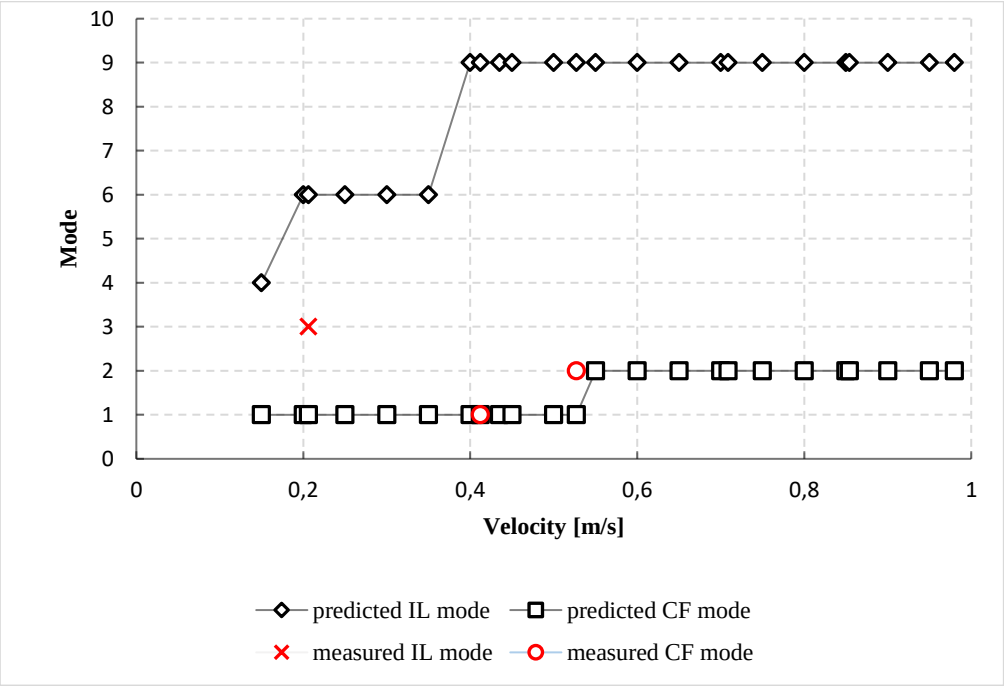

Figure 21. Comparison of the dominating modes predicted by DNV-RP-F105 and the measured dominating modes for the 10° current direction. The measurement data is recreated from Wang et al. (2013).

Figure 21 shows that the response model approach predicts that CF VIV can start at the same current velocity as IL VIV. This is because mode 1 is assumed to be the first CF mode and mode 3 the first IL mode. (using the natural frequency of mode 1(CF mode 1) to calculate Vr will give larger Vr value for lower velocities compared to using the natural frequency of mode 3(IL mode 1)) Therefore, when the calculated Vr,onset,IL =0.91 and Vr,onset,CF=2.5

according to the DNV-RP-F105(2006), CF or pure IL response may occur at the same current velocity for this case according to the above mentioned criteria.

To be conservative, the mode which leads to higher displacement in the response model is selected at flow speeds where two possible modes can be excited. Hence, mode 6 is chosen as the dominant mode over mode 3 at velocity 0.206m/s and mode 1 is chosen as the dominant mode over mode 2 at velocity 0.527m/s, as shown in Figure 21.

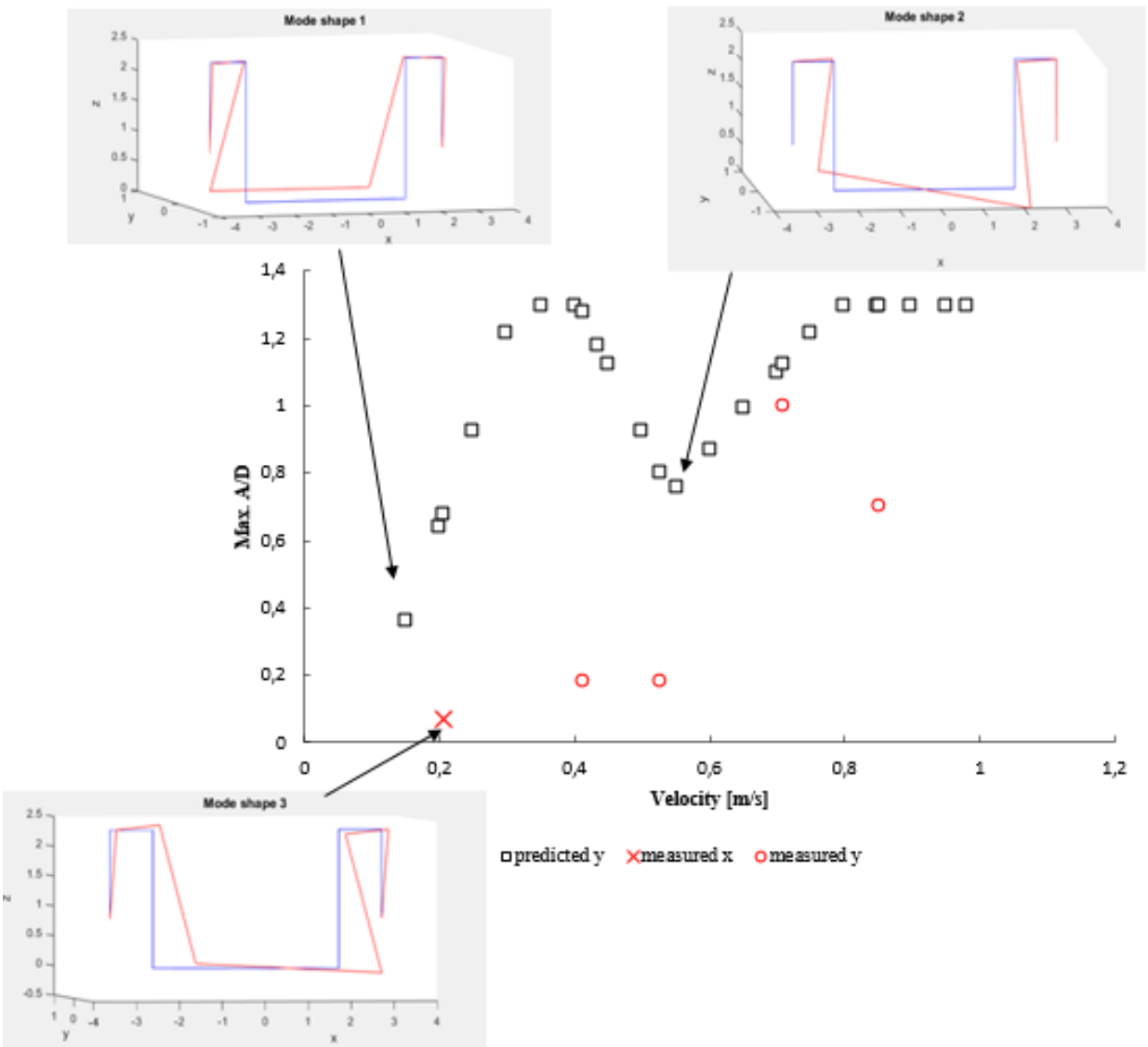

Figure 22. Comparison of the maximum non-dimensional response amplitude over the jumper model predicted by DNV-RP-F105 and the measured values for the 10° current direction. The measurement data is recreated from Wang et al. (2013).

Figure 22 shows that the response model approach generally over-predicts the maximum response for this current direction. At current velocity 0.206m/s, this over-prediction is most likely due to the prediction that CF VIV will occur at a such a low velocity. For the higher current velocities, the over-prediction probably is due to the uniform current assumption.

Figure 23 shows the maximum response over the jumper model if the correct response modes were predicted. The maximum response for current velocities smaller than or equal to 0.206m/s would be predicted accurately if the correct modes were predicted. However, for higher velocities the maximum response still would be over-predicted.

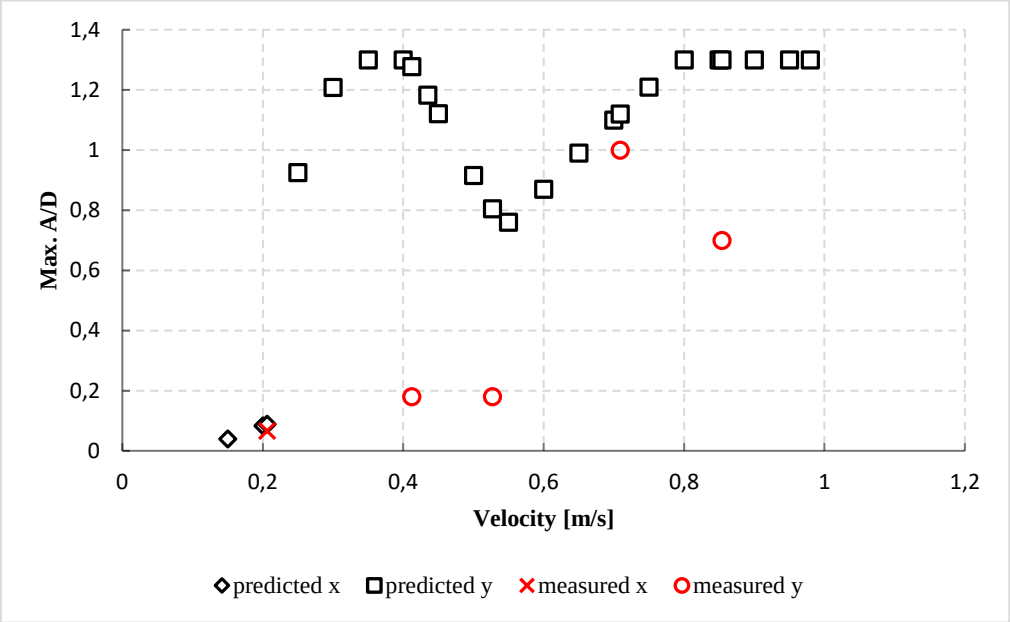

Figure 23. Comparison of the maximum non-dimensional response amplitude over the jumper model predicted by DNV-RP-F105, if the correct response modes were predicted, and the measured values for the 10° current direction. The measurement data is recreated from Wang et al. (2013).

5.2.2. Prediction of 90° current direction

When the current hits the jumper plane at a 90° angle, IL is in y-direction, CF is in x-direction for the vertical members and in z-direction for the horizontal members. Thus, modes with significant motions in x and z-directions can be viewed as CF modes, and modes with significant motion in y-direction can be viewed as IL modes.

Since little benchmark data can be found in the literature for this current direction, the predicted results shown in Figure 24 and 25 are not compared to measured values.

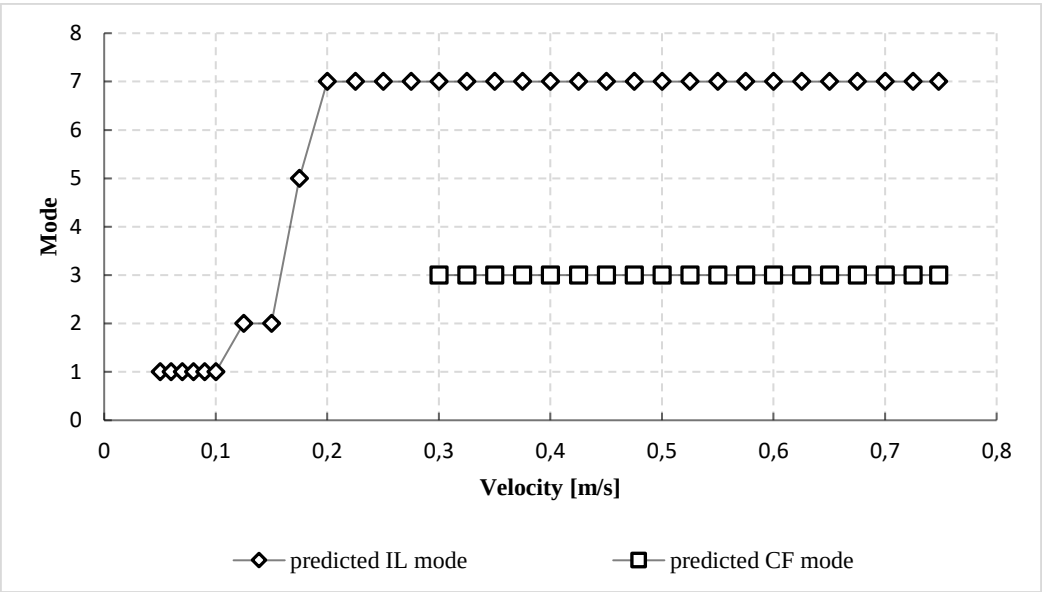

Figure 24. The dominating modes predicted by DNV-RP-F105 for the 90° current direction.

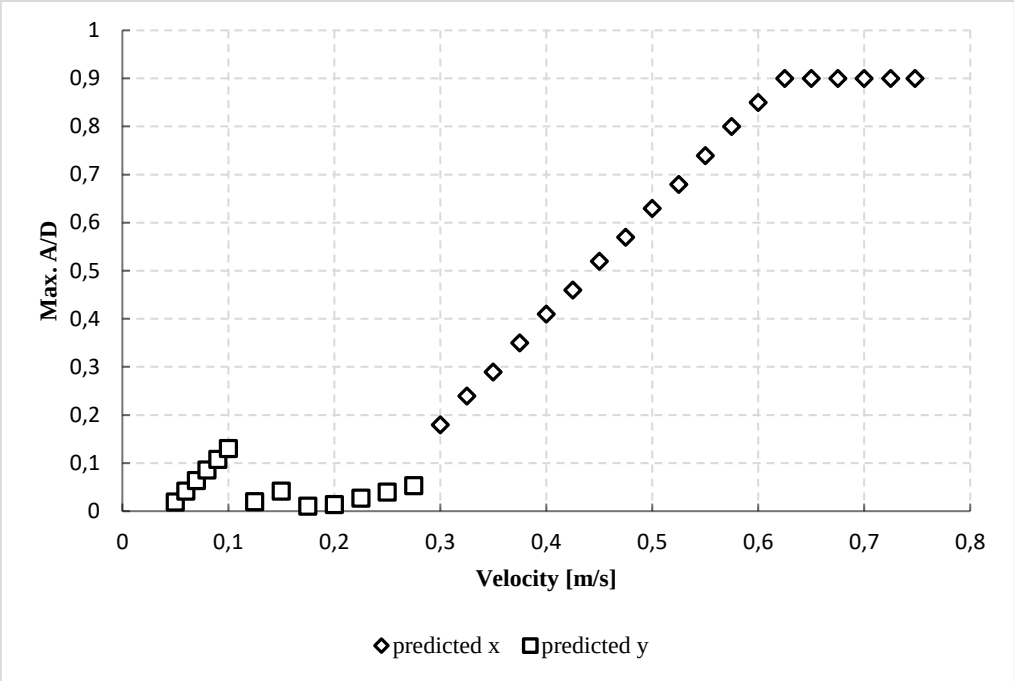

Figure 25. The maximum non-dimensional response amplitude over the jumper model predicted by DNV-RP-F105 for the 90° current direction.

5.3. Comparison of analysis using force model and the response model approaches

To compare VIVANA and the response models in DNV-RP-F105, the maximum non-dimensional response predicted by VIVANA is compared to the maximum non-dimensional response predicted by the response model approach. This is done for the 10° and 90° current direction in Figure 26 and 27, respectively.

Figure 26 shows that VIVANA clearly gives more accurate predictions compared to the response model approach. For current velocities smaller than 0.55m/s, the response model approach largely over-predicts the maximum response. This is probably because the response model approach predicts that CF VIV will occur at very low velocities. Furthermore, VIVANA defines the dominating mode using an excitation parameter based on energy considerations, whereas the response model approach uses a more simple and conservative method where the mode that gives the largest A/D is chosen as the dominant mode.

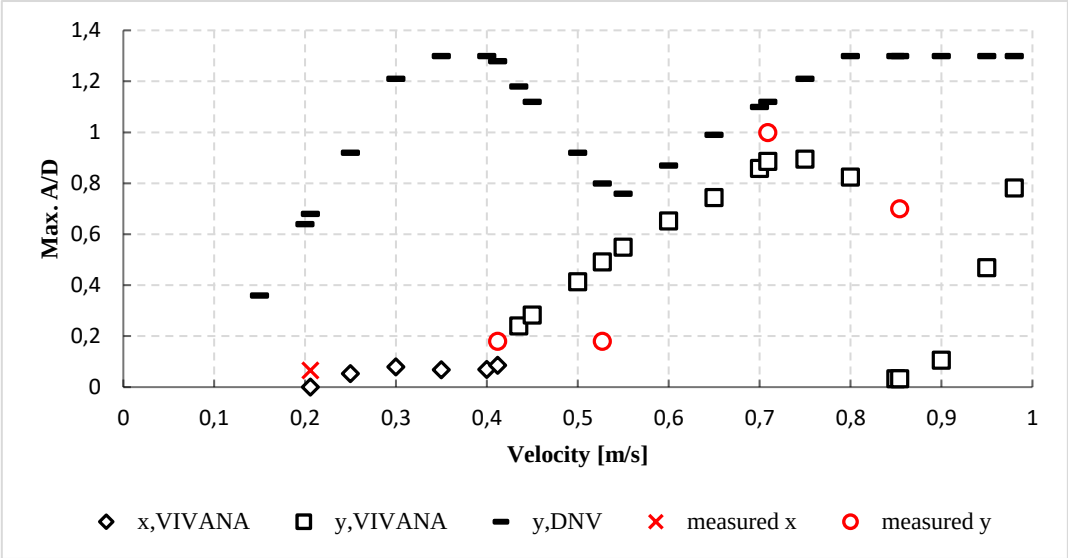

Figure 26. Comparison of the maximum non-dimensional response amplitude over the jumper model predicted by VIVANA and the DNV-RP-F105 for the 10° current direction.

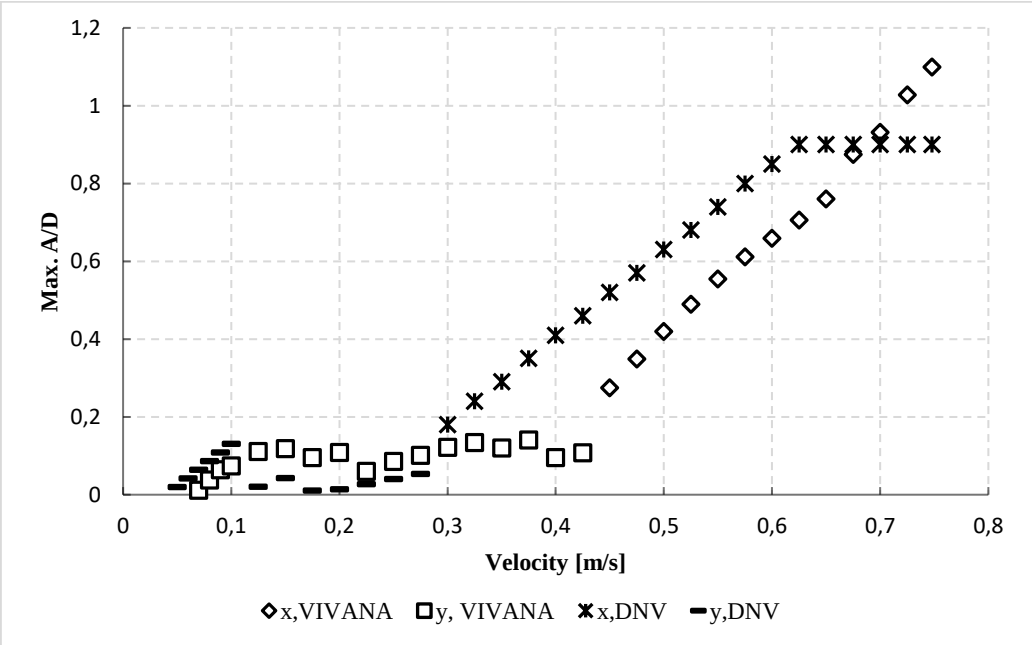

Figure 27. Comparison of the maximum non-dimensional response amplitude over the jumper model predicted by VIVANA and the DNV-RP-F105 for the 90° current direction.

Figure 27 shows that both methods predict similar response due to IL loading for velocities smaller than 0.1m/s. For velocities between 0.1m/s and 0.3m/s the response model approach predicts a somewhat smaller response than VIVANA. This is because the response model approach predicts higher IL response modes than VIVANA for these velocities. Nevertheless, since response model approach predicts that CF VIV starts after velocity 0.3m/s and VIVANA predicts that it starts at around 0.4m/s, the response model approach predicts a larger response for current velocities between 0.3m/s and 0.4m/s. For velocities larger than 0.4m/s, both methods predict quite similar results.

5.4. Summary of the comparisons

VIVANA gives quite good predictions of the maximum response over the jumper model for the 10° current direction. The response model approach on the other hand, largely over-predicts the maximum response for this current direction. However, for the 90° current direction both methods give quite similar predictions. This is probably because when the current hits the jumper plane at a 90° direction the jumper behaves similarly to a free spanning pipeline because the horizontal span, H2, dominates the response.

For both current directions VIVANA generally under-predicts the response at accelerometer 3, which is located at the bend between a horizontal and vertical structural member. This is probably because of the simplified structural model with sharp corners used in present study. For the 10° current direction the response predicted by VIVANA at accelerometer 5 in y-direction show a good trend compared to the measured values. However, the response in x and z-direction due to CF loading is predicted to be zero whereas the measured values show some response in x and z-direction due to CF loading. This is probably because VIVANA predicts a single mode response when in reality there is a multi-mode response.

For the 90° current direction the response predicted by VIVANA at accelerometer 7 in x and y-direction show a good trend compared to the measured values. However, the response in z-direction due to CF loading is predicted to be zero whereas the measured values show significant response in z-direction due to CF loading. This is probably because of the same reason as mentioned above, single mode response is predicted.

6. Conclusion

Two prediction methods, the force model approach (VIVANA) and the response model approach based on DNV-RP-F105(2006), have been evaluated by benchmarking against the model test data. The main conclusions are as follows:

- For the 10° current direction, the flow speed normal to the structure varies due to the orientation of the structural members. VIVANA generally gives good predictions when it comes to the maximum response over the jumper model. On the other hand, the response model approach based on DNV-RP-F105(2006) largely over-predicts the maximum response.

- For the 90° current direction, the flow speed normal to the structure is uniform. VIVANA and the response models predicts quite similar maximum response for this current direction. The response in x-direction is better predicted compared to the model test results than the prediction in z-direction.

- This study shows that the force model approach is in general applicable for VIV response prediction of a planar rigid jumper. The use of the response model approach will lead to larger over-prediction when the flow angle is oblique to the jumper plane in this study. The force model can apply correct hydrodynamic loads to the structural members depending on the local flow speed, while the response model implicitly assumes loads corresponding to a uniform flow.

References

Blevins, R. D. (1990). *Flow Induced Vibrations* (2nd ed.). New York, USA: Van Nostrand Reinhold

Deka, D., Cerkovnik, M., Panicker, N., & Achanta, V. (2013). *Subsea Jumpers Vibration Assessment.* Paper presented at the 32nd International Conference on Ocean, Offshore and Arctic Engineering (OMAE2013-11011), Nantes, France.

DNV-RP-F105 *Free spanning pipelines* (2006). DNV, Norway.

Gopalkrishnan, R. (1993). *Vortex-Induced Forces on Oscillating Bluff Cylinders.* (Ph.D.), Massachusetts Institute of Technology, Cambridge, MA, USA.

Hariharan, M., Cerkovnik, M. E., & Thompson, H. M. (2004). The Significance of Low Velocity Near Bottom Currents on the In-Line Vortex-Induced Vibration Response of Rigid Subsea Jumpers

Holmes, S., & Constantinides, Y. (2010). *Vortex Induced Vibration Analysis of a Complex Subsea Jumper*. Paper presented at the 29th International Conference on Ocean, Offshore and Arctic Engineering (OMAE2010-20520), Shanghai, China.

Larsen, C. M. (2011). *VIV A short and incomplete introduction to fundamental concepts*. Trondheim, Norway: Department of marine technology, Norwegian University of Science and Technology.

MIT. (2016). SHEAR7[Computer software].

MIT. (2016). *Shear 7 User Guide for SHEAR7 Version 4.9b*: AMOG consulting.

Nielsen, F.G., Kvarme, S.O. and Søreide, T.(2002) *VIV response of long free spanning pipelines*. Paper presented at the 21st International conference on offshore mechanics and arctic engineering, (OMAE2002-28075), Oslo, Norway.

Passano, Elizabeth, Carl M. Larsen, and Jie Wu.(2010) *VIV of free spanning pipelines: Comparison of response from semi-empirical code to model tests.* Paper presented at the ASME 2010 29th International Conference on Ocean, Offshore and Arctic Engineering(OMAE2010-20330), Shanghai, China.

Passano, E., Larsen, C. M., Lie, H., & Wu, J. (2016). *VIVANA Theory Manual V4.8.0*. Trondheim: MARINTEK.

Sintef Ocean. (2016). VIVANA (Version 4.8) [Computer software]

Sumer, B. M., & Fredsøe, J. (1997). *Hydrodynamics around cylindrical structures* (Vol. 12). London: World Scientific.

Voie, P., Wu, J., Resvanis, T., Larsen, C.M., Vandiver, J.K., Triantafyllou, M. & Baarholm, R. (2017). *Consolidation of Empirics for Calculation of VIV Response.* Paper presented at the ASME 2017, 36th International Conference on Ocean, Offshore and Arctic Engineering.

Wang, H., Huang, J., Lee, S., Gioielli, P., Kan, W., Spencer, D., & Islam, M. (2013). *VIV Response of a Subsea Jumper in Uniform Current.* Paper presented at the ASME 2013 32nd International Conference on Ocean, Offshore and Arctic Engineering(OMAE2013-11417), Nantes, France.

Zheng, H., Slocum, S. T., Huang, J. Z., Srivastava, V., Lee, S., & Wang, H. H. (2015). *Numerical Analysis of Experimental Data of Subsea Jumper Vortex Induced Vibrations.* Paper

presented at the ASME 2015 34th International Conference on Ocean, Offshore and Arctic Engineering(OMAE2015-41224), Newfoundland, Canada.

Chapter 5: Fatigue Damage Assessment

In this chapter, results obtained from chapter 4 are to be used to calculate the fatigue damage of the rigid jumper model. Both the DNV-RP-F105 and VIVANA have methods to calculate the stress due to VIV, as well as the fatigue damage. However, the shear stress due to torsional moment is normally ignored.

A study by Nair et al. (2013) shows that rigid jumpers, planar or multi-planar, can experience significant torsional stress contributions. Consequently, the method in VIVANA and the method in DNV-RP-F105 cannot accurately be used to estimate the fatigue damage for the rigid jumper considered.

Two different fatigue damage calculation methods, where the torsional shear stresses are considered, will be used to calculate the fatigue damage of the rigid jumper. The first method is a method proposed by Nair et al. (2011) and the second method is a novel method proposed in this thesis by using the first principal stress.

5.1. Fatigue Damage Calculation Methodology

5.1.1. Method 1: a method presented by Nair et al. (2011)

In the method proposed by Nair et al. (2011), one possible approach to include the torsional stress in fatigue assessment is to consider torsional stress to be equivalent to flexural stress. Thus, the torsional stress ranges due to CF loading can be found by multiplying the flexural stress ranges with a torsion ratio($t(x)$) given by:

$$t(x) = \frac{A_{torsion,i}(x)}{A_{flexural,i}(x)} \tag{5.1}$$

Where $A_{torsion,i}(x)$ is the torsional unit stress of mode *i* at location *x*, and $A_{flexural,i}(x)$ is the flexural unit stress of mode *i* at location *x*.

The flexural stress range is found using the stress assessment method given in DNV-RP-F105 (2006).

5.1.2. Method 2: a novel method using first principal stress

According to DNV-RP-C203 (2010) it is conservative to use the principal stress range in the fatigue analysis when the direction of the nominal stress and the principal stress is different (angle between the nominal stress direction and the principal stress direction, φ, is not zero). This is the case when there are both normal stresses (σ) and shear stresses (τ), see Figure 5.1.

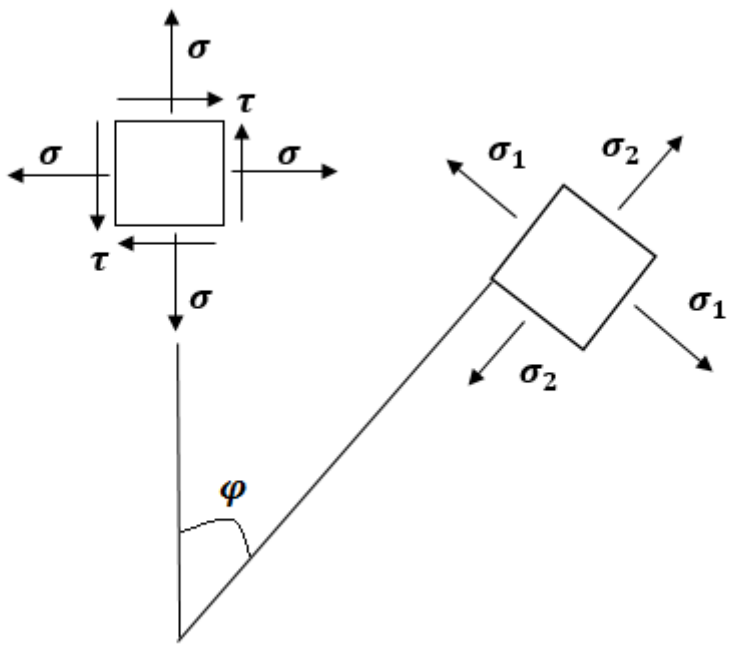

Figure 5.1. Stress state of a small solid element.

Thus, it is conservative to use the first principal stress(σ_1), which is the maximum principal stress, to combine the bending stress and the torsional shear stresses.

$$\sigma_1 = \frac{\sigma_{bending}}{2} + \sqrt{(\frac{\sigma_{bending}}{2})^2 + \tau_{shear}{}^2} \tag{5.2}$$

Where $\sigma_{bending}$ is the bending stress and τ_{shear} is the shear stress due to torsion.

The hoop stress (σ_{hoop}) is not included in present study since the experiment carried out is without internal pressure. On general base, the principle stress calculation should be:

$$\sigma_1 = \frac{\sigma_{bending} + \sigma_{hoop}}{2} + \sqrt{(\frac{\sigma_{bending} - \sigma_{hoop}}{2})^2 + \tau_{shear}{}^2} \tag{5.3}$$

In this method, the flexural and torsional stress ranges are calculated in the same way as in method 1.

5.2. Modal Analysis

The modal analysis performed in VIVANA, which results are used in chapter 4, could not be used in this chapter because it does not provide the unit stress amplitudes due to torsion. This is because the beam formulation in VIVANA does not consider torsional stiffness. (Passano, 2016) Hence, another modal analysis has been performed, using the FEA software ANSYS (ANSYS, 2015), to obtain the unit amplitude stresses due to bending and torsion. The difference in the FEM in VIVANA and the FEM in ANSYS is that the model in ANSYS have bends at the corners and torsional stiffness is considered in the beam formulation. Pipe288 elements are used in the ANSYS model, which is based on Timoshenko beam theory, a first-order shear-deformation theory (ANSYS, 2013). Transverse-shear strain is constant through the cross-section; that is, cross-sections remain plane and undistorted after deformation, see Figure 5.2.

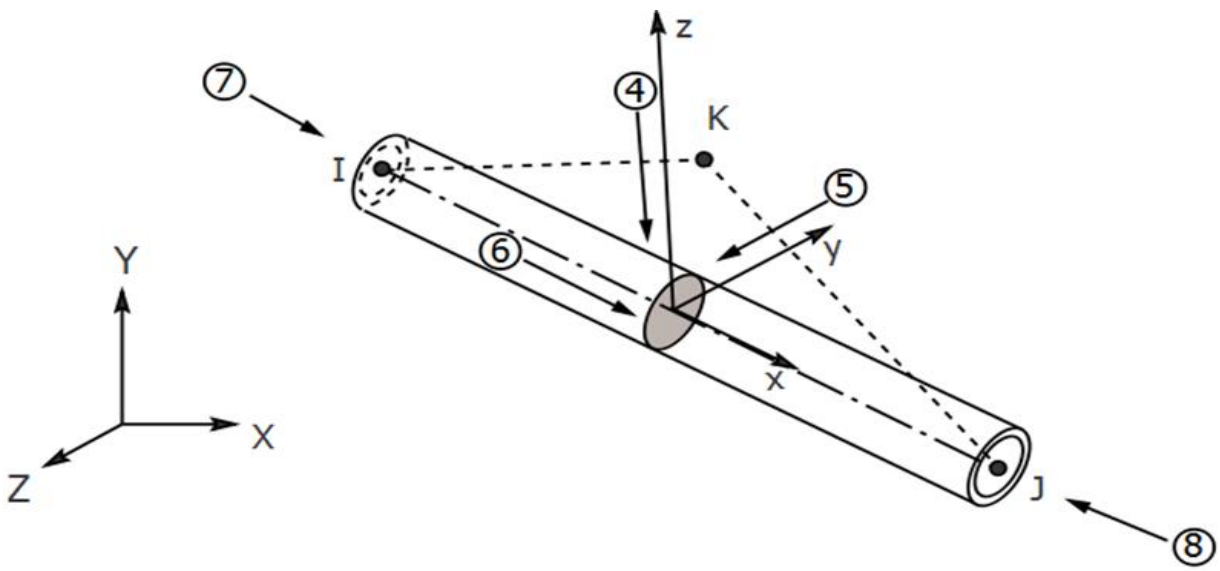

Figure 5.2. Pipe288 geometry (taken from ANSYS, 2013).

Table 5.1 show the predicted eigenfrequencies from the modal analysis in VIVANA and from the modal analysis in ANSYS. In Figure 5.3, 5.4, 5.5 and 5.6, the first four mode shapes predicted by VIVANA are plotted against the four first mode shapes predicted by ANSYS. The accelerometer positions are shown in Figure 5.13.

Table 5.1 shows that the eigenfrequencies estimated in ANSYS are somewhat larger than those estimated by VIVANA. However, the difference between the frequencies are smaller than 6%. Figure 5.3 to 5.6 show that the predicted mode shapes are basically the same. This is also the case for the higher modes, mode 5 to 9. The results show that the two modal analyses match each other well even though the beam formulation differs

Table 5.1. Predicted eigenfrequencies.			
Mode	eigenfreq. VIVANA [Hz]	eigenfreq. ANSYS [Hz]	difference in %
1	0.8587	0.85	-1.0
2	2.1403	2.23	4.2
3	2.1741	2.294	5.5
4	2.5457	2.637	3.6
5	3.2669	3.429	5.0
6	3.56	3.743	5.1
7	3.6218	3.817	5.4
8	6.1957	6.397	3.2
9	6.911	7.187	4.0

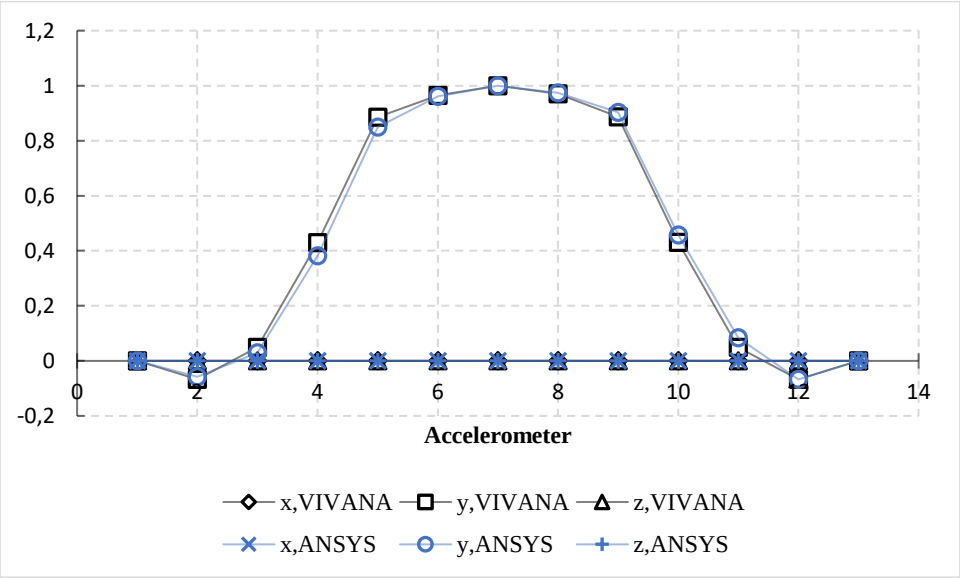

Figure 5.3. Comparison of mode shape 1 predicted by VIVANA (black lines) and mode shape 1 predicted by ANSYS (blue lines).

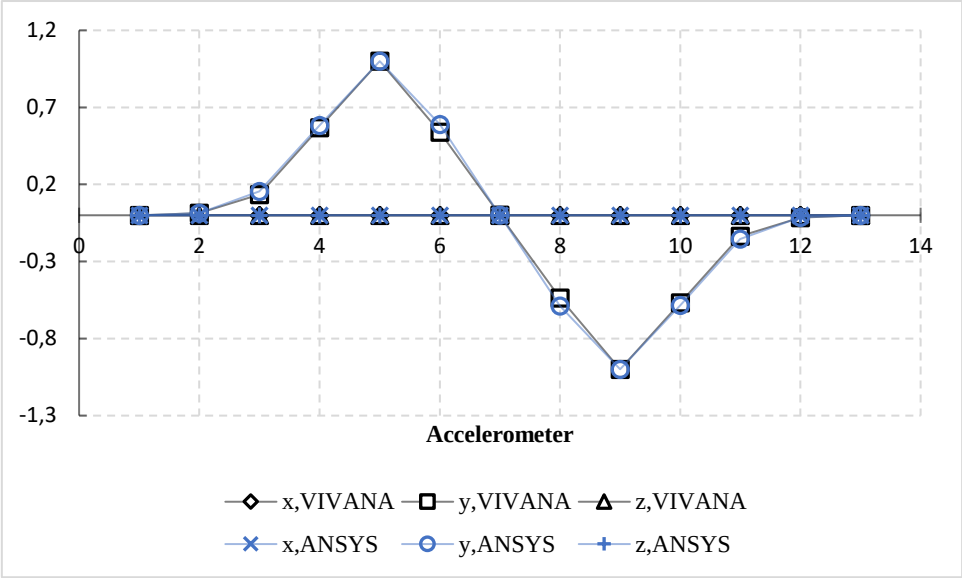

Figure 5.4. Comparison of mode shape 2 predicted by VIVANA (black lines) and mode shape 2 predicted by ANSYS (blue lines).

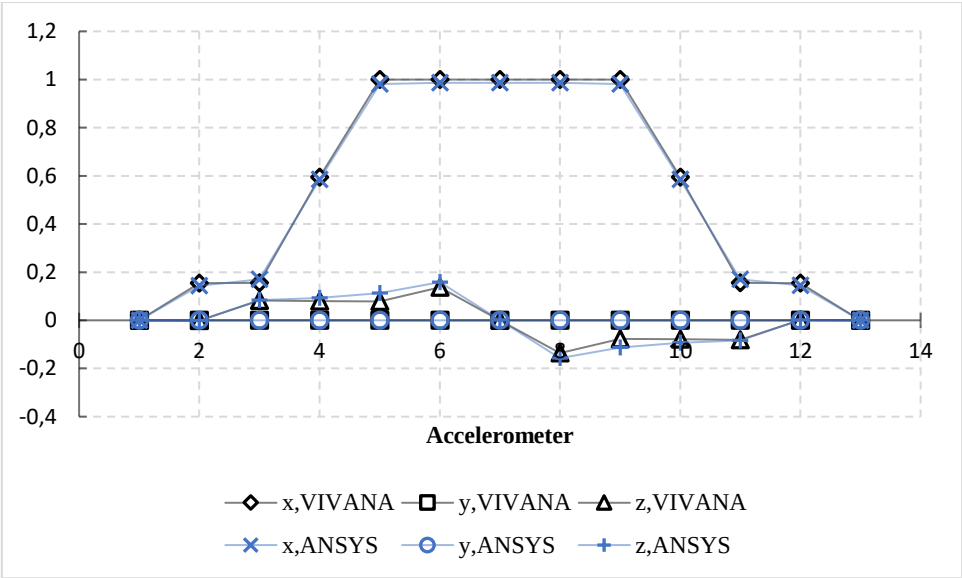

Figure 5.5. Comparison of mode shape 3 predicted by VIVANA (black lines) and mode shape 3 predicted by ANSYS (blue lines).

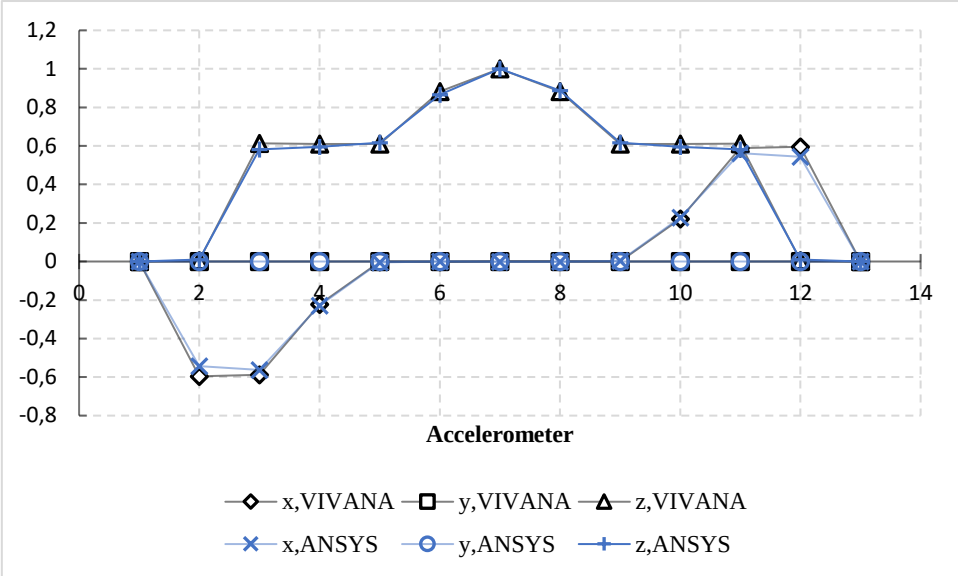

Figure 5.6. Comparison of mode shape 4 predicted by VIVANA (black lines) and mode shape 4 predicted by ANSYS (blue lines).

5.2.1. Modal unit amplitude stresses

The flexural modal stresses and the torsional modal stresses obtained from the modal analysis in ANSYS have been normalized by multiplying the stress of mode *i* at each location with:

$$\frac{D_{outer}}{D_{modal,max,i}} \tag{5.4}$$

Where D_{outer} is the pipe outer diameter, and $D_{modal,max,i}$ is the maximum modal displacement of mode *i*.

The normalized flexural and torsional unit stresses are plotted in Figure 5.7 and 5.8, respectively. Figure 5.8 shows that there are no torsional modal stresses associated with mode 3,4,6 and 9. This is because only modes that gives motion out of the jumper plane (y-direction) are associated with torsional stresses. Thus, in the present study when the current hits the jumper plane at a 10° direction there will be no torsional stresses due to IL loading. Moreover, when the current hits the jumper plane at a 90° direction there will be no torsional stresses due to CF loading.

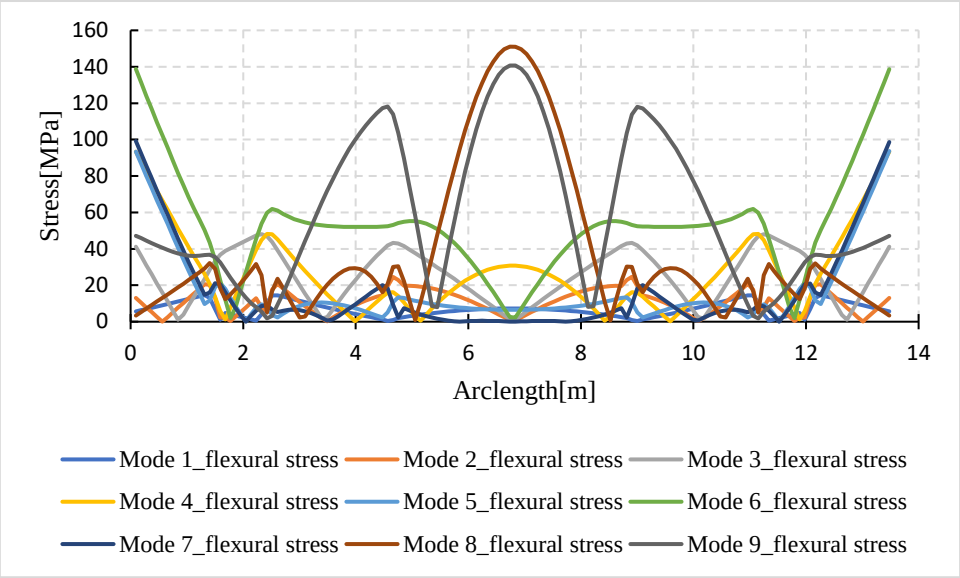

Figure 5.7. Flexural modal stresses versus arclength.

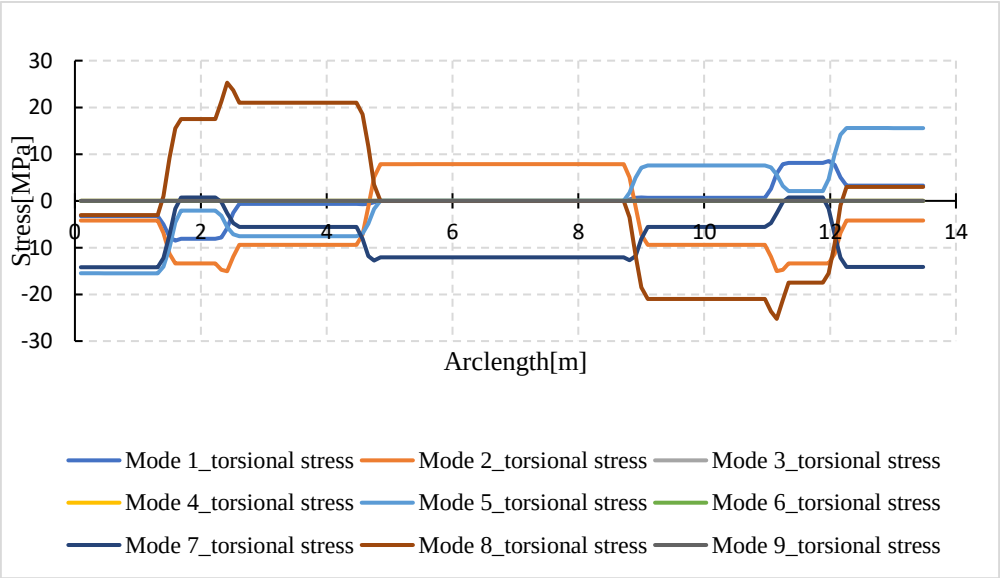

Figure 5.8. Torsional modal stresses versus arclength.

5.2.2. Modal stresses for the 10° flow direction

Figure 5.9 and 5.10 show the possibly active IL and CF modes along with their associated modal stresses for the 10° flow direction.

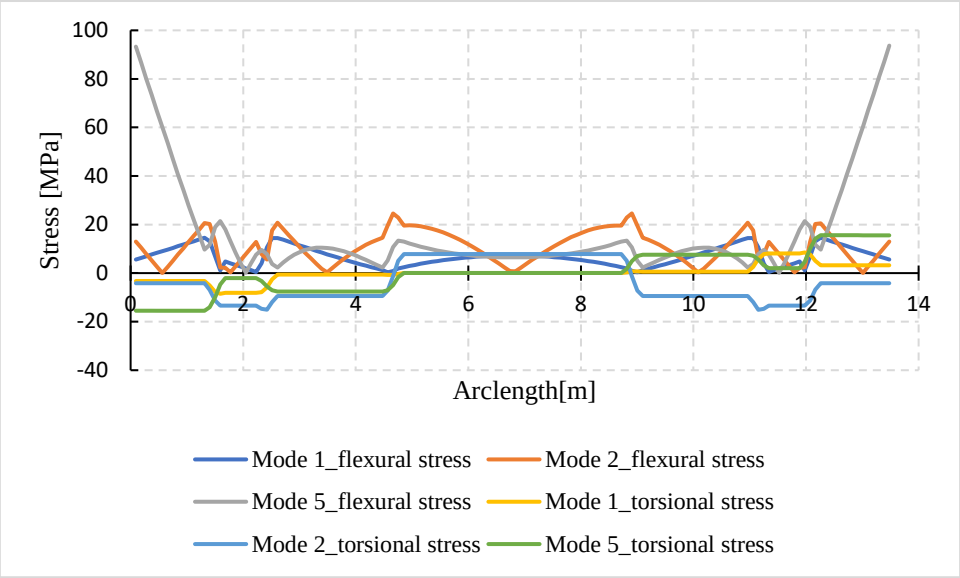

Figure 5.9. CF modal stresses versus arclength for the 10° flow direction.

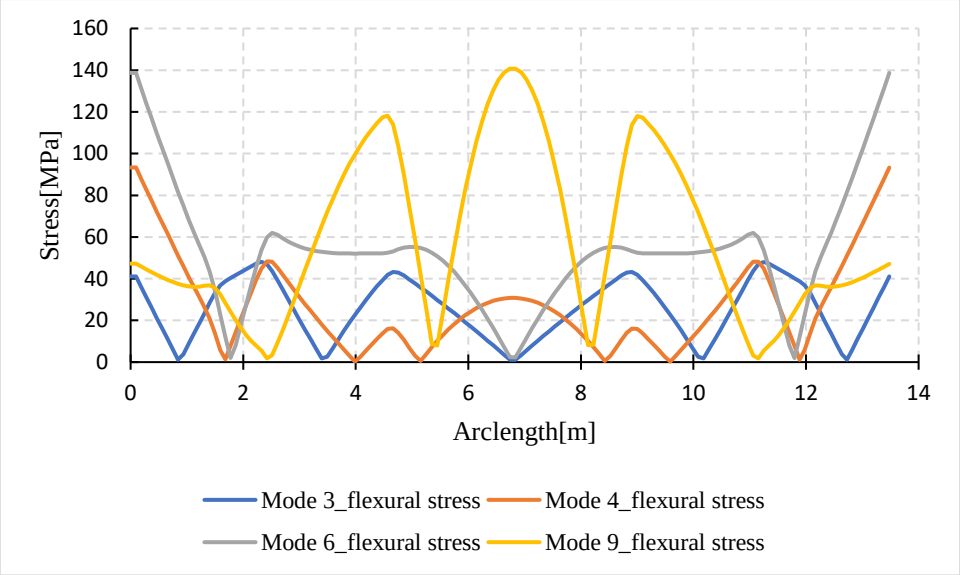

Figure 5.10. IL modal stresses versus arclength for the 10° flow direction.

Figure 5.9 and 5.10 show that the peak flexural stress due to IL loading will occur approximately at the middle of the jumper length (location A), and the peak torsional and flexural stress due to CF loading will occur at the right jumper end (location B). Thus, only the stress at these locations will be estimated for this current direction.

5.2.3. Modal stresses for the 90° flow direction

Figure 5.11 and 5.12 show the possibly active IL and CF modes along with their associated modal stresses for the 90° flow direction.

Figure 5.11 and 5.12 show that the peak flexural stress due to IL loading occurs at the left end of the jumper (location C) and the peak torsional stress at the right end of the jumper (location B). The peak flexural stress due to CF loading also occurs at the right end of the jumper. Only the stresses at these locations (B and C) will be estimated for this current direction. Figure 5.13 shows location A, B, and C (locations where the stresses are to be calculated) on the jumper model.

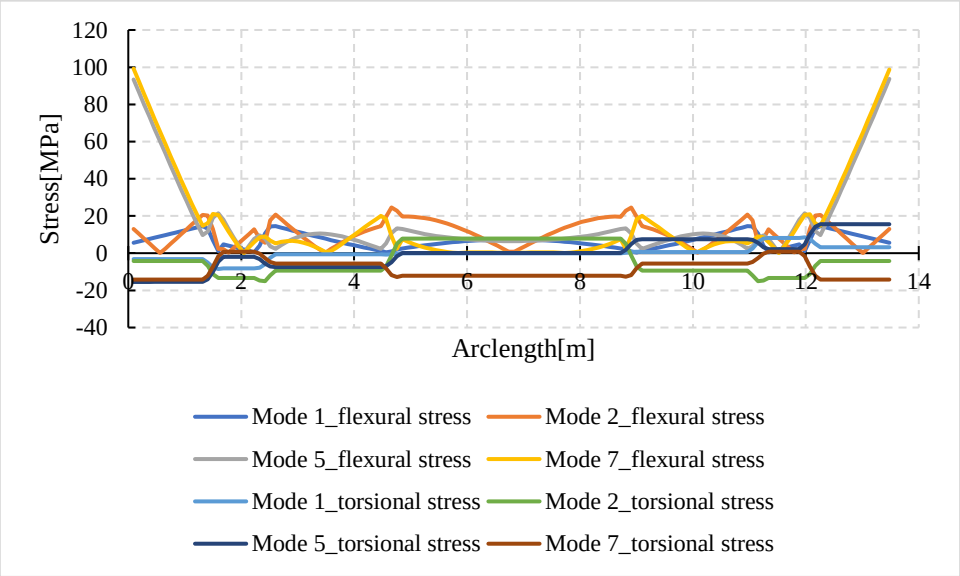

Figure 5.11. IL modal stresses versus arclength for the 90° flow direction.

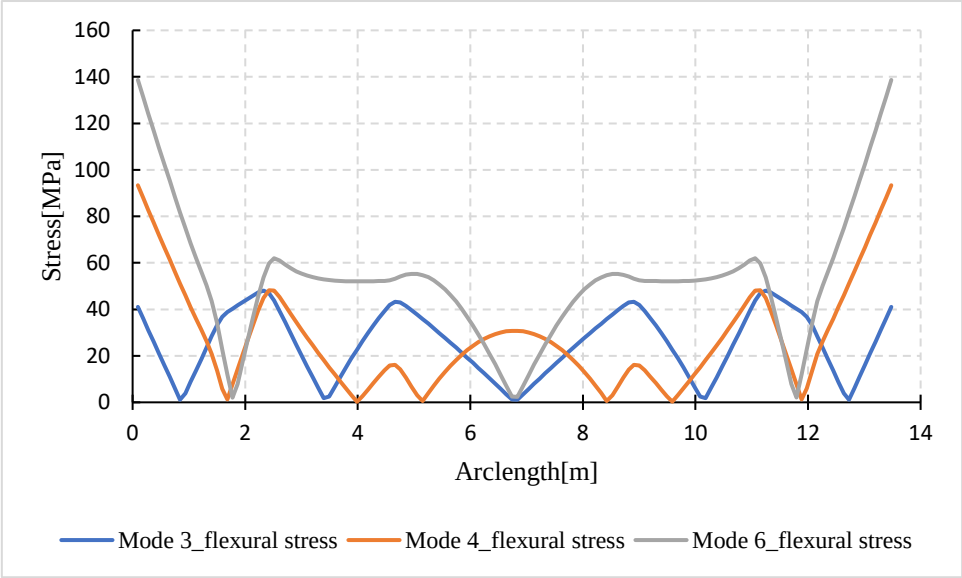

Figure 5.12. CF modal stresses versus arclength for the 90° flow direction.

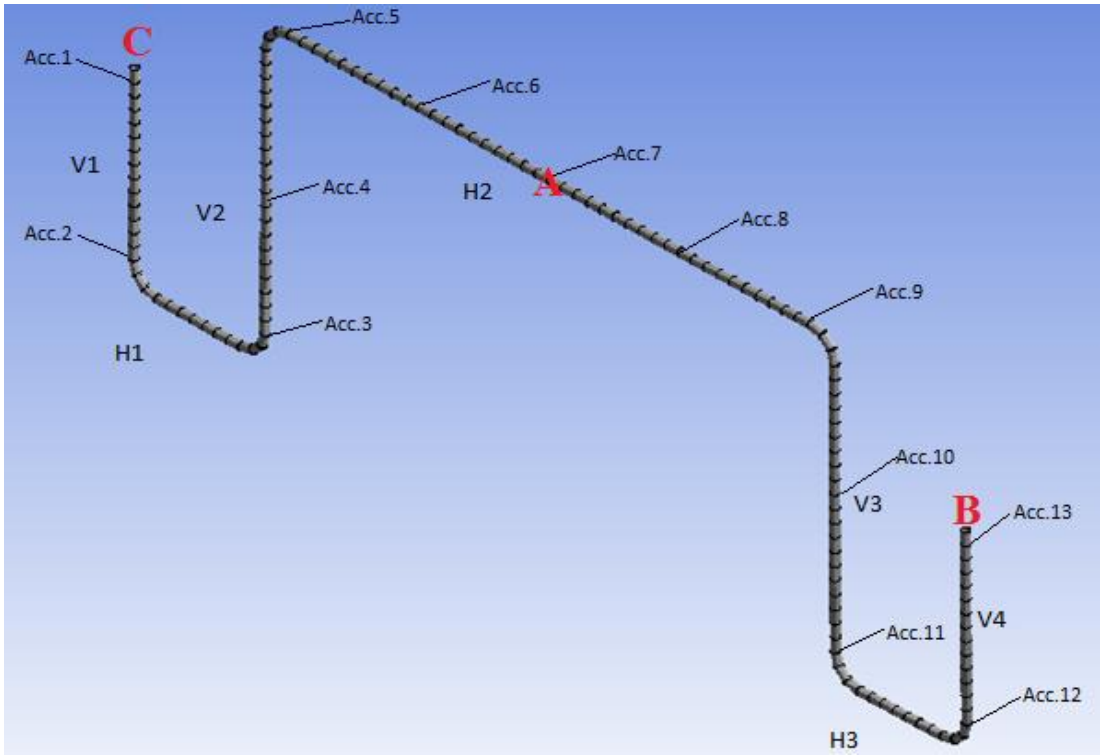

Figure 5.13. Location A, B, and C on the jumper model.

5.3. Results and Discussion

The fatigue damage of the rigid jumper is found using the stresses calculated in Appendix C. These stresses are calculated using the VIV response predicted by the response model approach (based on DNV-RP-F105) and the VIV response predicted by VIVANA.

The stresses, and hence the fatigue damage, due to the predicted response from the response model approach and the predicted response from VIVANA are calculated using the same stress assessment method.

The fatigue damage is calculated using two different methods. In method 1, the fatigue damage due to flexural stresses and the fatigue damage due torsional stresses are calculated separately. In method 2, the flexural and torsional stresses are combined into the first principal stress, which then is used to calculated the fatigue damage.

When calculating the fatigue damage, the probability of occurrence of each of the different current velocities considered is assumed to be 1. Furthermore, S-N curve B1, for structures in seawater free to corrode, given in DNV-RP-C203 (2010) have been chosen for the jumper system considered in this thesis. A problem with using this S-N curve on the jumper system considered in this chapter, is that S-N curve B1 is for steel structures and the jumper model is made of aluminium. However, the aluminium jumper model is a small-scale model of a 10" outer diameter "M" shaped rigid steel jumper. The small- scale aluminium jumper model and the steel jumper has similar geometry, mass ratio and torsion- and bending stiffness. Thus, the two jumpers are believed to experience the same VIV response and thus the same stresses. Hence, using this S-N curve and the stresses calculated from the model scale aluminium jumper is believed to give the fatigue damage of the full-scale steel jumper.

5.3.1. Fatigue damage results of method 1

In this section, the fatigue damage due to the VIV response predicted by VIVANA is compared to the fatigue damage due to the VIV response predicted by the response model approach for the different flow velocities and the different flow directions considered in chapter 4. Here method 1 has been used to find the fatigue damage.

10° flow direction

Figure 5.14 shows the comparison of the accumulated fatigue damage calculated using the response from the two different response prediction approaches at location A, approximately at the middle of the jumper length.

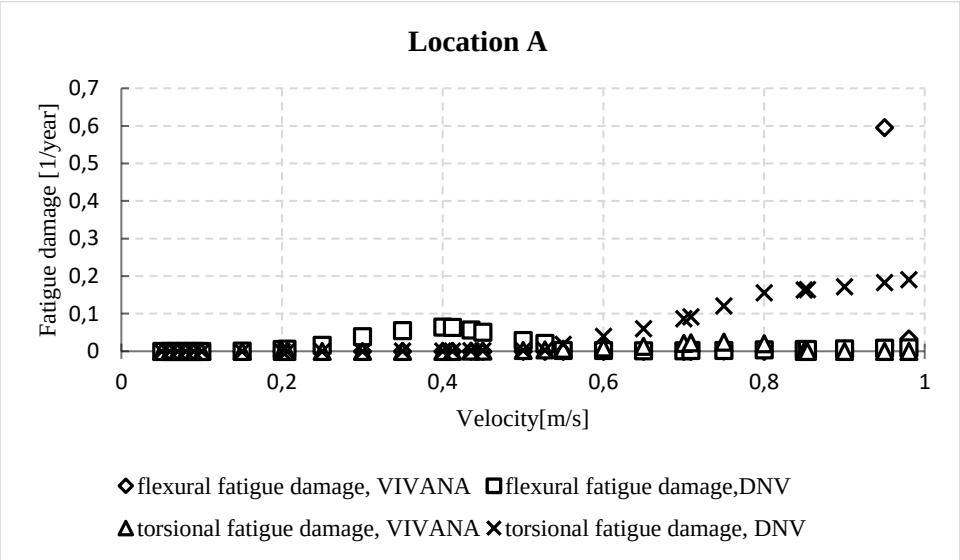

Figure 5.14. Comparison of the flexural and torsional fatigue damage at location A for the 10° flow direction.

For current velocities 0.25m/s to 0.527m/s the response model approach gives higher flexural fatigue damage than the VIVANA approach. This is probably because the response model approach predicts higher response than VIVANA for velocities smaller than 0.527m/s.

For current velocity 0.95m/s the VIVANA approach gives a much higher flexural fatigue damage than the response model approach. This is most likely because VIVANA predicts that mode 4 will be excited for this current velocity whereas the response model approach predicts that mode 2 will be the dominating mode. Figure 5.9 and 5.10 show that at location 1 (approximately the middle of the jumper length) mode 4 will give much higher modal flexural stresses than mode 2. Thus, mode 4 will give a higher flexural stress range and hence also a higher flexural fatigue damage.

For velocities larger than 0.55m/s, the response model approach gives higher torsional fatigue damage than flexural fatigue damage. The VIVANA approach give higher torsional fatigue

damage than flexural from current velocity 0.6m/s to 0.8m/s. Furthermore, for velocities larger than 0.55m/s, except for velocity 0.95m/s, the response model approach gives higher fatigue damage than the VIVANA approach. This is because for these velocities the response model approach predicts that mode 2 is the dominating mode. Whereas VIVANA predicts that mode 2 is the dominant mode for velocities 0.55m/s to 0.8m/s, mode 4 is the dominant mode for velocities 0.8m/s to 0.95m/s and mode 5 the dominating mode for velocity 0.98m/s. Figure 5.9 shows that at location A, only mode 2 will give torsional modal stresses. Thus, there will be no torsional fatigue damage due to mode 4 and 5 which is why VIVANA predicts no fatigue damage due to torsion for these velocities.

For velocities 0.55m/s to 0.8m/s VIVANA and the response model approach predicts the same dominating mode. However, the VIVANA approach gives lower torsional fatigue damage than the response model approach for these current velocities. This is because the response model approach predicts a higher response than VIVANA for all current velocities for this flow direction, and when calculating the stress ranges using the response model approach stresses due to weaker modes are also considered. This is not the case for the VIVANA approach.

In Figure 5.15 the flexural and torsional fatigue damage at location B, at the right end of the jumper, calculated using the response from the two different prediction methods is plotted against current velocity.

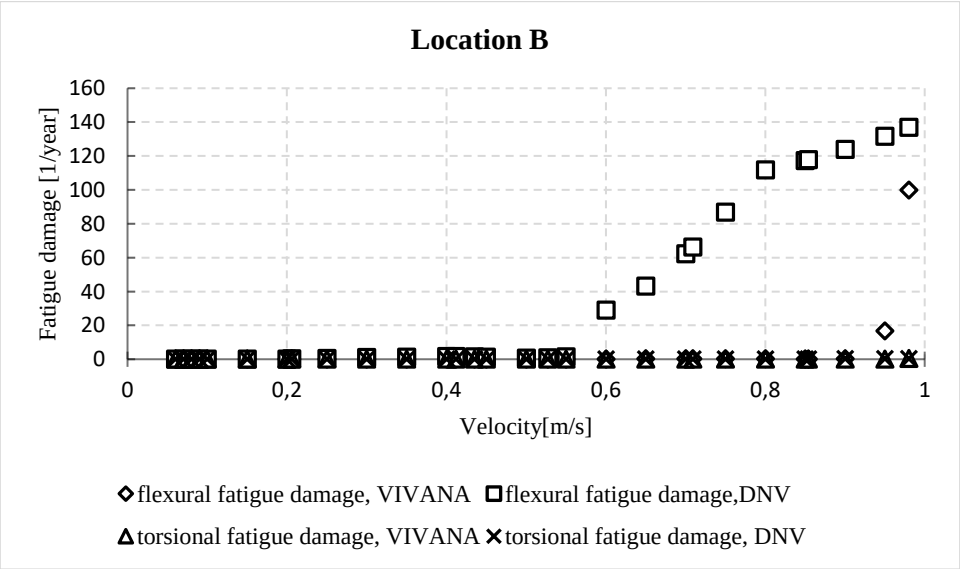

Figure 5.15. Comparison of the flexural and torsional fatigue damage at location B for the 10° flow direction.

Figure 5.15 shows that for velocities smaller than 0.6m/s the two approaches gives very little fatigue damage. For velocities larger than or equal to 0.6m/s, the response model approach gives much larger flexural fatigue damage than VIVANA. Figure C.2, in appendix C, show that the IL flexural stresses are the maximum stresses given by the response model approach. The dominating IL mode for these velocities are mode 6 (CF induced IL mode). Figure C.6 show that the CF flexural stresses are the maximum stresses given by the VIVANA approach. VIVANA predicts that mode 2 is the dominant mode for velocities 0.55m/s to 0.8m/s, mode 4 is the dominant mode for velocities 0.8m/s to 0.95m/s and mode 5 the dominating mode for velocity 0.98m/s. Figure 5.9 and 5.10 show that at location B (right end of the jumper) mode 6 gives the largest flexural stresses. The difference in mode prediction together with the the response model approach predicting larger response and considering the stress of weak modes, are the reasons why the response model approach gives larger flexureal fatigue damage than the VIVANA approach. Both the approaches give very little fatigue damage due to torsion for all current velocities.

90° flow direction

For the 90° flow direction, location B and C experience the same stresses. This is illustrated in Figure C.3, C.4, C.7, and C.8. Thus, the accumulated fatigue damage at the two locations will be the same. In Figure 5.16 the accumulated fatigue damage due to flexural and torsional stresses at location B and C, calculated using the response from the two different response prediction approaches, is plotted against current velocity.

Figure 5.16 shows that for velocities larger than 0.45m/s the response model approach gives larger flexural fatigue damage than the VIVANA approach. Figure C.3 and C.8 show that the response model appraoch gives larger stress ranges than the VIVANA approach. (Thus, the fatigue damage must be larger.) This is probably because the response model approach also considers stress due to weak modes and hence get higher stress ranges than the VIVANA approach even if the same mode is predicted to be dominant. The fatigue damage due to torsion is lower than the fatigue damage due to bending for both methods for velcities larger than 0.45m/s. For velocities smaller than 0.45m/s both methods give very little fatigue damage.

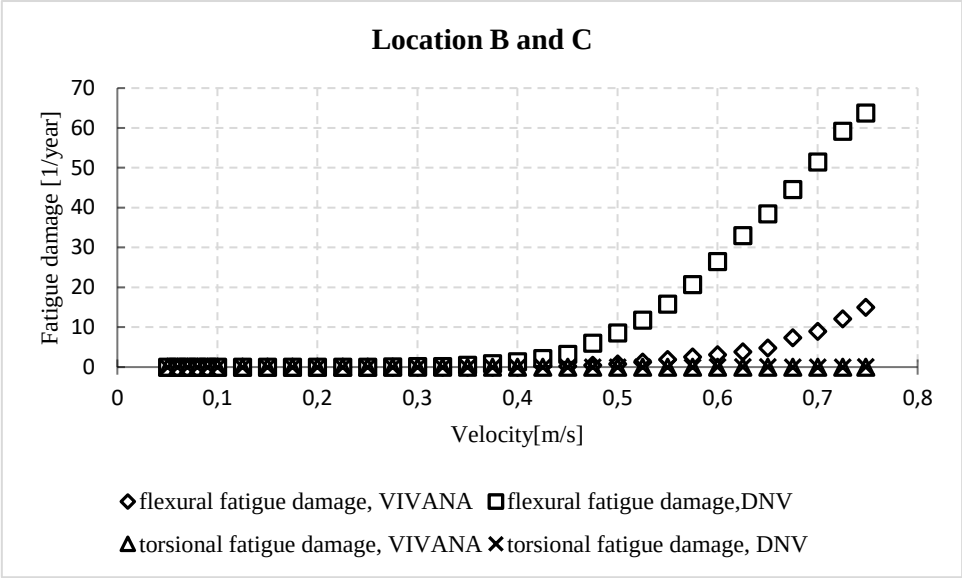

Figure 5.16. Comparison of the flexural and torsional fatigue damage at location B and C for the 90° flow direction.

5.3.2. Fatigue damage results of method 2

The fatigue damage due to the VIV response predicted by VIVANA is compared to the fatigue damage due to the VIV response predicted by the response model approach for the different flow velocities and flow directions considered in chapter 4. In this section, the fatigue damage is calculated using method 2.

10° flow direction

Figure 5.17 and 5.18 show the comparison of the accumulated fatigue damage calculated using the principal stress and the response from the two different response prediction approaches at location A and B, respectively.

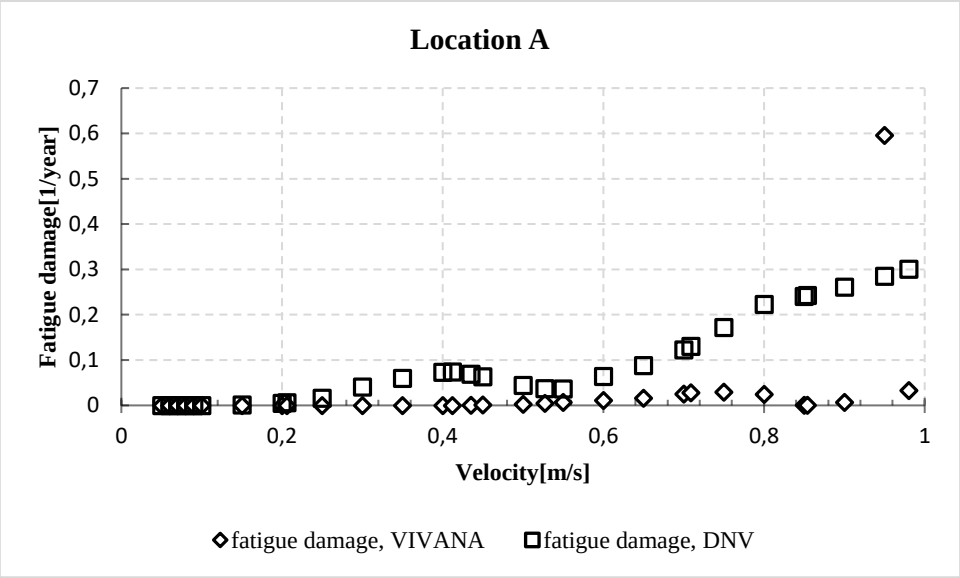

Figure 5.17. Comparison of the fatigue damage at location A for the 10° flow direction.

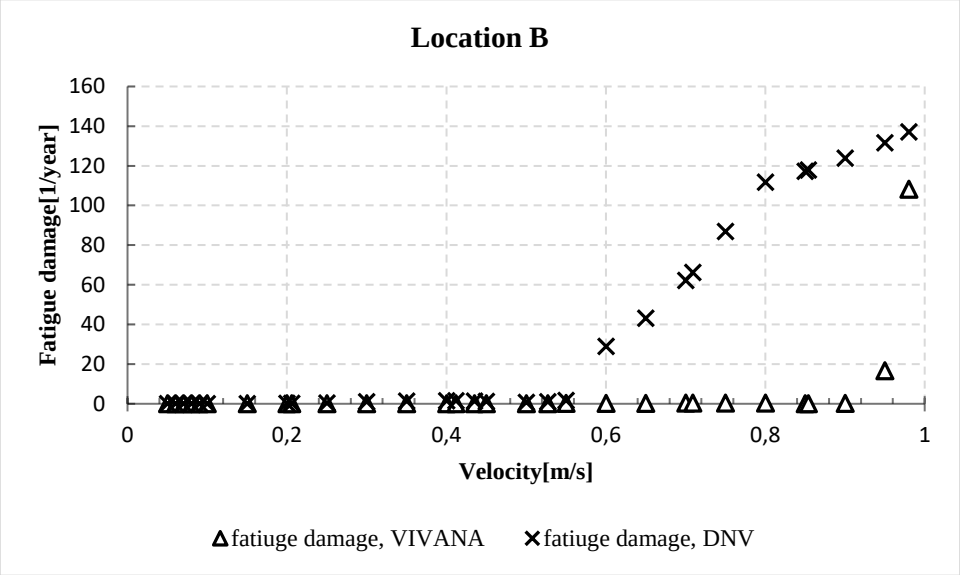

Figure 5.18. Comparison of the fatigue damage at location B for the 10° flow direction

90° flow direction

For the 90° flow direction, location B and C experience the same stresses due to the symmetry of the jumper model. Thus, the accumulated fatigue damage at the two locations will be the same. In Figure 5.19 the accumulated fatigue damage due to flexural and torsional stresses at location B and C, calculated using the response from the two different response prediction approaches, is plotted against current velocity.

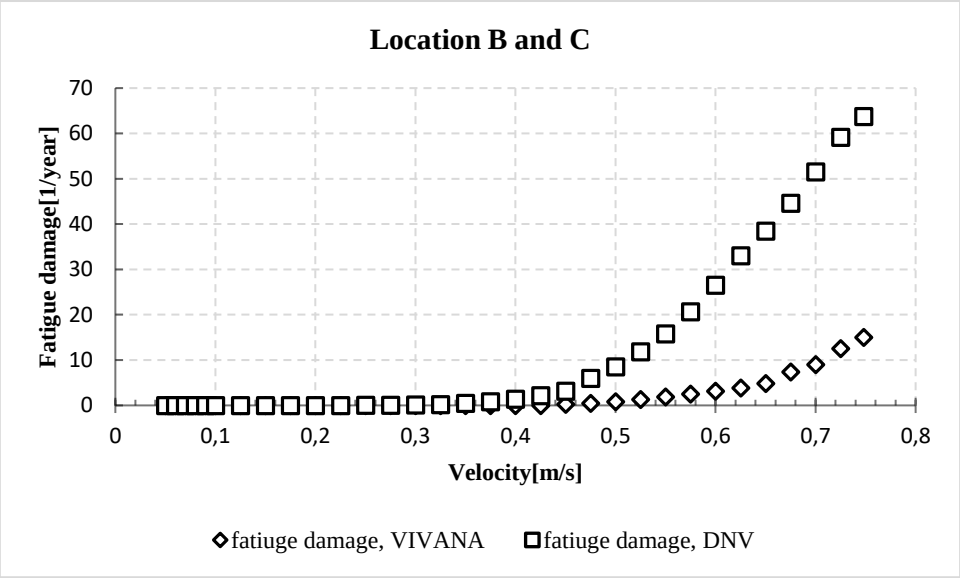

Figure 5.19. Comparison of the fatigue damage at location B and C for the 90° flow direction.

Figure 5.17, 5.18 and 5.19 show that also when using method 2 to calculate the fatigue damage, the response model approach generally gives larger fatigue damage than the VIVANA approach. This is due to the same reasons as described in section 5.3.1.

5.3.3. Comparison of the fatigue damage calculated using method 1 and method 2

Fatigue damage due to the VIV response predicted by VIVANA

In Figure 5.20, 5.21 and 5.22 the fatigue damage, at location A, B, and C, calculated using method 1 is compared to the fatigue damage calculated using method 2. In these figures, the fatigue damage is calculated using the stresses due to the VIV response predicted by VIVANA.

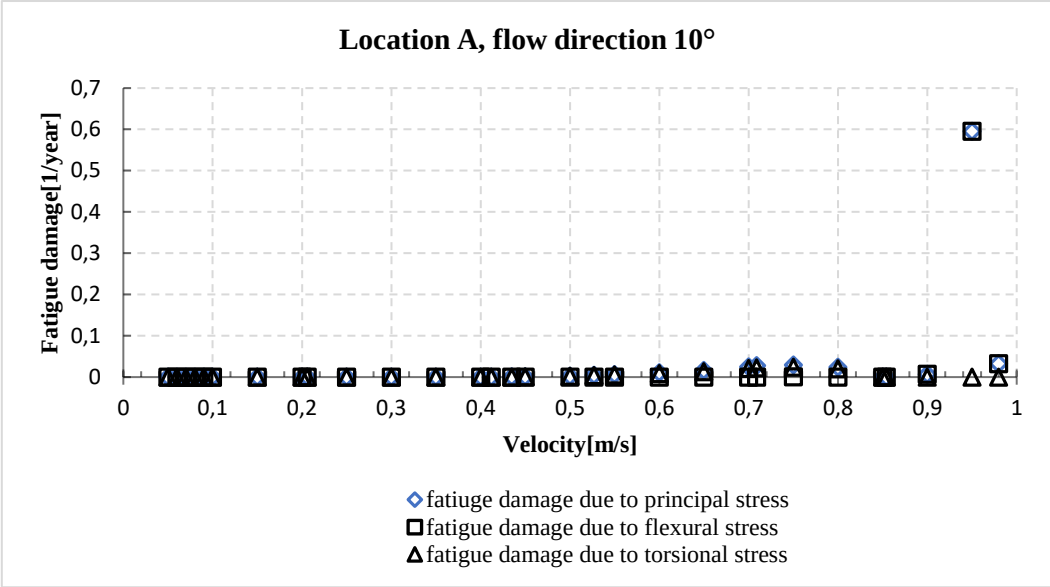

Figure 5.20. Comparison of the fatigue damage at location A calculated using method 1 and method 2 for the 10° flow direction.

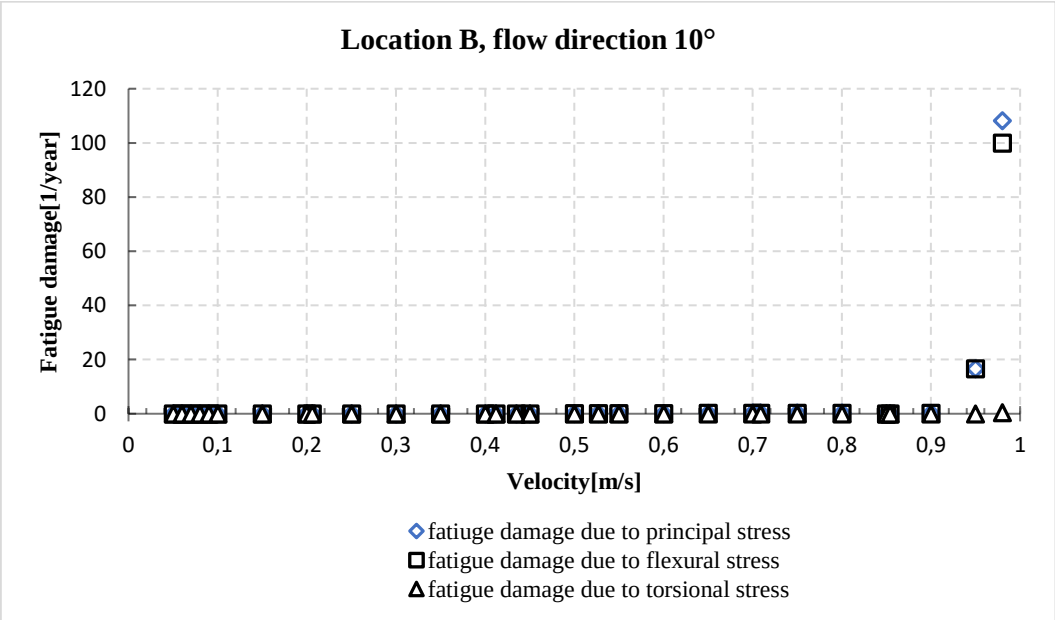

Figure 5.21. Comparison of the fatigue damage at location B calculated using method 1 and method 2 for the 10° flow direction.

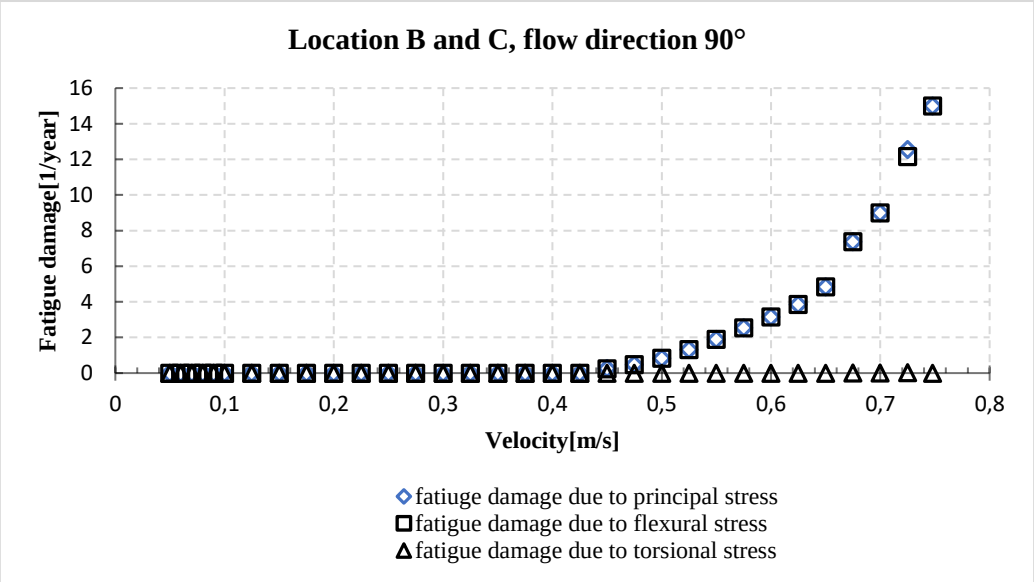

Figure 5.22. Comparison of the fatigue damage at location B and C calculated using method 1 and method 2 for the 90° flow direction.

Fatigue damage due to the VIV response predicted by the response model approach

In figure 5.23, 5.24, and 5.25 the fatigue damage, at location A, B, and C, calculated using method 1 is compared to the fatigue damage calculated using method 2. In these figures, the fatigue damage is calculated using the stresses due to the VIV response predicted by the response model approach.

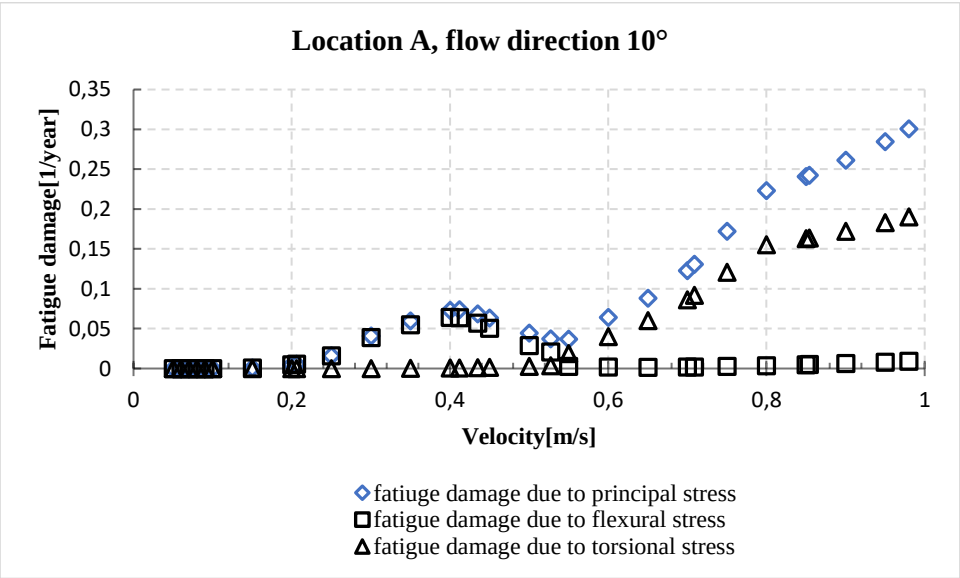

Figure 5.23. Comparison of the fatigue damage at location A calculated using method 1 and method 2 for the 10° flow direction.

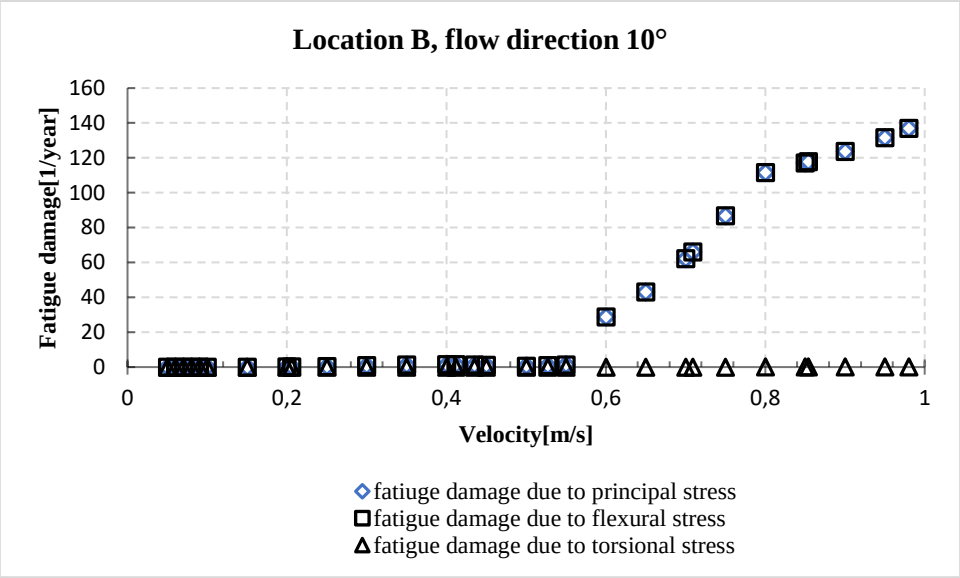

Figure 5.24. Comparison of the fatigue damage at location B calculated using method 1 and method 2 for the 10° flow direction.

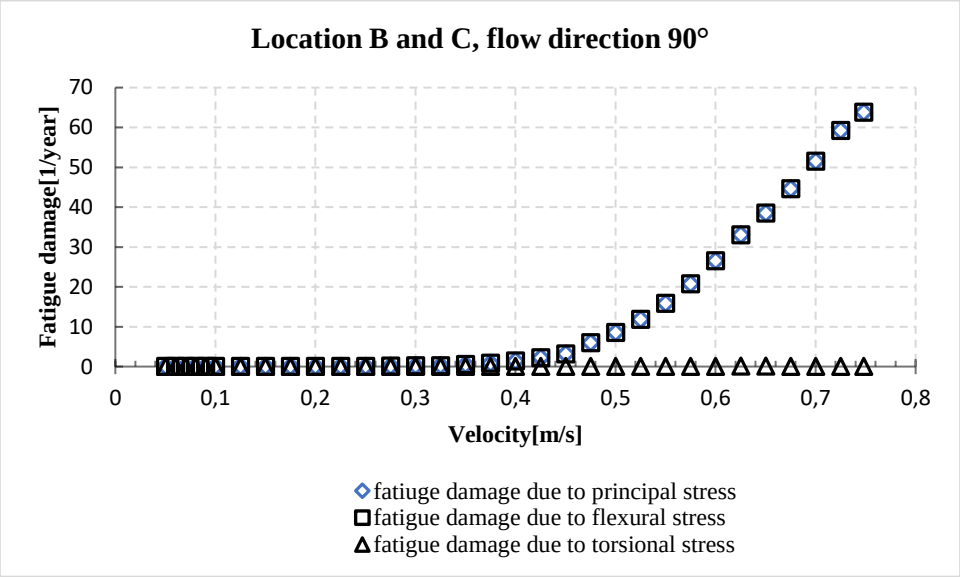

Figure 5.25. Comparison of the fatigue damage at location B and C calculated using method 1 and method 2 for the 90° flow direction

Figure 5.20 to Figure 5.25 show that the fatigue damage due to the first principal stress always is the same or larger than the maximum fatigue damage due to flexural or torsional stresses. For velocities where the torsional stresses are negligible the fatigue damage due to the first principal stress is the same as the fatigue damage due to the flexural stress.

5.4. Conclusions

The fatigue damage has been calculated using two different methods, method 1 and 2, and the VIV response predicted by the response model approach based on DNV-RP-F105 and the VIV response predicted by VIVANA. The main conclusions are as follows:

- For the 10° flow direction, the fatigue damge due to torsional stresses at location A is larger than the fatigue damage due to flexural stresses for all current velocities over 0.55m/s, except current velocity 0.95m/s. This shows that the torsional effects cannot be neglected for the jumper model considered. At location B, for the 10° flow direction, and at both locations for the 90° flow direction, the significant fatigue damage is due to flexural stresses.

- Method 1 and 2 both in general give larger fatigue damage due to the response predited by the response model approach than due to the respones predicted by VIVANA. This is because the response model approach in general predicts higher VIV response amplitudes than VIVANA, and because the ampitude response of weaker modes is not given by VIVANA and hence the stresses due to weaker modes can not be calculated. Furthermore, difference in mode predictions gives differences in the stress.

- For both flow directions and for all the flow velocities, the fatigue damage calculated using method 2 is is always conservative, and thus might be used in engineering design due to its simplicity.

- Both methods give similar results, however method 2 gives a somewhat higher fatigue damage for current velocities where the torsional stress contribution is large. This is to be expected as the combined fatigue damage due flexural and torsional stresses are considered in this method. Method 2 is also somewhat less time consuming as the fatigue damge only needs to be calculated using one type of stress.

Chapter 6: Conclusions

6.1. Summary of the Results in Chapter 4

The results from Chapter 4 can be summarized as follows:

- VIVANA gives quite good predictions of the maximum response over the jumper model for the 10° current direction. The response model approach on the other hand, largely over-predicts the maximum response for this current direction. However, for the 90° current direction both methods give quite similar predictions.

- For both current directions VIVANA generally under-predicts the response at accelerometer 3, which is located at the bend between a horizontal and vertical structural member. This is probably because of the simplified structural model with sharp corners used in present study. For the 10° current direction the response predicted by VIVANA at accelerometer 5 in y-direction show a good trend compared to the measured values. However, the response in x and z-direction due to CF loading is predicted to be zero whereas the measured values show some response in x and z-direction due to CF loading.

- For the 90° current direction the response predicted by VIVANA at accelerometer 7 in x and y-direction show a good trend compared to the measured values. However, the response in z-direction due to CF loading is predicted to be zero whereas the measured values show significant response in z-direction due to CF loading. This is probably because VIVANA predicts single mode response.

6.2. Summary of the Results in Chapter 5

The results from Chapter 5 can be summarized as follows:

- For the 10° flow direction, the fatigue damge due to torsional stresses at location A, approximately at middel of the jumper, is larger than the fatigue damage due to flexural stresses for all current velocities over 0.55m/s, except current velocity 0.95m/s. At location B, right end of the jumper, and C, left end of the jumper, the significant fatigue damage is due to flexural stresses for both current directions.

- Method 1 (fatigue damage due to torsional and flexural stresses are calculated seperately) and method 2 (fatigue damage is calculated using the first principal stress) both in general give larger fatigue damage due to the response predited by the response model approach than due to the response predicted by VIVANA.

- For both flow directions and for all the flow velocities, the fatigue damage calculated using method 2 is is always conservative, and thus might be used in engineering design due to its simplicity.

6.3. Conclusions

The main conclusions from Chapter 4 and 5 are as follows:

- The force model approach is in general applicable for VIV response prediction of 2D rigid jumper. Use of the response model approach will lead to larger over-prediction when the flow angle is oblique from the jumper plane.

- Method 1 and method 2 give similar results, however method 2 gives somewhat higher fatigue damage for current velocities where the torsional stress contribution is large. Method 2 is also slightly less time-consuming than method 1.

Chapter 7: Future work

Some recommendations for future work are given in the following:

- Re-calibrate the parameters in the existing response model given in DNV-RP-F105, or develop a new response model approach for complex jumper systems.

- Calibrate the default force coefficient database in VIVANA for pipelines and jumpers vibrating at low modes.

- Investigate if normalizing the torsional modal stresses using the maximum modal flexural displacements will capture the peak torsional stress.

- Investigate if the fatigue assessment method given in DNV-RP-F105 is applicable for multi-axial stress.

References

Amini, M., & Fernandes, A. (2015). *Experimental Evaluation of Pure In-Line Vortex Induced Vibration (VIV-X) in Subsea Jumper Subject to Ocean Current.* Paper presented at the Offshore Technology Conference, Brasil.

ANSYS Inc. (2013). *ANSYS Mechanical APDL Theory Reference*. Canonsburg, PA 15317.

ANSYS Inc. (2013). *ANSYS Mechanical APDL Structural Analysis Guide*. Canonsburg, PA 15317.

ANSYS Inc. (2015). ANSYS Mechanical [Software], version 15.0

Aronsen, K. H. (2007). *An experimental investigation of in-line and combined in-line and cross-flow vortex induced vibrations.* (Ph.D.), Norwegian University of Science and Technology, Trondheim, Norway.

Bai, Y., & Bai, Q. (2012). *Subsea Engineering Handbook*. Burlington: Elsevier Science.

Blevins, R. D. (1990). *Flow Induced Vibrations* (2nd ed.). New York, USA: Van Nostrand Reinhold.

Bybee, K. Ormen Lange Langeled Development. *Journal of Petroleum Technology*, *59*(06). doi:10.2118/0607-0047-JPT

Chaplin, J. R., Bearman, P. W., Cheng, Y., Fontaine, E., Graham, J. M. R., Herfjord, K., . . . Willden, R. H. J. (2005). Blind predictions of laboratory measurements of vortex-induced vibrations of a tension riser. *Journal of Fluids and Structures*, *21*(1), 25-40. doi:10.1016/j.jfluidstructs.2005.05.016

Chen, N.-Z., Wang, G., & Guedes Soares, C. (2011). Palmgren–Miner's rule and fracture mechanics-based inspection planning. *Engineering Fracture Mechanics*, *78*(18), 3166-3182. doi:10.1016/j.engfracmech.2011.08.002

Choi, H. S. (2001). Free spanning analysis of offshore pipelines. *Ocean Engineering*, *28*(10), 1325-1338. doi:10.1016/S0029-8018(00)00071-8

Corbetta, G., & Cox, D. S. (2001). Deepwater Tie-Ins of Rigid Lines: Horizontal Spools or Vertical Jumpers? *Society of Petroleum Engineers*. doi:10.2118/72997-PA

Deka, D., Cerkovnik, M., Panicker, N., & Achanta, V. (2013). *Subsea Jumpers Vibration Assessment.* Paper presented at the 32nd International Conference on Ocean, Offshore and Arctic Engineering (OMAE2013-11011), Nantes, France.

DNV-RP-F105 *Free spanning pipelines* (2006). DNV, Norway.

DNV-RP-C203 *Fatigue design of offshore steel structures* (2010). DNV, Norway.

Drag on objects moving through fluids [picture]. (2013). Retrieved from http://www.roymech.co.uk/Related/Fluids/Fluids_Drag.html

Gopalkrishnan, R. (1993). *Vortex-Induced Forces on Oscillating Bluff Cylinders.* (Ph.D.), Massachusetts Institute of Technology, Cambridge, MA, USA.

Gudmestad, O. T. (2015). *Marine technology and operations: theory & practice*. Southampton: WIT Press.

Gustafsson, J., & Saarinen, J. (2007). *Multi-axial fatigue in welded details -An investigation of existing design approaches.* (Thesis, Chalmers University of Technology). J.Gustafsson & J.Saarinen, Göteborg, Sweden

Hariharan, M., Cerkovnik, M. E., & Thompson, H. M. (2004). The Significance of Low Velocity Near Bottom Currents on the In-Line Vortex-Induced Vibration Response of Rigid Subsea Jumpers

Hjertager, B. (2013). *Fluid Dynamics*. University of Stavanger: McGraw-Hill Education.

Holmes, S., & Constantinides, Y. (2010). *Vortex Induced Vibration Analysis of a Complex Subsea Jumper*. Paper presented at the 29th International Conference on Ocean, Offshore and Arctic Engineering (OMAE2010-20520), Shanghai, China.

Ilstad, T., Sørreide, T., & Nielsen, F. G. (2005*). Fatigue Calculations of Multi-Mode VIV*. Proceedings of the 24th Int. Conf. on Offshore Mechanics and Artic Engineering (OMAE2005-67540), Halkdiki, Greece

Jia, J. (2014). *Essentials of Applied Dynamic Analysis*. Berlin/Heidelberg: Springer.

Jumper [picture]. (2014). Retrieved from http://www.nsl8coating.com/oil--gas

Kosanunt, P. (2015). *Fatigue analysis of subsea Jumper under external loads (steady current and earthquake).* (Thesis, Delft University of Technology).

Lafitte, J. L., Perrot, M., Lesgent, J., Bouville, J., Le Pennec, S., Dahl, P., & Lindseth, S. (2007). *Dalia Subsea Production System, Presentation and Challenges*. Paper presented at the Offshore Technology Conference, Houston, Texas, USA.

Larsen, C. M. (2011). *VIV A short and incomplete introduction to fundamental concepts*. Trondheim, Norway: Department of marine technology, Norwegian University of Science and Technology.

MARINETEK. (2011). *RIFLEX User Manual V3.6v2*.

MARINETEK. (2016). *VIVANA User Guide V4.8.0.*

Masilamani, V. (2015). *Vortex induced vibration (VIV) analysis of subsea jumper spools.* (Thesis, University of Stavanger).V.Masilamani, Stavanger, Norway.

MIT. (2016a). SHEAR7[Software].

MIT. (2016b). *Shear 7 User Guide for SHEAR7 Version 4.9b*: AMOG consulting.

Nair, A. R., Kadiyala, R. K., Whooley, A. J., Eltaher, A. H., & Jukes, P. (2011). *Torsional VIV Damage Assessment of Multi-Planar Structures*. Paper presented at the International Offshore and Polar Engineering Conference, Hawaii, USA.

Nair, A. R., Sharma, P., Grytøyr, G., Fyrileiv, O., & Vedeld, K. (2013). *VIV Assessment of Rigid Jumper Systems-A Comparative Study on Jumper Shapes.* Paper presented at the The Twenty-third International Offshore and Polar Engineering Conference, Anchorage, Alaska, USA.

Nelson, S. G. (2010). *AKPO: The Subsea Production System*. Paper presented at the Offshore Technology Conference, Houston, Texas, USA.

Nielsen, F.G., Kvarme, S.O. and Søreide, T.(2002) *VIV response of long free spanning pipelines*. Paper presented at the 21st International conference on offshore mechanics and arctic engineering, (OMAE2002-28075), Oslo, Norway.

Passano, E., Larsen, C. M., Lie, H., & Wu, J. (2016). *VIVANA Theory Manual V4.8.0*. Trondheim: MARINTEK.

Passano, Elizabeth, Carl M. Larsen, and Jie Wu.(2010) *VIV of free spanning pipelines: Comparison of response from semi-empirical code to model tests.* Paper presented at the ASME 2010 29th International Conference on Ocean, Offshore and Arctic Engineering(OMAE2010-20330), Shanghai, China.

Resvanis, T. L., Jhingran, V., Vandiver, J. K., & Liapis, S. (2012). *Reynolds number effects on the vortex-induced vibration of flexible marine risers.* Paper presented at the ASME 2012 31st International Conference on Ocean, Offshore and Arctic Engineering(OMAE2012-83565), Rio de Janeiro, Brazil.

Sintef Ocean. (2016). VIVANA[Software], version 4.8.

Slettebø, E. (2012). *Tie-in spools - a verification study*. (Thesis, University of Stavanger). E.Slettebø, Stavanger, Norway

Soni, P. K. (2008). *Hydrodynamic coefficients for vortex induced vibrations of flexible beams.* (Ph.D), NTNU, Trondheim.

Spool.[picture]. (2008). Retrieved from http://www.oceaneering.com/pipeline-connection-repair-systems/diverless-pipeline-systems/diverless-connection-and-repairsystems/

Sumer, B. M., & Fredsøe, J. (1997). *Hydrodynamics around cylindrical structures* (Vol. 12). London: World Scientific.

Søreide, T., Ilstad, T., Paulsen, G., & Nielsen, F. G. Design implementation of multi-span VIV tests

Techet, A. (2005). 13.42 Lecture: Vortex Induced Vibrations. *Massachusetts Institute of Technology, Open Courseware, 21*.

Voie, P., Wu, J., Resvanis, T., Larsen, C.M., Vandiver, J.K., Triantafyllou, M. & Baarholm, R. (2017). *Consolidation of Empirics for Calculation of VIV Response.* Paper presented at the ASME 2017, 36th International Conference on Ocean, Offshore and Arctic Engineering.

Wang, H., Huang, J., Lee, S., Gioielli, P., Kan, W., Spencer, D., & Islam, M. (2013). *VIV Response of a Subsea Jumper in Uniform Current.* Paper presented at the ASME 2013 32nd International Conference on Ocean, Offshore and Arctic Engineering(OMAE2013-11417), Nantes, France.

Zheng, H., Slocum, S. T., Huang, J. Z., Srivastava, V., Lee, S., & Wang, H. H. (2015). *Numerical Analysis of Experimental Data of Subsea Jumper Vortex Induced Vibrations.* Paper presented at the ASME 2015 34th International Conference on Ocean, Offshore and Arctic Engineering(OMAE2015-41224), Newfoundland, Canada.

Appendix A: VIVANA Output

A.1. 10° Flow Direction

Table A.1. Excited modes for the 10° flow direction.

Velocity [m/s]	pure IL	CF	IL with CF
0.05	no mode is excited	no mode is excited	no mode is excited
0.06	no mode is excited	no mode is excited	no mode is excited
0.07	1	no mode is excited	no mode is excited
0.08	1	no mode is excited	no mode is excited
0.09	1	no mode is excited	no mode is excited
0.1	1	no mode is excited	no mode is excited
0.15	1	no mode is excited	no mode is excited
0.2	3	no mode is excited	no mode is excited
0.206	3	no mode is excited	no mode is excited
0.25	3	no mode is excited	no mode is excited
0.3	3	no mode is excited	no mode is excited
0.35	3	no mode is excited	no mode is excited
0.4	3	no mode is excited	no mode is excited
0.412	3	no mode is excited	no mode is excited
0.435	3	2	7
0.45	3	2	7
0.5	7	2	7
0.527	7	2	7
0.55	7	2	7
0.6	7	2	7
0.65	7	2	7
0.7	7	2	7
0.709	8	2	8
0.75	8	2	8
0.8	8	2	8
0.85	8	4	8
0.854	8	4	8
0.9	8	4	8
0.95	8	4	8
0.98	8	5	8

Table A.2. Response frequencies for the 10° flow direction.			
Velocity [m/s]	pure IL	CF	IL with CF
0.05	no frequency is excited	no frequency is excited	no frequency is excited
0.06	no frequency is excited	no frequency is excited	no frequency is excited
0.07	0.857	no frequency is excited	no frequency is excited
0.08	0.857	no frequency is excited	no frequency is excited
0.09	0.857	no frequency is excited	no frequency is excited
0.1	0.857	no frequency is excited	no frequency is excited
0.15	0.857	no frequency is excited	no frequency is excited
0.2	2.174	no frequency is excited	no frequency is excited
0.206	2.174	no frequency is excited	no frequency is excited
0.25	2.18	no frequency is excited	no frequency is excited
0.3	2.208	no frequency is excited	no frequency is excited
0.35	2.237	no frequency is excited	no frequency is excited
0.4	2.253	no frequency is excited	no frequency is excited
0.412	2.257	no frequency is excited	no frequency is excited
0.435	2.262	2.077	4.154
0.45	2.27	2.069	4.138
0.5	3.619	2.041	4.082
0.527	3.62	2.023	4.047
0.55	3.62	2.008	4.015
0.6	3.621	1.969	3.937
0.65	3.622	1.986	3.973
0.7	3.623	2.016	4.032
0.709	3.623	2.023	4.046
0.75	6.186	2.086	4.173
0.8	6.186	2.185	4.37
0.85	6.188	2.544	5.089
0.854	6.188	2.544	5.089
0.9	6.189	2.545	5.09
0.95	6.19	2.548	5.095
0.98	6.19	3.016	6.033

Table A.3. A/D at accelerometer 3 and 5 for the 10° flow direction.						
	Acc. 3			Acc. 5		
Velocity	A/D in x-direction	A/D in y-direction	A/D in z-direction	A/D in x-direction	A/D in y-direction	A/D in z-direction
0.05	0	0	0	0	0	0
0.06	0	0	0	0	0	0
0.07	0	0	0	0	0	0
0.08	0	0	0	0	0	0
0.09	0	0	0	0	0	0
0.1	0	0	0	0	0	0
0.15	0	0	0	0	0	0
0.2	0	0	0	0	0	0
0.206	8.7625E-05	1.0627E-06	4.6084E-05	0.0005626	1.2412E-06	4.3952E-05
0.25	0.00835686	0.00014479	0.00443488	0.05385289	0.00012619	0.00423339
0.3	0.01211769	0.0002316	0.00668678	0.07938678	0.0002063	0.00639421
0.35	0.01022562	0.00018094	0.0058886	0.06823802	0.0001822	0.00564182
0.4	0.0102843	0.00023109	0.00606612	0.06934545	0.0001978	0.00582132
0.412	0.01273058	0.00033884	0.00754463	0.08600496	0.000254	0.00724298
0.435	3.3896E-06	0.03470413	4.8435E-05	5.9559E-06	0.24087603	4.8479E-05
0.45	3.974E-06	0.04110248	5.2881E-05	9.8078E-06	0.28307438	5.2904E-05
0.5	9.3712E-06	0.06179835	7.2202E-05	1.4703E-05	0.41449587	7.2197E-05
0.527	1.6017E-05	0.07446446	9.0745E-05	8.606E-06	0.49152066	9.0845E-05
0.55	1.3722E-05	0.08447603	0.00010129	1.6389E-05	0.5497686	0.00010134
0.6	3.646E-05	0.10386116	0.00015457	1.2349E-05	0.65252893	0.00015482
0.65	3.3172E-05	0.11701488	0.00017759	1.532E-05	0.74409917	0.00017795
0.7	2.1445E-05	0.13239504	0.00018091	3.2964E-05	0.85818182	0.00018126
0.709	3.6688E-05	0.13581488	0.00019825	2.6312E-05	0.88614876	0.000198
0.75	2.5965E-05	0.12975537	0.00031717	4.2744E-05	0.89561983	0.00031909
0.8	0.00016112	0.10874711	0.00032602	0.00033109	0.8252562	0.00032245
0.85	7.5841E-05	0.03988926	0.00016805	0.00023332	0.02041818	0.0001719
0.854	7.6179E-05	0.03986446	0.00016929	0.00023469	0.01738512	0.00017322
0.9	0.00015355	0.08950744	0.00028398	0.00027646	0.09673719	0.00029005
0.95	0.00022164	0.01990744	0.00030402	0.00046536	0.48123967	0.00029301
0.98	0.0001837	0.78241322	0.00011913	0.00020808	0.17644628	0.0001216

Table A.4. Maximum A/D for the 10° flow direction.						
	IL			CF		
Velocity[m/s]	Max. Ax/D	Max. Ay/D	Max. Az/D	Max. Ax/D	Max. Ay/D	Max. Az/D
0.05						
0.06						
0.07						
0.08						
0.09						
0.1						
0.15						
0.2						
0.206	5.6E-04	1.2E-06	8.5E-05			
0.25	5.4E-02	1.3E-04	8.2E-03			
0.3	7.9E-02	2.1E-04	1.2E-02			
0.35	6.8E-02	1.8E-04	1.1E-02			
0.4	6.9E-02	2.0E-04	1.1E-02			
0.412	8.6E-02	2.5E-04	1.4E-02			
0.435	1.5E-05	1.3E-03	9.3E-05	4.1E-04	2.4E-01	1.1E-03
0.45	1.8E-05	1.4E-03	1.0E-04	4.8E-04	2.8E-01	1.3E-03
0.5	2.2E-05	1.8E-03	1.4E-04	7.2E-04	4.1E-01	2.0E-03
0.527	1.7E-05	2.1E-03	1.7E-04	8.6E-04	4.9E-01	2.6E-03
0.55	2.9E-05	2.4E-03	2.0E-04	9.6E-04	5.5E-01	3.1E-03
0.6	2.7E-05	3.3E-03	2.8E-04	1.2E-03	6.5E-01	3.7E-03
0.65	3.9E-05	3.9E-03	3.3E-04	1.7E-03	7.4E-01	3.9E-03
0.7	5.5E-05	4.3E-03	3.6E-04	2.5E-03	8.6E-01	6.2E-03
0.709	3.8E-05	4.6E-03	3.8E-04	2.8E-03	8.9E-01	7.0E-03
0.75	8.1E-05	7.8E-03	6.1E-04	4.9E-03	9.0E-01	8.6E-03
0.8	3.3E-04	2.9E-03	3.2E-04	1.8E-02	8.3E-01	1.0E-02
0.85	2.3E-04	1.6E-03	1.7E-04	1.7E-02	3.3E-02	2.8E-02
0.854	2.3E-04	1.6E-03	1.7E-04	1.7E-02	3.3E-02	2.8E-02
0.9	2.8E-04	2.0E-03	3.9E-04	2.2E-02	1.1E-01	3.5E-02
0.95	4.7E-04	3.5E-03	6.7E-04	2.1E-02	4.7E-01	3.5E-02
0.98	2.1E-04	1.7E-03	2.9E-04	6.0E-03	7.8E-01	6.2E-03

A.2 90° Flow Direction

Table A.5. Excited modes for the 90° flow direction.			
Velocity [m/s]	pure IL	CF	IL with CF
0.05	no mode is excited	no mode is excited	no mode is excited
0.06	no mode is excited	no mode is excited	no mode is excited
0.07	1	no mode is excited	no mode is excited
0.08	1	no mode is excited	no mode is excited
0.09	1	no mode is excited	no mode is excited
0.1	1	no mode is excited	no mode is excited
0.125	1	no mode is excited	no mode is excited
0.15	1	no mode is excited	no mode is excited
0.175	1	no mode is excited	no mode is excited
0.2	1	no mode is excited	no mode is excited
0.225	1	no mode is excited	no mode is excited
0.25	2	no mode is excited	no mode is excited
0.275	2	no mode is excited	no mode is excited
0.3	2	no mode is excited	no mode is excited
0.325	2	no mode is excited	no mode is excited
0.35	2	no mode is excited	no mode is excited
0.375	2	no mode is excited	no mode is excited
0.4	2	no mode is excited	no mode is excited
0.425	5	no mode is excited	no mode is excited
0.45	5	3	7
0.475	5	3	7
0.5	5	3	7
0.525	5	3	7
0.55	5	3	7
0.575	5	3	7
0.6	5	3	7
0.625	5	3	7
0.65	5	3	7
0.675	5	3	7
0.7	5	3	7
0.725	5	3	7
0.748	5	3	8

Table A.6. Response frequencies for the 90° flow direction.			
Velocity [m/s]	pure IL	CF	IL with CF
0.05	No response frequency	No response frequency	No response frequency
0.06	No response frequency	No response frequency	No response frequency
0.07	0.858	No response frequency	No response frequency
0.08	0.858	No response frequency	No response frequency
0.09	0.861	No response frequency	No response frequency
0.1	0.866	No response frequency	No response frequency
0.125	0.902	No response frequency	No response frequency
0.15	0.936	No response frequency	No response frequency
0.175	0.957	No response frequency	No response frequency
0.2	0.987	No response frequency	No response frequency
0.225	1.027	No response frequency	No response frequency
0.25	2.159	No response frequency	No response frequency
0.275	2.184	No response frequency	No response frequency
0.3	2.227	No response frequency	No response frequency
0.325	2.275	No response frequency	No response frequency
0.35	2.307	No response frequency	No response frequency
0.375	2.334	No response frequency	No response frequency
0.4	2.357	No response frequency	No response frequency
0.425	3.342	No response frequency	No response frequency
0.45	3.383	2.12	4.24
0.475	3.433	2.111	4.223
0.5	3.48	2.1	4.199
0.525	3.51	2.089	4.179
0.55	3.539	2.076	4.151
0.575	3.566	2.063	4.126
0.6	3.913	2.048	4.096
0.625	3.94	2.037	4.073
0.65	3.966	2.044	4.088
0.675	3.647	2.051	4.101
0.7	3.664	2.061	4.121
0.725	3.69	2.077	4.153
0.748	3.733	2.097	4.195

Table A.7. A/D at accelerometer 3 and 7 for the 90° flow direction.						
	acc3			acc7		
Velocity[m/s]	A/D in x-direction	A/D in y-direction	A/D in z-direction	A/D in x-direction	A/D in y-direction	A/D in z-direction
0.05						
0.06						
0.07	3.417E-07	0.00056476	5.9952E-07	2.0977E-09	0.01134	3.5311E-06
0.08	1.4708E-06	0.00186099	2.5805E-06	9.0278E-09	0.03736529	1.5197E-05
0.09	3.1944E-06	0.00319174	5.603E-06	1.9595E-08	0.06407603	3.2987E-05
0.1	4.5693E-06	0.0036924	8.0098E-06	2.7992E-08	0.07412231	4.7124E-05
0.125	1.0793E-05	0.00552298	1.8846E-05	6.5512E-08	0.11086777	0.11086777
0.15	0.0000168	0.00590893	2.9226E-05	1.0107E-07	0.11860992	0.0001703
0.175	1.8455E-05	0.00473752	3.2026E-05	3.2026E-05	0.09507934	0.00018603
0.2	2.7864E-05	0.00542017	4.8177E-05	1.652E-07	0.10879339	0.00027853
0.225	1.957E-05	0.00296579	3.3671E-05	1.1466E-07	0.05955207	0.00019344
0.25	0.00030412	0.01156198	0.00012781	0.00182529	6.8873E-05	1.1076E-06
0.275	0.00042668	0.01368397	0.00026453	0.00284149	8.1526E-05	1.9445E-06
0.3	0.00019889	0.01641008	0.00022509	0.00165653	9.7734E-05	1.3575E-06
0.325	9.8073E-05	0.01817686	0.00021641	0.00115795	0.00010828	1.1215E-06
0.35	5.416E-05	0.01619074	0.00020035	0.0008974	9.6493E-05	9.5537E-07
0.375	3.9845E-05	0.019	0.00025258	0.00099026	0.00011307	1.1029E-06
0.4	0.0000178	0.01293289	0.0001875	0.00066367	7.6985E-05	7.7519E-07
0.425	0.00114382	0.10714876	0.00093231	4.9936E-07	0.00722529	0.000426
0.45	0.04379504	0.08857355	0.02196694	0.2747438	1.6628E-05	0.00061858
0.475	0.05480331	0.08964793	0.02880661	0.34852893	1.696E-05	0.0012601
0.5	0.06727603	0.09042975	0.03336529	0.41919008	1.5221E-05	0.00107383
0.525	0.0788281	0.0990314	0.03887273	0.48955372	1.7595E-05	0.00136699
0.55	0.08930909	0.11037355	0.04431074	0.55466116	1.3616E-05	0.00136221
0.575	0.09740992	0.12073884	0.05029587	0.61145455	1.9936E-05	0.00257521
0.6	0.10727438	0.13040826	0.05214215	0.65922314	1.7293E-05	0.00222744
0.625	0.11465124	0.14090248	0.0563124	0.70575207	1.836E-05	0.00161617
0.65	0.12219339	0.15192893	0.06194215	0.76049587	1.6663E-05	0.00206
0.675	0.14033554	0.16223802	0.07116198	0.87446281	1.9712E-05	0.00205769
0.7	0.15044463	0.24533884	0.07442149	0.93153719	3.5127E-05	0.00149221
0.725	0.16509752	0.32424793	0.08259174	1.02781818	5.0152E-05	0.00297273
0.748	0.17287603	0.0632314	0.09149917	1.09869421	0.28152066	0.01052992

Table A.8. Maximum A/D for the 90° flow direction.						
	IL			CF		
Velocity[m/s]	Ax/D	Ay/D	Az/D	Ax	Ay	Az
0.05						
0.06						
0.07	2.0977E-09	0.01134	3.5311E-06			
0.08	9.0278E-09	0.03736529	1.5197E-05			
0.09	1.9595E-08	0.06407603	3.2987E-05			
0.1	2.7992E-08	0.07412231	4.7124E-05			
0.125	6.5512E-08	0.11086777	0.00011034			
0.15	1.0107E-07	0.11860992	0.0001703			
0.175	1.1038E-07	0.09507934	0.00018603			
0.2	1.652E-07	0.10879339	0.00027853			
0.225	1.1466E-07	0.05955207	0.00019344			
0.25	0.00184678	0.08541488	0.0002038			
0.275	0.00282215	0.10110413	0.00048987			
0.3	0.00158896	0.12126281	0.00063797			
0.325	0.00106443	0.13429587	0.00076198			
0.35	0.00079934	0.11967769	0.0007659			
0.375	0.00085785	0.14044793	0.00101575			
0.4	0.00056088	0.09556694	0.00077878			
0.425	0.00113894	0.10735041	0.0009274			
0.45	0.00125154	0.08857355	0.00108489	0.27472727	0.02534215	0.0407157
0.475	0.00142655	0.08964793	0.00124322	0.34852893	0.02826942	0.05286446
0.5	0.00161623	0.09042975	0.00141775	0.41919008	0.02918182	0.06180992
0.525	0.00197488	0.0990314	0.00174231	0.48955372	0.03096033	0.07202314
0.55	0.00245901	0.11037355	0.00218661	0.55466116	0.03080496	0.08194215
0.575	0.00299025	0.12073884	0.00267851	0.61145455	0.03115702	0.09220826
0.6	0.00359769	0.13040826	0.0032519	0.65923967	0.03034711	0.09655702
0.625	0.00429388	0.14090248	0.00390744	0.7057686	0.03112066	0.10392066
0.65	0.00493306	0.15192893	0.0044686	0.76054545	0.03916198	0.1136314
0.675	0.00560198	0.16223802	0.00505256	0.87452893	0.05237521	0.13053058
0.7	0.00901702	0.24533884	0.00808711	0.93165289	0.0679719	0.13716694
0.725	0.01251058	0.32424793	0.01111686	1.02803306	0.10197355	0.15330579
0.748	0.00268099	0.28152066	0.00785835	1.09907438	0.16783471	0.16689256

Appendix B: Response Model Calculations and Results

B.1 10° Flow Direction

From the eigenvalue analysis done in VIVANA the frequencies and mode shapes of the model jumper are found. When the current hits the jumper plane at a 10°angle it is assumed that IL is in x -direction and CF is in y-direction for the vertical members with regards to the jumper's coordinate system. Hence, the mode shapes that gives response in y-direction are taken as CF modes whereas the mode shapes that gives response in x- direction are taken as IL mode.

According to the DNV-RP-F105, three «contributing» CF modes and four «contributing» IL modes are considered sufficient to capture the underlying physics and provide accurate engineering for most practical cases. Table B.1 show the contributing CF and IL modes for this flow direction.

Table B.1. Contributing IL and CF modes for the 10° flow direction.

Eigen mode	Frequency [Hz]	CF mode	IL mode
1	0.8587	1	
2	2.1403	2	
3	2.1741		1
4	2.5457		2
5	3.2669	3	
6	3.56		3
7	3.6218	4	
8	6.1957	5	
9	6.911		4

In the model test the jumper is towed at a specified speed, just as if the jumper was exposed to a uniform current. This means that the jumper is exposed to pure current flow ($\alpha = 1$). Hence, the response models apply in both IL and CF directions according to the DNV-RP-F105. The inputs used to construct the IL and CF response models are shown in Table B.2.

Table B.2. Response model parameters for the 10° flow direction		
Parameter	Value	
γ_k	1.3	Assume safety class is high
γ_f	1.15	Assume safety class is high and span is well defined
$\gamma_{on,IL}$	1.1	For all safety classes
$\gamma_{on,CF}$	1.2	For all safety classes
ξ_{st}	0.01	As set in VIVANA
m_e	9.829 kg/m	$m_e = m_{pipe} + m_{content} + m_a$
m_a	2.95kg/m	Calculated assuming $C_a = 1$
$m_{pipe} + m_{content}$	6.879kg/m	
D	0.0605m	
ρ_{water}	1027kg/m^3	
I_c	0.05	According to the RP if no information is available
θ_{rel}	0.174 rad	

Using the parameters in Table B.2 above, and the equations in chapter 3.1.1, the response curves in Figure B.1 and B.2 have been constructed.

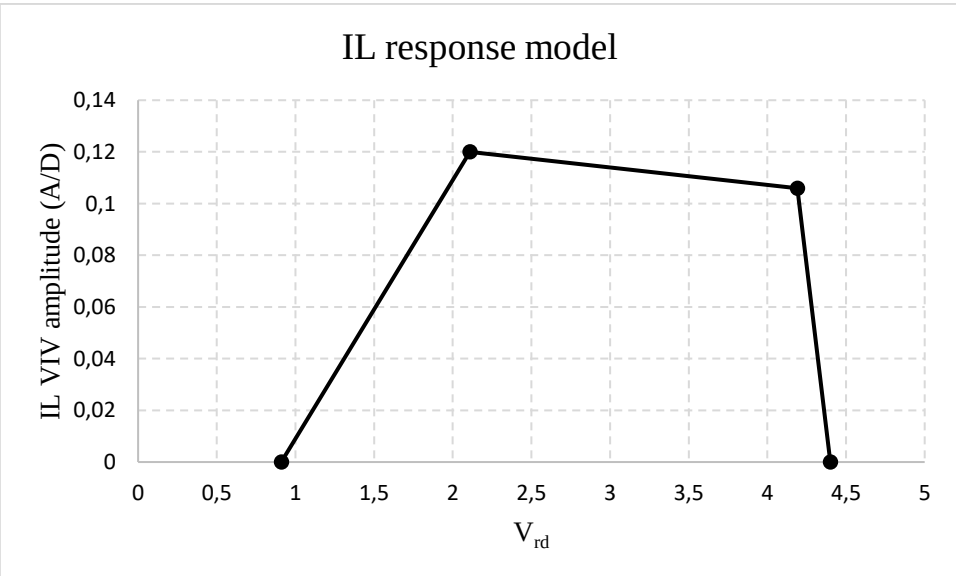

Figure B.1. IL response model for the 10° flow direction.

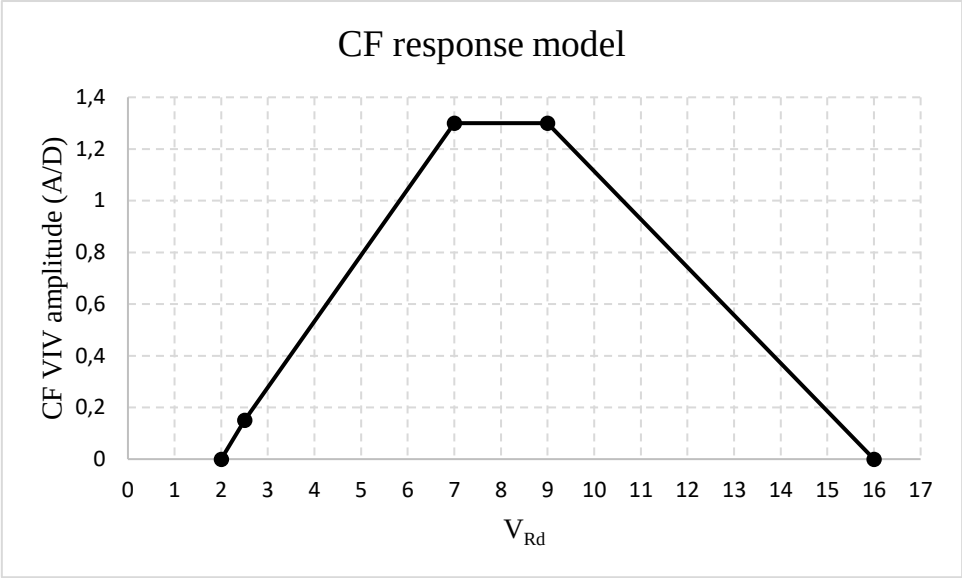

Figure B.2. CF response model for the 10° flow direction.

The reduced velocities are calculated for current velocities between 0.05-0.98 m/s and the 3 first CF modes and the 4 first IL modes. The reduced velocities are shown in Table B.3 and B.4. According to the DNV-RP-F105 a simple and conservative procedure to check for multi-mode response is to check if the following criterions are satisfied for each mode.

$$V_{Rd,CF} > 2 \quad for\ cross - flow$$

$$V_{Rd,IL} > 1 \qquad for\ in - line$$

If the criterion is only satisfied by one mode, the response is single mode. If not, the response is multi-mode. For current velocities that give multi-mode response, the mode that gives the largest A/D is chosen as the dominant mode for the CF analysis. For the IL analysis, the dominating mode is the mode associated with the largest unit amplitude stress. Every adjacent mode combination needs to be checked to see if they are competing. Two modes are competing if

$$\frac{f_{n+1}}{f_n} < 2$$

The IL mode associated with the largest stress of the two competing modes is the dominant mode of the two.

To find the dominating mode for CF induced IL VIV, the IL mode with frequency closest to twice the dominant CF response frequency ($f_{n,CF-RES}$) is chosen.

Table B.3, B.4 and B.5 show which modes that are dominating for each current velocity.

Table B.3. Dominating IL mode for the 10° flow direction.

Velocity	IL freq.1	assosiated Vrd	IL freq.2	assosiated Vrd	IL freq. 3	assosiated Vrd	IL freq.4	assosiated Vrd	Dominating IL mode
0.05	2.1741	0.44	2.5457	0.37	3.56	0.27	6.911	0.14	-
0.06	2.1741	0.52	2.5457	0.45	3.56	0.32	6.911	0.17	-
0.07	2.1741	0.61	2.5457	0.52	3.56	0.37	6.911	0.19	-
0.08	2.1741	0.70	2.5457	0.60	3.56	0.43	6.911	0.22	-
0.09	2.1741	0.79	2.5457	0.67	3.56	0.48	6.911	0.25	-
0.1	2.1741	0.87	2.5457	0.75	3.56	0.53	6.911	0.28	-
0.15	2.1741	1.31	2.5457	1.12	3.56	0.80	6.911	0.41	Mode 4
0.2	2.1741	1.75	2.5457	1.49	3.56	1.07	6.911	0.55	Mode 6
0.206	2.1741	1.80	2.5457	1.54	3.56	1.10	6.911	0.57	Mode 6
0.25	2.1741	2.19	2.5457	1.87	3.56	1.33	6.911	0.69	Mode 6
0.3	2.1741	2.62	2.5457	2.24	3.56	1.60	6.911	0.83	Mode 6
0.35	2.1741	3.06	2.5457	2.61	3.56	1.87	6.911	0.96	Mode 6
0.4	2.1741	3.50	2.5457	2.99	3.56	2.14	6.911	1.10	Mode 9
0.412	2.1741	3.60	2.5457	3.08	3.56	2.20	6.911	1.13	Mode 9
0.435	2.1741	3.80	2.5457	3.25	3.56	2.32	6.911	1.20	Mode 9
0.45	2.1741	3.93	2.5457	3.36	3.56	2.40	6.911	1.24	Mode 9
0.5	2.1741	4.37	2.5457	3.73	3.56	2.67	6.911	1.38	Mode 9
0.527	2.1741	4.61	2.5457	3.94	3.56	2.81	6.911	1.45	Mode 9
0.55	2.1741	4.81	2.5457	4.11	3.56	2.94	6.911	1.51	Mode 9
0.6	2.1741	5.25	2.5457	4.48	3.56	3.20	6.911	1.65	Mode 9
0.65	2.1741	5.68	2.5457	4.85	3.56	3.47	6.911	1.79	Mode 9
0.7	2.1741	6.12	2.5457	5.23	3.56	3.74	6.911	1.93	Mode 9
0.709	2.1741	6.20	2.5457	5.29	3.56	3.79	6.911	1.95	Mode 9
0.75	2.1741	6.56	2.5457	5.60	3.56	4.00	6.911	2.06	Mode 9
0.8	2.1741	6.99	2.5457	5.97	3.56	4.27	6.911	2.20	Mode 9
0.85	2.1741	7.43	2.5457	6.35	3.56	4.54	6.911	2.34	Mode 9
0.854	2.1741	7.47	2.5457	6.38	3.56	4.56	6.911	2.35	Mode 9
0.9	2.1741	7.87	2.5457	6.72	3.56	4.81	6.911	2.48	Mode 9
0.95	2.1741	8.31	2.5457	7.09	3.56	5.07	6.911	2.61	Mode 9
0.98	2.1741	8.57	2.5457	7.32	3.56	5.23	6.911	2.70	Mode 9

Table B.4. Dominating CF mode for the 10° flow direction.							
Velocity	CF freq. 1	assosiated Vrd	CF freq. 2	assosiated Vrd	CF freq. 3	assosiated Vrd	Dominating CF mode
0.05	0.8587	1.11	2.1403	0.44	3.2669	0.29	-
0.06	0.8587	1.33	2.1403	0.53	3.2669	0.35	-
0.07	0.8587	1.55	2.1403	0.62	3.2669	0.41	-
0.08	0.8587	1.77	2.1403	0.71	3.2669	0.47	-
0.09	0.8587	1.99	2.1403	0.80	3.2669	0.52	-
0.1	0.8587	2.21	2.1403	0.89	3.2669	0.58	-
0.15	0.8587	3.32	2.1403	1.33	3.2669	0.87	mode 1
0.2	0.8587	4.43	2.1403	1.78	3.2669	1.16	mode 1
0.206	0.8587	4.56	2.1403	1.83	3.2669	1.20	mode 1
0.25	0.8587	5.53	2.1403	2.22	3.2669	1.45	mode 1
0.3	0.8587	6.64	2.1403	2.66	3.2669	1.75	mode 1
0.35	0.8587	7.75	2.1403	3.11	3.2669	2.04	mode 1
0.4	0.8587	8.85	2.1403	3.55	3.2669	2.33	mode 1
0.412	0.8587	9.12	2.1403	3.66	3.2669	2.40	mode 1
0.435	0.8587	9.63	2.1403	3.86	3.2669	2.53	mode 1
0.45	0.8587	9.96	2.1403	4.00	3.2669	2.62	mode 1
0.5	0.8587	11.07	2.1403	4.44	3.2669	2.91	mode 1
0.527	0.8587	11.67	2.1403	4.68	3.2669	3.07	mode 1
0.55	0.8587	12.17	2.1403	4.88	3.2669	3.20	mode 2
0.6	0.8587	13.28	2.1403	5.33	3.2669	3.49	mode 2
0.65	0.8587	14.39	2.1403	5.77	3.2669	3.78	mode 2
0.7	0.8587	15.50	2.1403	6.22	3.2669	4.07	mode 2
0.709	0.8587	15.69	2.1403	6.30	3.2669	4.13	mode 2
0.75	0.8587	16.60	2.1403	6.66	3.2669	4.36	mode 2
0.8	0.8587	17.71	2.1403	7.10	3.2669	4.65	mode 2
0.85	0.8587	18.82	2.1403	7.55	3.2669	4.95	mode 2
0.854	0.8587	18.90	2.1403	7.58	3.2669	4.97	mode 2
0.9	0.8587	19.92	2.1403	7.99	3.2669	5.24	mode 2
0.95	0.8587	21.03	2.1403	8.44	3.2669	5.53	mode 2
0.98	0.8587	21.69	2.1403	8.70	3.2669	5.70	mode 2

Table B.5. Dominating CF induced IL mode for the 10° flow direction						
Velocity	fn	Vr	Ca,CF-RES	fn,CF-RES	2*fn,CF-RES	IL mode closest to 2*fn,CF-RES
0.05						
0.06						
0.07						
0.08						
0.09						
0.1						
0.15	0.8587	2.89	4.11	0.6175	1.2350	mode 3
0.2	0.8587	3.85	4.15	0.6156	1.2311	mode 3
0.206	0.8587	3.97	4.03	0.6213	1.2427	mode 3
0.25	0.8587	4.81	3.19	0.6670	1.3339	mode 3
0.3	0.8587	5.77	2.23	0.7338	1.4676	mode 3
0.35	0.8587	6.74	1.26	0.8270	1.6540	mode 3
0.4	0.8587	7.70	0.3	0.9662	1.9325	mode 3
0.412	0.8587	7.93	0.07	1.0115	2.0230	mode 3
0.435	0.8587	8.37	-0.37	1.1193	2.2385	mode 3
0.45	0.8587	8.66	-0.5	1.1583	2.3167	mode 3
0.5	0.8587	9.62	-0.5	1.1583	2.3167	mode 3
0.527	0.8587	10.14	-0.5	1.1583	2.3167	mode 3
0.55	0.8587	10.59	-0.5	1.1583	2.3167	mode 3
0.6	2.1403	4.63	3.37	1.6359	3.2718	mode 6
0.65	2.1403	5.02	2.98	1.6949	3.3898	mode 6
0.7	2.1403	5.41	2.59	1.7608	3.5216	mode 6
0.709	2.1403	5.48	2.52	1.7735	3.5470	mode 6
0.75	2.1403	5.79	2.21	1.8330	3.6661	mode 6
0.8	2.1403	6.18	1.82	1.9172	3.8344	mode 6
0.85	2.1403	6.56	1.44	2.0115	4.0231	mode 6
0.854	2.1403	6.60	1.4	2.0223	4.0446	mode 6
0.9	2.1403	6.95	1.05	2.1244	4.2488	mode 6
0.95	2.1403	7.34	0.66	2.2587	4.5174	mode 6
0.98	2.1403	7.57	0.43	2.3509	4.7019	mode 6

Using the IL response model and the V_{Rd} calculated using the eigenfrequency of the dominating mode, the maximum A/D due to IL loading can be found for each current velocity. For mode 3 (IL mode 1) the maximum response will be in x-direction according to its mode shape. At the location where x is maximum, the maximum z is 0.13. Hence, the maximum response in x-direction is found by using the response curve in Figure B.1 while the corresponding response in z-direction is found by multiplying the response curve values with 0.13.

For mode 4 (IL mode 2) the maximum response will be in z-direction according to its mode shape. At the location where z is at is maximum, the maximum x is 0. Hence, the maximum response in z-direction is found by using the response curve in figure B.1 while the corresponding response in x-direction is found by multiplying the response curve values with 0. (I.e. no response in x-direction)

For mode 6 (IL mode 3) the maximum response will be in z-direction according to its mode shape. At the location where z is at is maximum, the maximum x is 0.88. Hence, the maximum response in z-direction is found by using the response curve in figure B.1 while the corresponding response in x-direction is found by multiplying the response curve values with 0.88.

Using the CF response model and the V_{Rd} calculated using the eigenfrequency of the dominating CF mode, the maximum A/D due to CF loading can be found for each current velocity. As the CF response is in y-direction, the maximum A/D due to CF loading will be in y-direction.

The calculated maximum A/D in x, y and z-directions are shown in Table B.6.

Table B.6. Maximum A/D for the 10° flow direction.			
Velocity[m/s]	Max. A/D in x-direction	Max. A/D in y-direction	Max. A/D in z-direction
0.05			
0.06			
0.07			
0.08			
0.09			
0.1			
0.15	0.04	0.36	0.01
0.2	0.08	0.64	0.01
0.206	0.09	0.68	0.01
0.25	0.12	0.92	0.02
0.3	0.12	1.21	0.02
0.35	0.11	1.30	0.02
0.4	0.41	1.30	0.06
0.412	0.43	1.28	0.06
0.435	0.48	1.18	0.07
0.45	0.52	1.12	0.07
0.5	0.63	0.92	0.09
0.527	0.69	0.80	0.09
0.55	0.21	0.76	0.26
0.6	0.27	0.87	0.33
0.65	0.33	0.99	0.40
0.7	0.39	1.10	0.47
0.709	0.39	1.12	0.48
0.75	0.43	1.21	0.53
0.8	0.49	1.30	0.60
0.85	0.55	1.30	0.67
0.854	0.56	1.30	0.68
0.9	0.61	1.30	0.74
0.95	0.66	1.30	0.81
0.98	0.70	1.30	0.85

B.2. 90° Flow Direction

When the current hits the jumper plane at a 90° angle it is assumed that the IL response is in y-direction and the CF response is in x-direction for vertical members and in z-direction for horizontal members. Table B.7 shows the contributing IL and CF modes for this flow direction.

Table B.7 Contributing IL and CF modes for the 90° flow direction.

Eigen mode	Frequency [Hz]	CF mode	IL mode
1	0.8587		1
2	2.1403		2
3	2.1741	1	
4	2.5457	2	
5	3.2669		3
6	3.56	3	
7	3.6218		4

The inputs used to construct the IL and CF response models are shown in Table B.8 below.

Table B.8. Response model parameters for the 90° flow direction.

Parameter	Value	
γ_k	1.3	Assume safety class is high
γ_f	1.15	Assume safety class is high and span is well defined
ξ_{st}	0.01	As set in VIVANA
m_e	9.829 kg/m	$m_e = m_{pipe} + m_{content} + m_a$
m_a	2.95kg/m	Calculated assuming $C_a = 1$
$m_{pipe} + m_{content}$	6.879kg/m	
D	0.0605m	
ρ_{water}	1027kg/m^3	
I_c	0.05	According to the RP if no information is available
θ_{rel}	1.57 rad	

Using the parameters in Table B.8, and equations in section 3.1.1, the response curves in Figure B.4 and B.5 have been constructed.

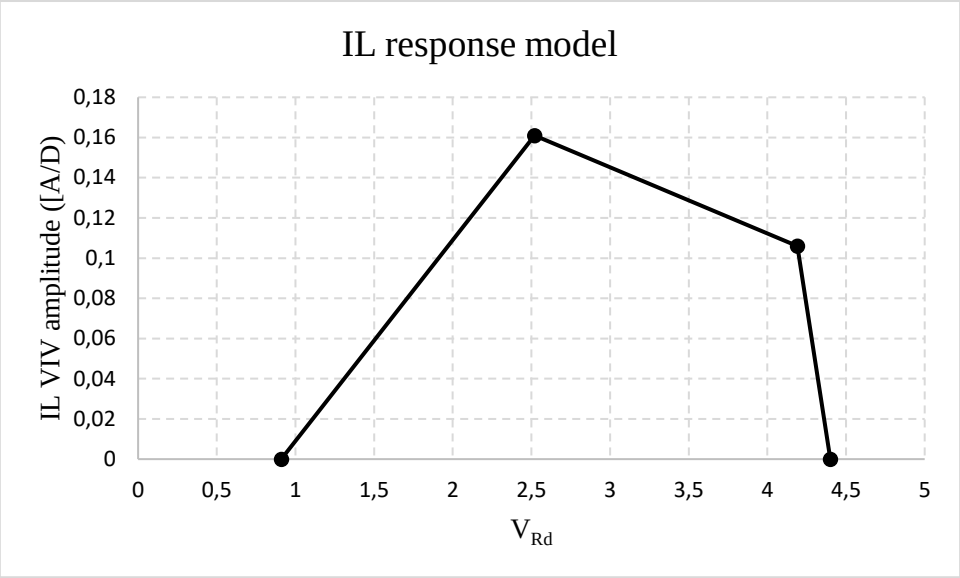

Figure B.4. IL response model for the 90° flow direction.

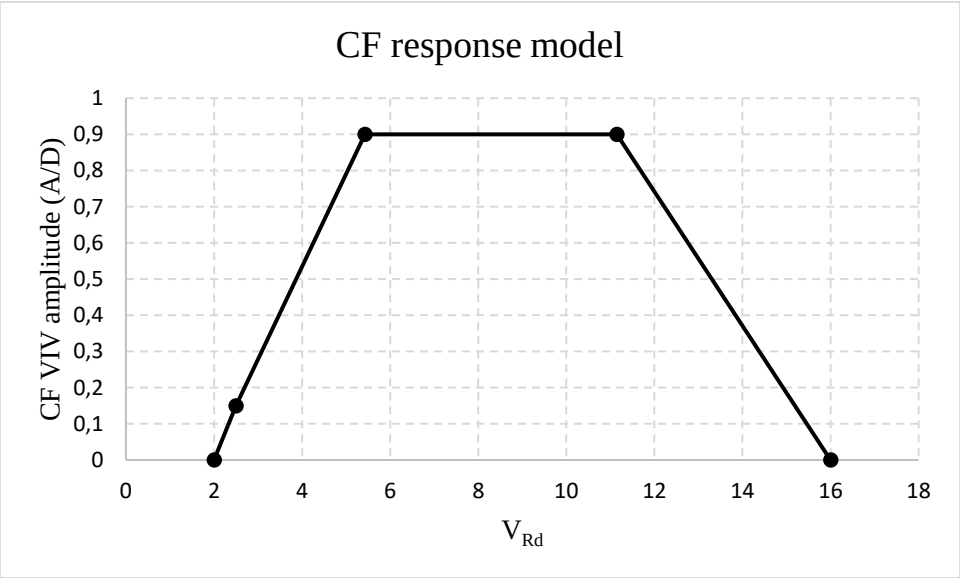

Figure B.5. CF response model for the 90° flow direction.

The reduced velocities are calculated for current velocities between 0.05-0.748m/s and the 3 first CF modes and the 4 first IL modes. This is shown in Table B.9 and B.10. Also for this current heading, the multi-mode procedure used for the 10° current heading can be used to find the dominating IL, CF, and CF induced IL modes. The dominating modes are shown in Table B.9, B.10, and B11. The maximum A/D in x, y and z-direction is given in Table B.12.

Table B.9. Dominating IL mode for the 90° flow direction.									
Velocity	IL freq.1	assosiated Vrd	IL freq.2	assosiated Vrd	IL freq. 3	assosiated Vrd	IL freq.4	assosiated Vrd	Dominating IL mode
0.05	0.8587	1.11	2.1403	0.44	3.2669	0.29	3.6218	0.26	mode 1
0.06	0.8587	1.33	2.1403	0.53	3.2669	0.35	3.6218	0.31	mode 1
0.07	0.8587	1.55	2.1403	0.62	3.2669	0.41	3.6218	0.37	mode 1
0.08	0.8587	1.77	2.1403	0.71	3.2669	0.47	3.6218	0.42	mode 1
0.09	0.8587	1.99	2.1403	0.80	3.2669	0.52	3.6218	0.47	mode 1
0.1	0.8587	2.21	2.1403	0.89	3.2669	0.58	3.6218	0.52	mode 1
0.125	0.8587	2.77	2.1403	1.11	3.2669	0.73	3.6218	0.66	mode 2
0.15	0.8587	3.32	2.1403	1.33	3.2669	0.87	3.6218	0.79	mode 2
0.175	0.8587	3.87	2.1403	1.55	3.2669	1.02	3.6218	0.92	mode 5
0.2	0.8587	4.43	2.1403	1.78	3.2669	1.16	3.6218	1.05	mode 7
0.225	0.8587	4.98	2.1403	2.00	3.2669	1.31	3.6218	1.18	mode 7
0.25	0.8587	5.53	2.1403	2.22	3.2669	1.45	3.6218	1.31	mode 7
0.275	0.8587	6.09	2.1403	2.44	3.2669	1.60	3.6218	1.44	mode 7
0.3	0.8587	6.64	2.1403	2.66	3.2669	1.75	3.6218	1.57	mode 7
0.325	0.8587	7.19	2.1403	2.89	3.2669	1.89	3.6218	1.71	mode 7
0.35	0.8587	7.75	2.1403	3.11	3.2669	2.04	3.6218	1.84	mode 7
0.375	0.8587	8.30	2.1403	3.33	3.2669	2.18	3.6218	1.97	mode 7
0.4	0.8587	8.85	2.1403	3.55	3.2669	2.33	3.6218	2.10	mode 7
0.425	0.8587	9.41	2.1403	3.77	3.2669	2.47	3.6218	2.23	mode 7
0.45	0.8587	9.96	2.1403	4.00	3.2669	2.62	3.6218	2.36	mode 7
0.475	0.8587	10.51	2.1403	4.22	3.2669	2.76	3.6218	2.49	mode 7
0.5	0.8587	11.07	2.1403	4.44	3.2669	2.91	3.6218	2.62	mode 7
0.525	0.8587	11.62	2.1403	4.66	3.2669	3.05	3.6218	2.76	mode 7
0.55	0.8587	12.17	2.1403	4.88	3.2669	3.20	3.6218	2.89	mode 7
0.575	0.8587	12.73	2.1403	5.11	3.2669	3.35	3.6218	3.02	mode 7
0.6	0.8587	13.28	2.1403	5.33	3.2669	3.49	3.6218	3.15	mode 7
0.625	0.8587	13.84	2.1403	5.55	3.2669	3.64	3.6218	3.28	mode 7
0.65	0.8587	14.39	2.1403	5.77	3.2669	3.78	3.6218	3.41	mode 7
0.675	0.8587	14.94	2.1403	5.99	3.2669	3.93	3.6218	3.54	mode 7
0.7	0.8587	15.50	2.1403	6.22	3.2669	4.07	3.6218	3.67	mode 7
0.725	0.8587	16.05	2.1403	6.44	3.2669	4.22	3.6218	3.81	mode 7
0.748	0.8587	16.56	2.1403	6.64	3.2669	4.35	3.6218	3.93	mode 7

Table B.10. Dominating CF mode for the 90° flow direction.							
Velocity	CF freq. 1	assosiated Vrd	CF freq. 2	assosiated Vrd	CF freq. 3	assosiated Vrd	Dominating CF mode
0.05	2.1741	0.44	2.5457	0.37	3.56	0.27	-
0.06	2.1741	0.52	2.5457	0.45	3.56	0.32	-
0.07	2.1741	0.61	2.5457	0.52	3.56	0.37	-
0.08	2.1741	0.70	2.5457	0.60	3.56	0.43	-
0.09	2.1741	0.79	2.5457	0.67	3.56	0.48	-
0.1	2.1741	0.87	2.5457	0.75	3.56	0.53	-
0.125	2.1741	1.09	2.5457	0.93	3.56	0.67	-
0.15	2.1741	1.31	2.5457	1.12	3.56	0.80	-
0.175	2.1741	1.53	2.5457	1.31	3.56	0.93	-
0.2	2.1741	1.75	2.5457	1.49	3.56	1.07	-
0.225	2.1741	1.97	2.5457	1.68	3.56	1.20	-
0.25	2.1741	2.19	2.5457	1.87	3.56	1.33	-
0.275	2.1741	2.40	2.5457	2.05	3.56	1.47	-
0.3	2.1741	2.62	2.5457	2.24	3.56	1.60	mode 3
0.325	2.1741	2.84	2.5457	2.43	3.56	1.74	mode 3
0.35	2.1741	3.06	2.5457	2.61	3.56	1.87	mode 3
0.375	2.1741	3.28	2.5457	2.80	3.56	2.00	mode 3
0.4	2.1741	3.50	2.5457	2.99	3.56	2.14	mode 3
0.425	2.1741	3.72	2.5457	3.17	3.56	2.27	mode 3
0.45	2.1741	3.93	2.5457	3.36	3.56	2.40	mode 3
0.475	2.1741	4.15	2.5457	3.55	3.56	2.54	mode 3
0.5	2.1741	4.37	2.5457	3.73	3.56	2.67	mode 3
0.525	2.1741	4.59	2.5457	3.92	3.56	2.80	mode 3
0.55	2.1741	4.81	2.5457	4.11	3.56	2.94	mode 3
0.575	2.1741	5.03	2.5457	4.29	3.56	3.07	mode 3
0.6	2.1741	5.25	2.5457	4.48	3.56	3.20	mode 3
0.625	2.1741	5.46	2.5457	4.67	3.56	3.34	mode 3
0.65	2.1741	5.68	2.5457	4.85	3.56	3.47	mode 3
0.675	2.1741	5.90	2.5457	5.04	3.56	3.60	mode 3
0.7	2.1741	6.12	2.5457	5.23	3.56	3.74	mode 3
0.725	2.1741	6.34	2.5457	5.41	3.56	3.87	mode 3
0.748	2.1741	6.54	2.5457	5.59	3.56	3.99	mode 3

Table B.11. Dominating CF induced IL mode for the 90° flow direction.						
Velocity	fn	Vr	Ca,CF-RES	fn,CF-RES	2*fn,CF-RES	IL mode closest to 2*fn,CF-RES
0.05						
0.06						
0.07						
0.08						
0.09						
0.1						
0.125						
0.15						
0.175						
0.2						
0.225						
0.25						
0.275						
0.3	2.1741	2.28	3.52	1.6403	3.2806	mode 5
0.325	2.1741	2.47	5.23	1.4429	2.8858	mode 5
0.35	2.1741	2.66	5.34	1.4325	2.8651	mode 5
0.375	2.1741	2.85	5.15	1.4506	2.9012	mode 5
0.4	2.1741	3.04	4.96	1.4694	2.9388	mode 5
0.425	2.1741	3.23	4.77	1.4889	2.9778	mode 5
0.45	2.1741	3.42	4.58	1.5093	3.0185	mode 5
0.475	2.1741	3.61	4.39	1.5304	3.0609	mode 5
0.5	2.1741	3.80	4.2	1.5525	3.1051	mode 5
0.525	2.1741	3.99	4.01	1.5756	3.1513	mode 5
0.55	2.1741	4.18	3.82	1.5998	3.1996	mode 5
0.575	2.1741	4.37	3.63	1.6251	3.2502	mode 5
0.6	2.1741	4.56	3.44	1.6516	3.3033	mode 5
0.625	2.1741	4.75	3.25	1.6795	3.3590	mode 5
0.65	2.1741	4.94	3.06	1.7089	3.4177	mode 5
0.675	2.1741	5.13	2.87	1.7398	3.4796	mode 7
0.7	2.1741	5.32	2.68	1.7725	3.5450	mode 7
0.725	2.1741	5.51	2.49	1.8071	3.6142	mode 7
0.748	2.1741	5.69	2.31	1.8418	3.6836	mode 7

Table B.12. Maximum A/D for the 90° flow direction.			
Velocity[m/s]	Max. A/D in x-direction	Max. A/D in y-direction	Max. A/D in z-direction
0.05		0.02	
0.06		0.04	
0.07		0.06	
0.08		0.09	
0.09		0.11	
0.1		0.13	
0.125		0.15	
0.15		0.13	
0.175		0.12	
0.2		0.09	
0.225		0.11	
0.25		0.13	
0.275		0.15	
0.3	0.2	0.065	0.0234
0.325	0.2	0.07	0.0312
0.35	0.3	0.075	0.0377
0.375	0.4	0.11	0.0455
0.4	0.4	0.11	0.0533
0.425	0.5	0.13	0.0598
0.45	0.5	0.15	0.0676
0.475	0.6	0.16	0.0741
0.5	0.6	0.16	0.0819
0.525	0.7	0.15	0.0884
0.55	0.7	0.15	0.0962
0.575	0.8	0.14	0.104
0.6	0.9	0.14	0.1105
0.625	0.9	0.14	0.117
0.65	0.9	0.38	0.117
0.675	0.9	0.42	0.117
0.7	0.9	0.45	0.117
0.725	0.9	0.49	0.117
0.748	0.9	0.52	0.117

Appendix C: Stress Assessment

C.1 Flexural and Torsional Stresses Calculated Using the VIV Response Predicted by the Response Model Approach.

C.1.1. 10° flow direction

As mentioned in section 5.3.1, for the 10° flow direction there are only torsional stresses associated with the CF modes. The flexural stresses, torsional stresses and associated torsional ratios for the different CF modes at the two locations considered for this flow direction are found in Table C1.

Table C.1. CF modal stresses at location A and B.

	Location A (approx. middle of the jumper)			Location B (right end of the jumper)		
Mode	Flexural stress[MPa]	Torsional stress[MPa]	Torsion ratio	Flexural stress[MPa]	Torsional stress[MPa]	Torsion ratio
1	7.3	0.004	0.0005479	5.6	3.23	0.577
2	0.826	7.86	9.516	12.99	4.2	0.323
5	6.5	0.0206	0.00317	93.72	15.56	0.166

Figure 5.10 shows that at location A (approximately at the middle of the jumper length) only mode 4 and 9 will give significant unit stress (stress >10% maximum stress at this location). Thus, only mode 4 and 9 are active IL modes. The two modes are not competing, hence there will be no stress reduction ($\alpha_j = 1.0$) and both modes will obtain full response. Moreover, Figure 5.10 shows that at location B (at right end of the jumper) all the IL modes are active. All the adjacent mode combinations at this location are competing so there will be a stress reduction. The stress reduction factors for the different modes at the different locations are shown in Table C.2.

Table C.2. IL modal stresses and corresponding stress reduction factors.				
	Location A (approx. middle of the jumper)		Location B (right end of the jumper)	
Mode	Flexural stress[MPa]	Reduction factor	Flexural stress[MPa]	Reduction factor
3	1.11	Not an active IL mode	41.1	0.5
4	30.75	1	93.3	0.5
6	2.29	Not an active IL mode	138.7	1
9	140.7	1	47.12	0.5

As mentioned previously, the IL modes (mode 3, 4, 6 and 9) are not associated with any torsional stresses. Thus, only the flexural stress ranges due to IL loading needs to be calculated for this current direction.

Since CF VIV is predicted to start at the same time as IL VIV for this current direction (see chapter 4), the IL stresses will only be due to CF induced IL motion. Furthermore, the DNV-RP-F105 (p.41) assumes that only the dominant CF mode potentially can contribute to CF induced IL motion. Hence, no mode reduction is necessary as single mode response is assumed.

Figure C.1 and C.2 show the flexural and torsional stresses for the different current velocities for location A and B, respectively.

Figure C.1 and C.2 show that the maximum stress at location B is due to IL VIV and the maximum stress at location A is due to CF VIV. Which coincides with the fact that the peak CF stress is found at location A and peak IL stress at location B. Figure C.1 show that at location A, for velocities larger than 0.257m/s, the torsional stresses are larger than the flexural stresses. This shows why the torsional stresses should not be neglected for rigid jumpers and spools.

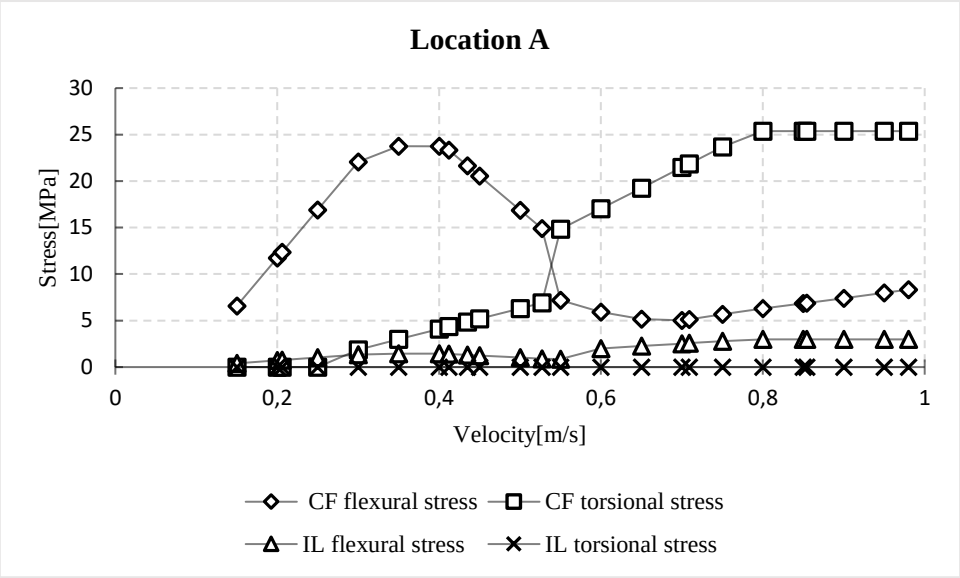

Figure C.1. Flexural and torsional stresses at location A (approximately at the middle of the jumper length).

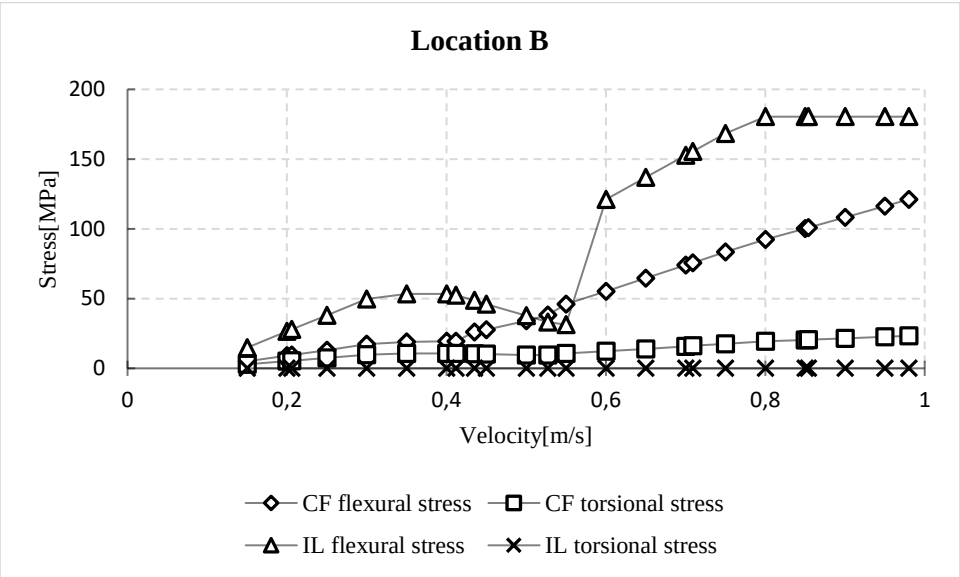

Figure C.2. Flexural and torsional stresses at location B (at the right end of the jumper).

C.1.2. 90° flow direction

As mentioned in section 5.3.1, for the 90° flow direction there are only torsional stresses associated with the IL modes. The flexural stresses, torsional stresses and associated torsional ratios for the different IL modes at the two locations considered for this flow direction are found in Table C.3.

Table C.3. IL modal stresses at location B and C.

	Location C (left end of the jumper)			Location B (right end of the jumper)		
Mode	Flexural stress[MPa]	Torsional stress[MPa]	Torsion ratio	Flexural stress[MPa]	Torsional stress[MPa]	Torsion ratio
1	5.6	3.23	0.577	5.61	3.23	0.576
2	13.02	4.2	0.323	12.99	4.19	0.323
5	93.35	15.49	0.166	93.72	15.56	0.166
7	99.18	14.2	0.143	98.7	14.14	0.143

If the torsional stresses at a location is larger than 10% of the maximum stress(flexural), the mode associated with this large torsional stress should be an active IL mode even if the flexural stresses are negligible. Furthermore, this large torsional stress should be used when determining which of two competing modes that are dominating. For the two locations considered here, the flexural stresses for all modes are larger than the torsional stresses and hence only the flexural stresses determine the active IL modes. Table C.3 show that at velocities where all modes are active, mode 1 is not an active mode as the stresses associated with this mode at the two locations considered are smaller than 10% of the maximum stresses at these locations. However, for velocities smaller than 0.125 m/s, mode 1 is the dominating mode as there is only a single-mode response for these currents. Table C.4 shows the IL modal flexural stresses and the corresponding reduction factors.

Table C.4. IL modal stresses and corresponding stress reduction factors.				
	Location C (left end of the jumper)		Location B(right end of the jumper)	
Mode	Flexural stress[MPa]	Reduction factor	Flexural stress[MPa]	Reduction factor
2	13.02	0.5	12.99	0.5
5	93.35	0.5	93.72	0.5
7	99.18	1	98.7	1

For this current direction, there are IL stresses due to IL loading until CF VIV starts (for this case CF VIV starts at 0.3 m/s). After this velocity, the IL stresses are due to CF induced IL motion. To find the torsional stress ranges, the calculated flexural stress ranges for each mode are multiplied with its associated torsion ratio.

Table C.5 show the CF modal stresses at location B and C.

Table C.5. CF modal stresses at location B and C.		
Mode	Flexural stress[MPa] at location C (left end of the jumper)	Flexural stress[MPa] at location B (right end of the jumper)
3	41.09	41.09
4	93.35	93.31
6	138.67	138.67

Figure C.3 and C.4 show the flexural and torsional stresses for the different current velocities for location C and B, respectively.

Figure C.3 and C.4 show that the stresses at the two locations considered are basically the same. This is due to the symmetry of the jumper model. For this current direction, the stresses due to torsion are small compared to the flexural stresses.

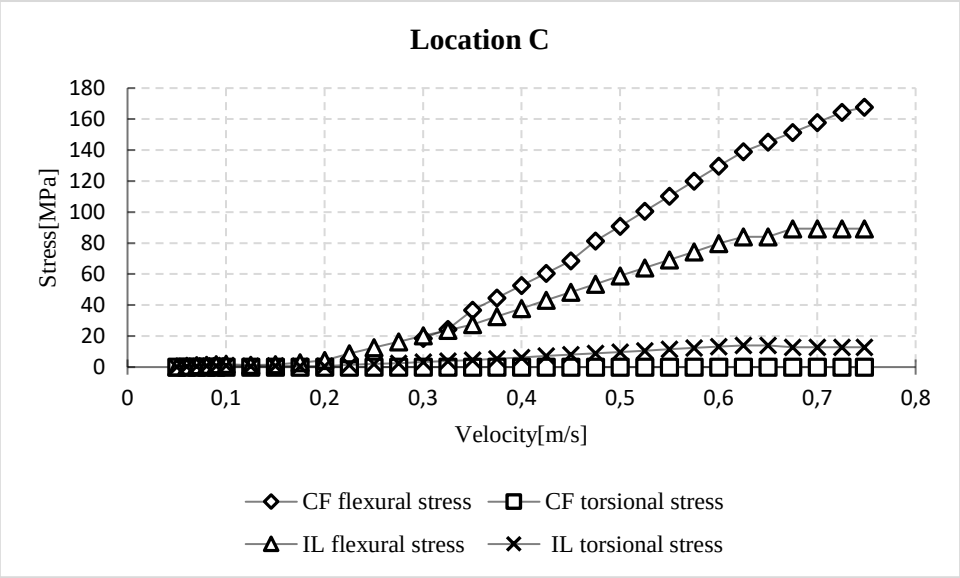

Figure C.3. Flexural and torsional stresses at location C (at the left end of the jumper).

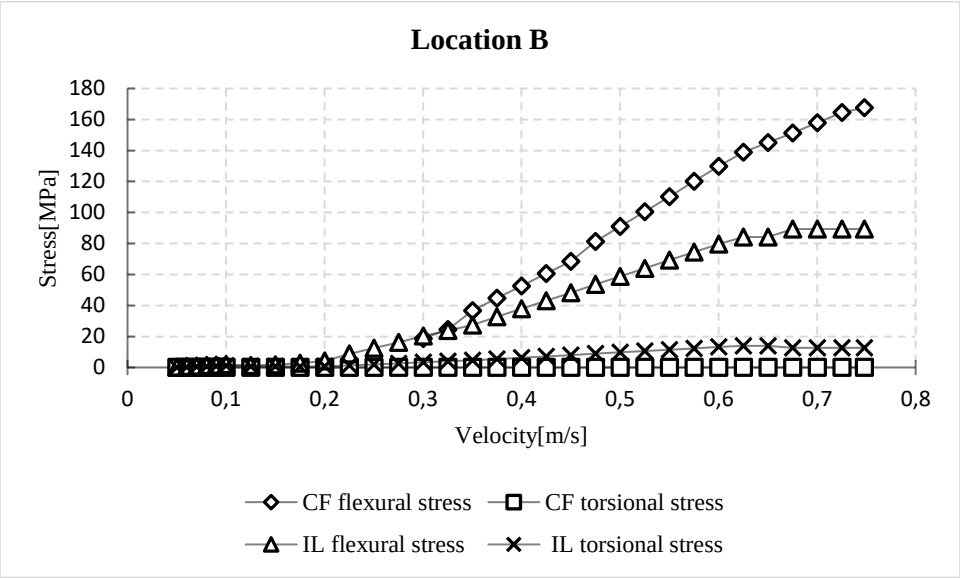

Figure C.4. Combined flexural and torsional stresses at location B (at the right end of the jumper).

C.2. Flexural and Torsional Stresses Calculated Using the VIV Response Predicted by VIVANA

Since the DNV-RP-F105(2006) uses the maximum response amplitude (found from the response models) to calculated the stress ranges, and the maximum response amplitude over the jumper model predicted by VIVANA is known from chapter 4. Thus, the maximum response amplitude over the jumper model predicted by VIVANA will be used to calculate the stress ranges. (This makes this method more conservative because the higher response amplitude, the lower reduction of the modal stresses)

Table C.6 and C.8 show the response modes and the maximum response amplitude (normalized with D) for the different current velocities predicted by VIVANA for the two different flow directions. As the dominating mode and the associated maximum response amplitude is known, the flexural stresses can be found using the equations in section 3.1.1. The torsional stresses are found by multiplying the flexural stresses with a torsion ratio also in this section.

C.2.1. 10° flow direction

Table C.6. Response mode and associated maximum A/D for the 10° flow direction.

Velocity	pure IL	IL response mode	CF	CF response mode	IL with CF	IL due to CF response mode
0.05		no mode is excited		no mode is excited		no mode is excited
0.06		no mode is excited		no mode is excited		no mode is excited
0.07	0.00	1		no mode is excited		no mode is excited
0.08	0.00	1		no mode is excited		no mode is excited
0.09	0.00	1		no mode is excited		no mode is excited
0.1	0.00	1		no mode is excited		no mode is excited
0.15	0.00	1		no mode is excited		no mode is excited
0.2	0.00	3		no mode is excited		no mode is excited
0.206	0.00	3		no mode is excited		no mode is excited
0.25	0.05	3		no mode is excited		no mode is excited
0.3	0.08	3		no mode is excited		no mode is excited
0.35	0.07	3		no mode is excited		no mode is excited
0.4	0.07	3		no mode is excited		no mode is excited
0.412	0.08	3		no mode is excited		no mode is excited
0.435	0.10	3	0.24	2	0.00	7
0.45	0.09	3	0.28	2	0.00	7
0.5	0.00	7	0.41	2	0.00	7
0.527	0.00	7	0.49	2	0.00	7
0.55	0.00	7	0.55	2	0.00	7
0.6	0.00	7	0.65	2	0.00	7
0.65	0.00	7	0.74	2	0.00	7
0.7	0.00	7	0.86	2	0.00	7
0.709	0.00	8	0.89	2	0.00	8
0.75	0.00	8	0.90	2	0.00	8
0.8	0.00	8	0.82	2	0.00	8
0.85	0.00	8	0.03	4	0.00	8
0.854	0.00	8	0.03	4	0.00	8
0.9	0.00	8	0.11	4	0.00	8
0.95	0.00	8	0.47	4	0.00	8
0.98	0.00	8	0.80	5	0.00	8

Table C.7. Modal stresses at location A and B.						
	Location A (approx. middle of the jumper)			Location B (right end of the jumper)		
Mode	Flexural stress[MPa]	Torsional stress[MPa]	Torsion ratio	Flexural stress[MPa]	Torsional stress[MPa]	Torsion ratio
1	7.3	0.004	0.00055	5.61	3.23	0.576
2	0.756	7.86	10.4	12.997	4.19	0.322
3	1.11	0	0	41.09	0	0
4	30.76	0	0	93.31	0	0
5	6.47	0.0206	0.0032	93.72	15.557	0.166
7	0.057	12.1	212.3	98.7	14.144	0.143
8	150.98	0.0193	0.00013	3.375	3.016	0.894

Figure C.5 and C.6 show the flexural and torsional stresses for location A and B, respectively.

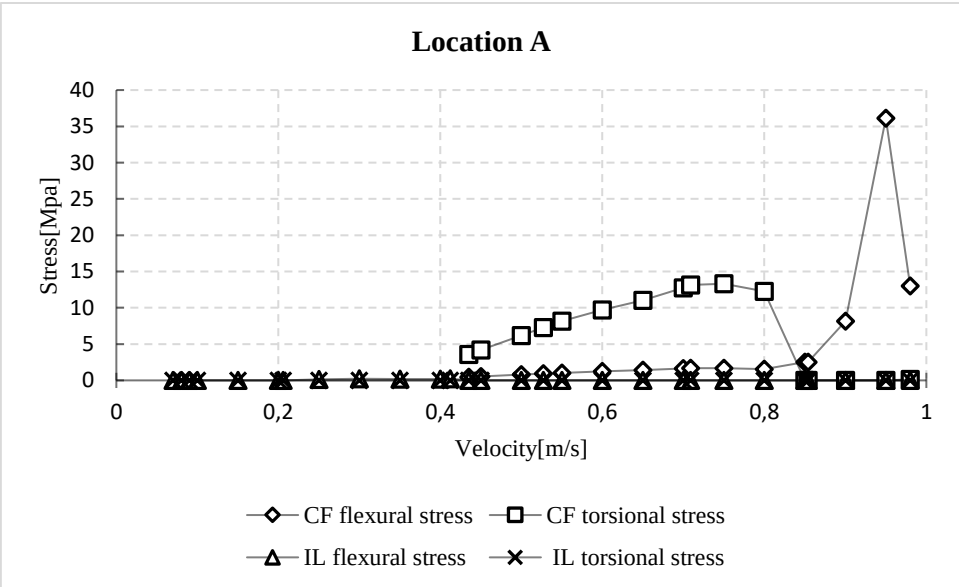

Figure C.5. Flexural and torsional stresses at location A using response amplitudes predicted by VIVANA.

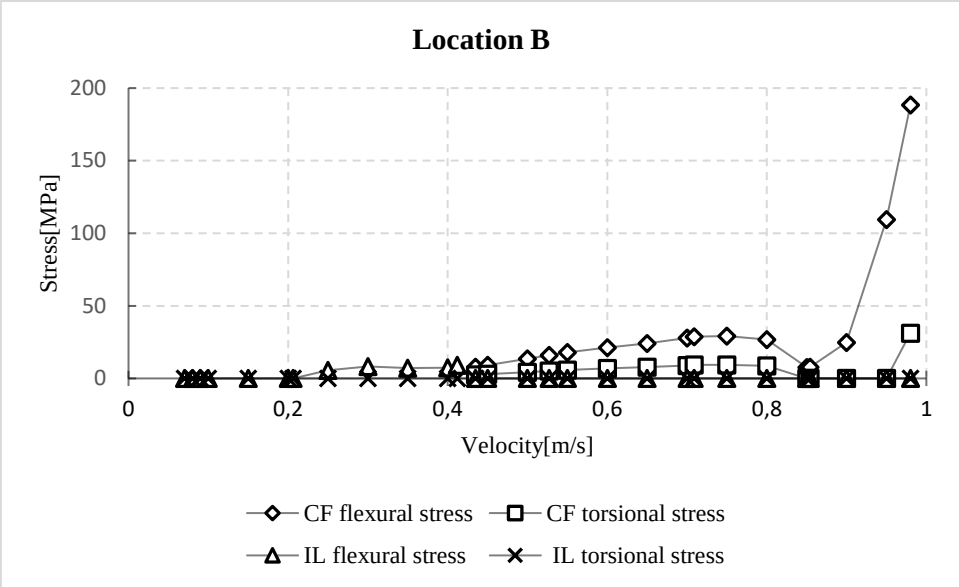

Figure C.6. Flexural and torsional stresses at location B using response amplitudes predicted by VIVANA.

Figure C.5 show that for velocities 0.425m/s to 0.8m/s the torsional stresses are larger than the flexural stresses at location A. Figure C.6 show that for velocities < 0.4m/s the maximum stress is flexural stress due to IL loading. For velocities > 0.4m/s the maximum stress is flexural stress due to CF loading.

C.2.2. 90° flow direction

Table C.8. Response mode and associated maximum A/D for the 90° flow direction.

Velocity	pure IL	response mode IL	CF	response mode CF	IL with CF	response mode IL due to CF loading
0.05		no mode is excited		no mode is excited		no mode is excited
0.06		no mode is excited		no mode is excited		no mode is excited
0.07	0.01	1		no mode is excited		no mode is excited
0.08	0.04	1		no mode is excited		no mode is excited
0.09	0.06	1		no mode is excited		no mode is excited
0.1	0.07	1		no mode is excited		no mode is excited
0.125	0.11	1		no mode is excited		no mode is excited
0.15	0.12	1		no mode is excited		no mode is excited
0.175	0.10	1		no mode is excited		no mode is excited
0.2	0.11	1		no mode is excited		no mode is excited
0.225	0.06	1		no mode is excited		no mode is excited
0.25	0.09	2		no mode is excited		no mode is excited
0.275	0.10	2		no mode is excited		no mode is excited
0.3	0.12	2		no mode is excited		no mode is excited
0.325	0.13	2		no mode is excited		no mode is excited
0.35	0.12	2		no mode is excited		no mode is excited
0.375	0.14	2		no mode is excited		no mode is excited
0.4	0.10	2		no mode is excited		no mode is excited
0.425	0.11	5		no mode is excited		no mode is excited
0.45	0.12	5	0.27	3	0.09	7
0.475	0.13	5	0.35	3	0.09	7
0.5	0.14	5	0.42	3	0.09	7
0.525	0.13	5	0.49	3	0.10	7
0.55	0.13	5	0.55	3	0.11	7
0.575	0.15	5	0.61	3	0.12	7
0.6	0.13	5	0.66	3	0.13	7
0.625	0.15	5	0.71	3	0.14	7
0.65	0.14	5	0.76	3	0.15	7
0.675	0.12	5	0.87	3	0.16	7
0.7	0.13	5	0.93	3	0.24	7
0.725	0.13	5	1.03	3	0.32	7
0.748	0.13	5	1.10	3	0.28	8

Table C.9. Modal stresses at location B and C.						
	Location C (left end of the jumper)			Location B (right end of the jumper)		
Mode	Flexural stress[MPa]	Torsional stress[MPa]	Torsion ratio	Flexural stress[MPa]	Torsional stress[MPa]	Torsion ratio
1	5.6	3.24	0.578	5.61	3.23	0.576
2	13.02	4.20	0.323	12.997	4.19	0.322
3	41.09	0	0	41.09	0	0
4	93.354	0	0	93.31	0	0
5	93.351	15.49	0.166	93.72	15.557	0.166
7	99.19	14.20	0.143	98.7	14.144	0.143
8	3.35	3.014	0.9	3.375	3.016	0.894

Figure C.7 and C.8 show the flexural and torsional stresses for location C and B, respectively.

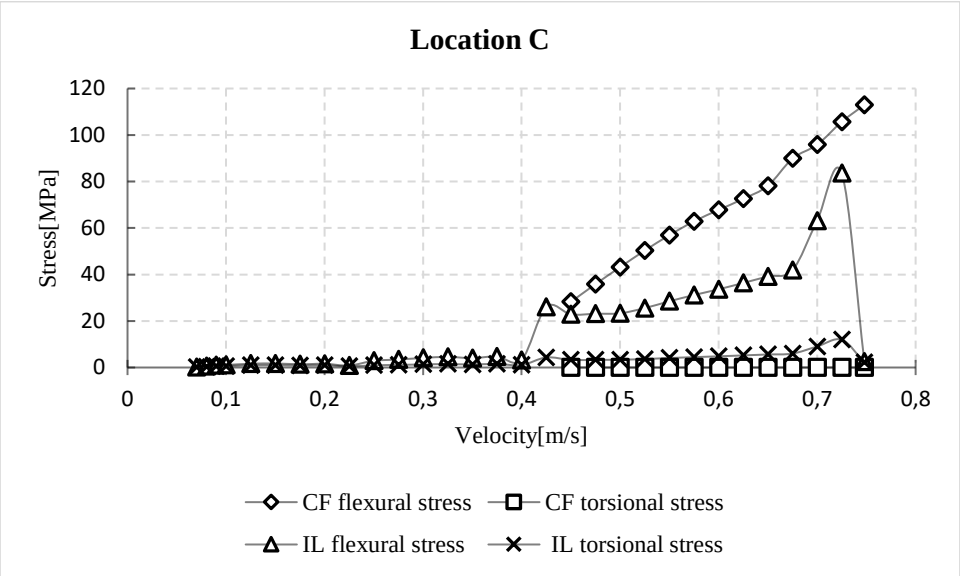

Figure C.7. Flexural and torsional stresses at location C using response amplitudes predicted by VIVANA.

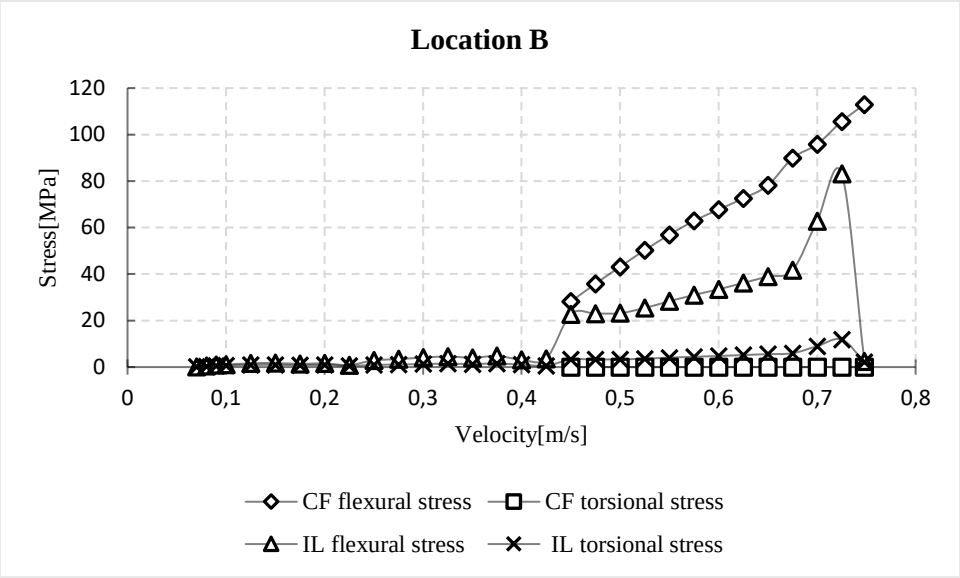

Figure C.8. Flexural and torsional stresses at location B using response amplitudes predicted by VIVANA.

Figure C.7 and C.8 show that the stresses are basically the same at these two locations. This is due to the symmetry of the jumper model. Moreover, they show that there are very small stresses for velocities ≤ 0.425m/s. For velocities > 0.425m/s the maximum stress is flexural stress due to CF loading.